

The Pennsylvania State University
The Graduate School
College of Earth and Mineral Sciences

**CHARACTERIZATION AND MODELING OF ATMOSPHERIC
FLOW WITHIN AND ABOVE PLANT CANOPIES**

A Dissertation in
Meteorology and Atmospheric Science
by
Livia Souza Freire Grion

© 2017 Livia Souza Freire Grion

Submitted in Partial Fulfillment
of the Requirements
for the Degree of

Doctor of Philosophy

May 2017

The dissertation of Livia Souza Freire Grion was reviewed and approved* by the following:

Marcelo Chamecki
Professor of Meteorology
Dissertation Advisor
Committee Co-Chair

Chris E. Forest
Professor of Climate Dynamics
Committee Co-Chair

Jose D. Fuentes
Professor of Meteorology

Xiaofeng Liu
Professor of Civil and Environmental Engineering

Johannes Verlinde
Professor of Meteorology
Associate Head, Graduate Program in Meteorology

*Signatures are on file in the Graduate School.

Abstract

The turbulent flow within and above plant canopies is responsible for the exchange of momentum, heat, gases and particles between vegetation and the atmosphere. Turbulence is also responsible for the mixing of air inside the canopy, playing an important role in chemical and biophysical processes occurring in the plants' environment. In the last fifty years, research has significantly advanced the understanding of and ability to model the flow field within and above the canopy, but important issues remain unsolved. In this work, we focus on (i) the estimation of turbulent mixing timescales within the canopy from field data; and (ii) the development of new computationally efficient modeling approaches for the coupled canopy-atmosphere flow field.

The turbulent mixing timescale represents how quickly turbulence creates a well-mixed environment within the canopy. When the mixing timescale is much smaller than the timescale of other relevant processes (e.g. chemical reactions, deposition), the system can be assumed to be well-mixed and detailed modeling of turbulence is not critical to predict the system evolution. Conversely, if the mixing timescale is comparable or larger than the other timescales, turbulence becomes a controlling factor for the concentration of the variables involved; hence, turbulence needs to be taken into account when studying and modeling such processes. In this work, we used a combination of ozone concentration and high-frequency velocity data measured within and above the canopy in the Amazon rainforest to characterize turbulent mixing. The eddy diffusivity parameter (used as a proxy for mixing efficiency) was applied in a simple theoretical model of one-dimensional diffusion, providing an estimate of turbulent mixing timescales as a function of height within the canopy and time-of-day. Results showed that, during the day, the Amazon rainforest is characterized by well-mixed conditions with mixing timescales smaller than thirty minutes in the upper-half of the canopy, and partially mixed conditions in the lower half of the canopy. During the night, most of the canopy (except for the upper 20%) is either partially or poorly mixed, resulting in mixing timescales of up to several hours. For the specific case of ozone, the mixing timescales observed during the day are much lower than the chemical and deposition timescales, whereas chemical processes and turbulence have comparable timescales during the night. In

addition, the high day-to-day variability in mixing conditions and the fast increase in mixing during the morning transition period indicate that turbulence within the canopy needs to be properly investigated and modeled in many studies involving plant-atmosphere interactions.

Motivated by the findings described above, this work proposes and tests a new approach for modeling canopy flows. Typically, vertical profiles of flow statistics are needed to represent canopy-atmosphere exchanges in chemical and biophysical processes happening within the canopy. Current single-column models provide only steady-state (equilibrium) profiles, and rely on closure assumptions that do not represent the dominant non-local turbulent fluxes present in canopy flows. We overcome these issues by adapting the one-dimensional turbulent (ODT) model to represent atmospheric flows from the ground up to the top of the atmospheric boundary layer (ABL). The ODT model numerically resolves the one-dimensional diffusion equation along a vertical line (representing a horizontally homogeneous ABL column), and the presence of three-dimensional turbulence is added through the effect of stochastic eddies. Simulations of ABL without canopy were performed for different atmospheric stabilities and a diurnal cycle, to test the capabilities of this modeling approach in representing unsteady flows with strong non-local transport. In addition, four different types of canopies were simulated, one of them including the transport of scalar with a point source located inside the canopy. The comparison of all simulations with theory and field data provided satisfactory results. The main advantages of using ODT compared to typical 1D canopy-flow models are the ability to represent the coupled canopy-ABL flow with one single modeling approach, the presence of non-local turbulent fluxes, the ability to simulate transient conditions, the straightforward representation of multiple scalar fields, and the presence of only one adjustable parameter (as opposed to the several adjustable constants and boundary conditions needed for other modeling approaches).

The results obtained with ODT as a stand-alone model motivated its use as a surface parameterization for Large-Eddy Simulation (LES). In this two-way coupling between LES and ODT, the former is used to simulate the ABL in a case where a canopy is present but cannot be resolved by the LES (i.e., the LES first vertical grid point is above the canopy). ODT is used to represent the flow field between the ground and the first LES grid point, including the region within and just above the canopy. In this work, we tested the ODT-LES model for three different types of canopies and obtained promising results. Although more work is needed in order to improve first and second-order statistics within the canopy (i.e. in the ODT domain), the results obtained for the flow statistics in the LES domain and for the third order statistics in the ODT domain demonstrate that the ODT-LES model is capable of capturing some important features of the canopy-atmosphere interaction. This new surface superparameterization approach using ODT provides

a new alternative for simulations that require complex interactions between the flow field and near-surface processes (e.g. sand and snow drift, waves over water surfaces) and can potentially be extended to other large-scale models, such as mesoscale and global circulation models.

Table of Contents

List of Figures	ix
List of Tables	xvi
Preface	xvii
Acknowledgments	xviii
Chapter 1	
Introduction	1
Chapter 2	
Turbulent mixing and removal of ozone within an Amazon rainforest canopy	10
2.1 Introduction	10
2.2 Methods	12
2.2.1 Data set	12
2.2.2 Data analysis	16
2.2.3 Mass balance of ozone inside the canopy	19
2.2.3.1 Turbulent mixing timescale	19
2.2.3.2 Ozone chemistry timescale	21
2.2.3.3 Ozone nonchemical removal timescale	22
2.2.3.4 Applicability of the eddy diffusivity model	24
2.3 Results	24
2.3.1 Turbulent mixing of ozone into the forest	24
2.3.2 Timescales for turbulent mixing	30
2.3.3 Timescales for ozone sink within the forest	35
2.4 Conclusions	38
2.A A simplified relation between Eulerian and Lagrangian timescales .	39
2.B Equivalent eddy diffusivity	41
2.C Determination of the deposition velocity	42
2.D Criteria for validity of eddy diffusivity model	43

Chapter 3	
A one-dimensional stochastic model of turbulence within and above plant canopies	45
3.1 Introduction	45
3.2 Model description	48
3.2.1 The One-Dimensional Turbulence model	48
3.2.2 The filtered ODT model	51
3.3 Simulations setup and experimental data	54
3.3.1 Rough-wall ABL simulations	54
3.3.2 Canopy-resolving ABL simulations	55
3.4 Results and Discussion	58
3.4.1 Rough-wall neutral ABL simulations	58
3.4.2 Rough-wall stratified ABL simulations	61
3.4.3 Canopy flow, case 1: CHATS experiment	66
3.4.4 Canopy flow, case 2: Mahomet cornfield experiment	67
3.4.5 Canopy flow, case 3: Scalar transport in lab experiment	71
3.5 Conclusions	72
Chapter 4	
Plant canopy representation in Large-Eddy Simulation using a one-dimensional stochastic wall model	76
4.1 Introduction	76
4.2 Description of the ODT-LES model	79
4.2.1 Overview of the two-way coupling approach	79
4.2.2 LES model	81
4.2.3 ODT model	82
4.2.4 The average ODT velocity field	84
4.2.5 ODT-overlap region	85
4.2.6 LES bottom boundary condition	85
4.2.7 ODT Pressure correction	86
4.2.8 Final notes	86
4.3 Simulation setup	87
4.4 Results and Discussion	90
4.4.1 Smooth channel flow	90
4.4.2 Rough channel flow	93
4.4.3 Canopy flows	96
4.4.4 Computational cost	100
4.5 Conclusions	103

Chapter 5	
Conclusions	105
Appendix	
Flux-profile relationship for dust concentration in the stratified atmospheric surface layer	108
A.1 Models for the mean concentration dust profile	110
A.1.1 Existing models for mean concentration profile	110
A.1.2 A new general solution for mean concentration profile	114
A.2 Large-Eddy Simulation of dust concentration in the atmospheric boundary layer	116
A.2.1 Summary of simulations	117
A.3 Results	118
A.3.1 The applicability of the steady-state assumption	118
A.3.2 The estimation of mean vertical concentration profiles of dust	122
A.3.3 Surface flux estimations from concentration data	125
A.4 Conclusions	128
Bibliography	131

List of Figures

2.1	Profiles of [(a), (f) and (k)] standard deviation of vertical wind velocity (σ_w), [(b), (g) and (l)] Lagrangian integral timescale of the vertical velocity (T_L), [(c), (h) and (m)] eddy diffusivity (K), [(d), (i) and (n)] ozone mixing ratio ($[\overline{O_3}]$) and [(e), (j) and (o)] normalized ozone mixing ratio ($(\overline{[O_3]}/\overline{[O_3]}_h)$) for the morning transition of (a)-(e) October 30, (f)-(j) December 3, and (k)-(o) December 4, 2014.	26
2.2	Normalized ozone mixing ratio ($(\overline{[O_3]}/\overline{[O_3]}_h)$) as a function of eddy diffusivity normalized by the e-folding eddy diffusivity (K/K_e) for the morning transition of October 30, December 3, and December 4, 2014. Equation (2.17) (black line), $K = 0.5K_e$ (red line) and $K = 2K_e$ (blue line)	27
2.3	Eddy diffusivity (K) as a function of local time and height. (a) October 30, 2014, (b) December 3, 2014 and (c) December 4, 2014. Blue and red lines indicate the limits $K = 0.5K_e$ and $K = 2K_e$, respectively. The arrows at the bottom indicate the times of the profiles presented in Figure 2.1.	28
2.4	Yearly averaged eddy diffusivity ($\langle K \rangle$). Blue and red lines indicate the limits $\langle K \rangle = 0.5K_e$ and $\langle K \rangle = 2K_e$, respectively.	29
2.5	Time fraction spent in the poorly mixed (blue), partially mixed (yellow) and well-mixed (red) regimes as a function of height for (a) nighttime, (b) sunrise and sunset transitions, and (c) daytime. See text for more details.	30
2.6	Time evolution of ozone mixing ratio inside the forest for the two values of eddy diffusivity used to separate the mixing regimes. (a) $K = 0.045 \text{ m}^2 \text{s}^{-1}$ and (b) $K = 0.18 \text{ m}^2 \text{s}^{-1}$. Yellow, red, blue and black lines indicate mixing times equal to 10, 30, 60, and 120 min, respectively. The vertical dashed line represents the limit for well-mixed regime $(\overline{[O_3]}/\overline{[O_3]}_h = 0.86$	32

2.7	Turbulent mixing timescale (τ_{mix}) as a function of local time and height obtained from the yearly averaged eddy diffusivity $\langle K \rangle$ using (a) $K_{\text{eq},1}$ and (b) $K_{\text{eq},2}$, representing lower and upper bounds on the expected timescales, respectively. Yellow, red, blue and black lines indicate mixing times equal to 10, 30, 60, and 120 min, respectively.	33
2.8	Same as Figure 2.7 but for December 3 2014.	34
2.9	Average turbulent mixing timescale (τ_{mix}) as a function of height obtained from the yearly averaged eddy diffusivity $\langle K \rangle$ for nighttime (blue) and daytime (red). Periods are divided as in Figure 2.5. The bounds are estimates of timescales using $K_{\text{eq},1}$ and $K_{\text{eq},2}$, while the true timescale is expected to fall somewhere in the filled area in between.	34
2.10	(a) Deposition velocity (V_S) as a function of time. Black line corresponds to results presented by Fitzjarrald et al. (1990) and Fan et al. (1990) for a similar site in the Amazon forest, dashed lines correspond to results presented by Rummel et al. (2007) for wet (yellow) and dry (red) in the Amazon forest. (b) Values of the criteria $N_{GD} = V_S/(3u_*)$ for applicability of the eddy diffusivity model.	36
2.11	Timescales for turbulent mixing (τ_{mix}), chemical reaction with BVOCs (τ_{chem}), and nonchemical removal processes ($\tau_{\text{su,dd}}$) for (a) daytime and (b) nighttime conditions.	38
3.1	Surface layer results for neutral ABL simulations. (a) Normalized mean streamwise velocity, (b) normalized vertical gradient of streamwise velocity, (c) eddy viscosity and (d) vertical velocity standard deviation for four different resolutions ($dz = 0.5, 1, 2$ and 5 m in red, blue, black and green lines, respectively). The gray line represents the law-of-the-wall (LOTW) predictions.	60
3.2	Results for neutral ABL simulations. (a) Vertical flux of streamwise velocity caused by the stochastic eddy events (yellow), SGS model (green) and total flux (black), for $dz = 5\text{ m}$. (b) Same as (a) for surface layer and $dz = 5$ and 0.5 m (solid and dashed lines, respectively). (c) TKE shear production (positive values) and SGS dissipation rate (negative values) normalized by $u_*^3/\kappa z$	61
3.3	(a) Streamwise and (b) vertical velocity spectra for different heights (from 0.01 to $0.1 z_i$), normalized by surface-layer scales.	62

3.4	Surface layer results unstable (red) and stable ABL simulations (blue). (a) Normalized mean streamwise velocity, (b) normalized vertical gradient of streamwise velocity, (c) eddy viscosity and (d) standard deviation of vertical velocity. The thicker lines represents the MOST	63
3.5	Time evolution of (a) the kinematic heat flux (magenta) and streamwise geostrophic wind (blue) applied in the LES and in the ODT ($V_g = 0$). Comparison between LES (black, Kumar et al. (2006)) and ODT (red) results for (b) friction velocity and (c) ABL height divided by Obukhov length	65
3.6	Profiles of ABL diurnal cycle. Comparison between LES (dashed, Kumar et al. (2006)) and ODT (solid) results for (a) potential temperature profile and (b) mean streamwise wind velocity during the stable ABL period and (c) potential temperature profiles and (d) heat flux for the unstable ABL period.	66
3.7	Results for neutral surface layer with walnut orchard without leaves (in blue, $h = 10\text{ m}$, $u_h = 2.03\text{ m s}^{-1}$ and $u_* = 0.30\text{ m s}^{-1}$) and with leaves (in red, $h = 10\text{ m}$, $u_h = 1.44\text{ m s}^{-1}$ and $u_* = 0.32\text{ m s}^{-1}$). Circles correspond to experimental results, solid and dashed lines correspond to ODT results for $dz = 0.1h$ and $dz = 0.05h$ respectively. (a) Mean streamwise velocity, (b) mean vertical flux of streamwise velocity, standard deviation of (c) streamwise and (d) vertical velocity, skewness of (e) streamwise and (f) vertical velocity.	68
3.8	Results for neutral surface layer with cornfield ($h = 2\text{ m}$ and $u_* = 0.52\text{ m s}^{-1}$). Circles correspond to experimental results, red lines correspond to ODT results for $dz = 0.05h$, blue lines correspond to Second Order Closure Model (SOCM, Gleicher et al. (2014)), and black lines correspond to Large-Eddy Simulation (LES) with plant reconfiguration. (a) Mean streamwise velocity, (b) mean vertical flux of streamwise velocity, standard deviation of (c) streamwise and (d) vertical velocity, skewness of (e) streamwise and (f) vertical velocity.	69
3.9	TKE budget terms (production in blue, transport in green, SGS dissipation in red, work against drag in black) for neutral surface layer with corn field ($h = 2\text{ m}$ and $u_* = 0.52\text{ m s}^{-1}$).	71
3.10	Scalar concentration field S normalized by $s_* = (\text{eddy flux}_s/u_*)_h$ as a function of streamwise and vertical directions. Dashed horizontal line represents the source location, solid horizontal line represents the canopy height, and solid vertical line corresponds to measurement position	72

3.11 Results for canopy model in wind-tunnel ($h = 60$ mm, $u_* = 1$ m s $^{-1}$ and $s_* = 0.23$). Circles correspond to experimental results, red lines correspond to ODT-space, green lines correspond to ODT-time ($dz = 0.03 h$), and blue lines correspond to Lagrangian Stochastic (LS) model (Cassiani et al., 2007). (a) Mean streamwise velocity, (b) mean vertical flux of streamwise velocity, (c) standard deviation of vertical velocity, (d) mean scalar concentration, (e) mean vertical flux of scalar, (f) standard deviation of scalar.	73
4.1 Illustration of the ODT-LES model.	79
4.2 Illustration of the velocity and momentum flux vertical positions in the LES staggered grid.	82
4.3 Illustration of ODT velocity field top boundary condition and ODT-overlap region velocity field interpolation.	84
4.4 Illustration of the three different types of simulations performed with the ODT-LES model: (a) smooth channel, (b) rough channel, and (d) flow through plant canopy.	87
4.5 Mean streamwise velocity profile for the smooth-channel flow simulation with $Re_* = 395$, $C_\lambda = 20$ and $L_{\max} = 3.5$. ODT (solid lines) and LES (dashed lines) results are shown for $Z_\lambda = 0$ (black), 5 (red) and 20 (blue). DNS result is shown in gray.	91
4.6 Profiles of (a) total stress and (b) mean streamwise velocity for the smooth-channel flow simulation with $Re_* = 395$, $Z_\lambda = 20$ and $L_{\max} = 3.5$. ODT (solid lines) and LES (dashed lines) results are shown for $C_\lambda = 15$ (black), 20 (blue) and 40 (red). DNS results are shown in gray.	91
4.7 Profiles of (a) mean streamwise velocity and (b) streamwise velocity standard deviation for the smooth-channel flow simulation with $Re_* = 590$, $Z_\lambda = 20$ and $C_\lambda = 20$. ODT (solid lines) and LES (dashed lines) results are shown for $L_{\max} = 2.5$ (black), 3.5 (blue) and 4.5 (red). DNS results are shown in gray.	92

4.8	Statistics of the velocity field for smooth channel simulations for $Re_* = 395$ (open symbols, dashed lines) and $Re_* = 590$ (filled symbols, solid lines, vertically dislocated), corresponding to ODT (\hat{u}_i , blue) and LES (\tilde{U}_i , red). Results of (a) total shear, (b) normalized mean streamwise velocity, normalized standard deviation of (c) streamwise and (d) vertical velocity. Black lines correspond to DNS results from Moser et al. (1999). (a) corresponds to $Re_* = 590$ only and it also presents the LES resolved shear (green) and subgrid-scale + viscous shear (yellow). (d) also presents the standard deviation of \tilde{v}_3 (cyan).	94
4.9	Statistics of the velocity field from rough channel simulation, corresponding to ODT (\hat{u}_i , blue) and LES (\tilde{U}_i , red). Results of (a) normalized mean streamwise velocity, (b) total shear, normalized standard deviation of (c) streamwise and (d) vertical velocity. Black lines corresponds to LES results from Bou-Zeid et al. (2005). (b) also presents the LES resolved (green) and subgrid-scale shear (yellow).	95
4.10	Same as Figure 4.9 but for $x_3/H \leq 0.12$	96
4.11	Corn simulation: ODT (blue) and LES (red) results of (a) normalized mean streamwise velocity, standard deviation of (b) streamwise and (c) vertical velocity, skewness of (d) streamwise and (e) vertical velocity and (f) vertical flux of streamwise velocity. Black dots correspond to field data presented by Pan et al. (2014). (f) also presents the LES resolved (green) and SGS (yellow) vertical flux of streamwise velocity.	97
4.12	Same as Figure 4.11 for $0 < x_3/h < 2$. LES results obtained by Pan et al. (2014) (magenta) and ODT-alone results (yellow) are also shown	98
4.13	CHATS simulation: ODT (solid lines) and LES (squares) results of (a) normalized mean streamwise velocity, standard deviation of (b) streamwise and (c) vertical velocity, skewness of (d) streamwise and (e) vertical velocity and (f) vertical flux of streamwise velocity. Open dots correspond to field data presented by Dupont and Patton (2012) for neutral conditions. Results for no-leaves period (blue) and with-leaves period (red).	99
4.14	Same as Figure 4.13 but for $0 < x_3/h < 3$ and no-leaves case. ODT-alone results are shown in yellow.	100
4.15	Same as Figure 4.14 but for with-leaves case.	101

4.16 (a) CPU time per LES timestep as a function of number of LES grid points $N = n_x = n_y = n_z = 32, 64$ and 128 . (b) CPU time per LES timestep per processor as a function of number of processors used (4, 8 and 16), for $N = 64$. All results correspond to the rough-channel simulation using ODT-LES (blue) and LES (red).	102
A.1 Examples of profiles obtained from Equation (A.12) for particles with diameter $D_p = 10$ (solid lines) and $20 \mu\text{m}$ (dashed lines), with unstable ($L = -5 \text{ m}$, red), neutral (black) and stable ($L = 5 \text{ m}$, blue) ABLs. Arbitrary values of $u_* = 0.2 \text{ m s}^{-1}$, $\Phi/C_r = 0.05 \text{ m s}^{-1}$ (net emission) and $\Phi/C_r = -0.05 \text{ m s}^{-1}$ (net deposition) were used.	115
A.2 Snapshots of normalized particle concentration field (\bar{C}/\bar{C}_r), for $D_p = 10 \mu\text{m}$, for emission simulations in (a) neutral and (b) unstable ABL.	119
A.3 Time evolution of the ratio between the unsteady term of Equation (A.16) and the turbulent flux, at $z/z_i \sim 0.05$, for all particle sizes. (a) Emission simulations, neutral ABL (solid lines) and unstable ABL (dashed lines). (b) Deposition simulations for neutral ABL (solid lines) and unstable ABL (dashed lines). (c) Deposition simulations for stable ABL. All times are normalized by the eddy turnover time scale for the ABL T_{eddy}	120
A.4 Vertical profiles of each term of the unsteady flux equation (A.16) normalized by the absolute value of the turbulent flux at the surface ($ \bar{w}'\bar{C}'_s $), for particles with (a) $D_p = 1 \mu\text{m}$ and (b) $D_p = 30 \mu\text{m}$ for emission simulations under neutral (solid lines) and unstable (dashed lines) ABL, (c) $D_p = 10 \mu\text{m}$ for deposition simulations under neutral (solid lines), unstable (dashed lines) and stable (thin lines) ABL.	121
A.5 Normalized mean vertical concentration profiles of dust in the neutral surface layer for different particle diameters (1, 10, 20 and $30 \mu\text{m}$, as indicated in the figure).	124
A.6 Normalized mean vertical concentration profiles of dust in the unstable surface layer for different particle diameters (1, 10, 20 and $30 \mu\text{m}$, as indicated in the figure).	125
A.7 Normalized mean vertical concentration profiles of dust in the deposition case for different particle diameters (1 and $10 \mu\text{m}$) and atmospheric stability, as indicated in the figure.	126

List of Tables

2.1	Vertical location of the ten sonic anemometers and number of data blocks used in the analyses for the current study. Canopy height $h = 35$ m is used.	13
2.2	Approximate values of vertically averaged mixing ratios of isoprene, monoterpenes, and sesquiterpenes obtained from Jardine et al. (2011) and Alves et al. (2016)	15
2.3	Three mixing regimes defined for the Amazon rainforest canopy	27
2.4	Summary of occurrence of the three mixing regimes (numbers represent fraction of time in poorly mixed; partially mixed; well-mixed regimes).	31
2.5	Values of bulk sink deposition velocity V_S , chemical deposition velocity V_{chem} and nonchemical deposition velocity $V_{\text{su,dd}}$	37
3.1	Setup for ODT simulations. The canopy-resolving simulations are based on field and laboratory experiments that will be used for assessment of simulation results: ¹ orchard data from Patton et al. (2010) (the different LAI and u_* corresponds to no-leaves and with-leaves periods); ² cornfield data from Gleicher et al. (2014); ³ laboratory data from Raupach et al. (1986) and Coppin et al. (1986). ⁴ Note that the drag coefficient reported by Raupach et al. (1986) is divided by 2 here, because they use a (1/2) in the definition of the drag force.	56
4.1	Setup for ODT-LES simulations without canopy (l is the half-channel height, u_* is the friction velocity).	89
4.2	Setup for ODT-LES simulations with canopy.	89
A.1	Simulations setup: domain and grid size.	117
A.2	Simulation setup: physical parameters. $z_{i,0}$ and $z_{i,f}$ are the initial and final ABL heights respectively, (U_g, V_g) are the horizontal components of geostrophic wind, $\overline{w'\theta'}_0$ is the surface heat flux, u_* is the friction velocity and L is the Obukhov length. Emission (emi.) and deposition (dep.) cases.	118

Preface

Chapter 2 of the present dissertation is a manuscript entitled “Turbulent mixing and removal of ozone within an Amazon rainforest canopy” by Livia S. Freire, Tobias Gerken, Jesus Ruiz-Plancarte, Dandan Wei, Jose D. Fuentes, Gabriel G. Katul, Nelson L. Dias, Otávio C. Acevedo and Marcelo Chamecki, currently under review in the *Journal of Geophysical Research*. Chapter 3 is a manuscript entitled “A one-dimensional stochastic model of turbulence within and above plant canopies” by Livia S. Freire and Marcelo Chamecki, currently under review in the journal *Agricultural and Forest Meteorology*. Chapter 4 is in preparation for future publication.

The appendix of this dissertation presents a journal article entitled “Flux-Profile Relationship for Dust Concentration in the Stratified Atmospheric Surface Layer” by Livia S. Freire, Marcelo Chamecki and John A. Gillies, published in the journal *Boundary-Layer Meteorology* with Copyright 2016 by Springer (Freire et al., 2016). Although it is not related to the main topic of the dissertation, this article was developed as part of the doctorate studies and is presented for completeness.

Acknowledgments

I would like to begin expressing my gratitude to my entire family, all the Souzas, Freires and Grions, for the support and love that brought me to this moment. In particular, I am grateful to my grandparents, for being the foundation of this amazing family, and my parents, for all the incentive and investment on my education. To my husband, André, thank you for being so present even from far away, giving me the encouragement that I needed to be able to reach this point of my professional life.

I am very grateful for all the amazing friends I have, without whom it would not be possible for me to go through grad school. Alex, Alicia, Bicheng, Burkely, Dandan, Giovanni, Jesus, Liege, Paulo, Scott, Tobias, Vanessa, Ying, and many other amazing people I have had the privilege to meet along the way. Thanks go to the amazing group of people in the department, all the staff, professors and students; I truly believe I could not have chosen a better place to be. To the professors I had the privilege of taking classes from and to the members of my committee, I cannot express how lucky I feel about having this opportunity.

I would like to thank my master's advisor, Prof. Nelson Dias, for introducing me to my field of research and to Prof. Marcelo Chamecki. It has been an honor and a privilege to be part of Marcelo's group, and I'm very grateful for all the opportunities he gave me during the last four and half years, beyond even my highest expectations. Marcelo is a great advisor, professor and friend, and I'm thankful for all the support I received from him and his amazing family during my time in grad school.

Finally, I'm thankful for the financial support of the Brazilian Government (through the program *Science Without Borders*, CNPq), Prof. Marcelo Chamecki and the Department of Meteorology and Atmospheric Science of Pennsylvania State University.

Thank you.

Every step the mind takes in its progress towards Knowledge makes some discovery, which is not only new, but the best too, for the time at least.

—John Locke

Chapter 1

Introduction

The turbulence in the atmospheric boundary layer (ABL) drives the exchange of momentum, heat, gases and particles between vegetated surfaces and the overlaying atmosphere, playing a crucial role in the biogeochemical cycles of the Earth. In addition to transport, turbulence's ability to keep the environment well-mixed or create spatial variability on the scalars' concentration field is critical for the efficiency of chemical reactions and biophysical processes happening within the canopy. For example, when biogenic hydrocarbons emitted by plants experience turbulent mixing that is slow compared to oxidation rates, turbulence becomes a controlling factor on the lifetime of the chemical species involved (Bryan et al., 2012). Another example is the stomatal activity responsible for the plant's photosynthesis and transpiration, as turbulence impacts local temperature and humidity levels which are part of the stomatal aperture regulation (Jones, 1998). At larger scales, turbulence is also responsible for connecting the plant environment with the upper levels of the ABL and the free troposphere. This connection enables a different set of chemical and biophysical processes, such as large-scale transport of pollen and spores (O'Connell et al., 2007) and the deposition of long-range transported nutrients (Swap et al., 1992). Hence, the understanding of the turbulent flow field within the canopy and its connection to large-scale atmospheric motion is relevant to ecology, air quality, climate and many other geoscience fields.

In an attempt to improve the current understanding of canopy-atmosphere interaction, this study focuses on the characterization and modeling of the flow field within and above plant canopies. In cases of extensive forests and crops, vertical variations are usually more pronounced than horizontal ones, and the horizontal variability can be neglected to a first-order approximation. Hence, in this study we focus on the description of vertical profiles (hereafter referred to

as “profiles”) of turbulence and scalar mixing within horizontally homogeneous canopies. As described in the review by Finnigan (2000), the presence of canopies create a unique type of turbulent flow with characteristics that are extremely relevant for atmospheric processes. First, the intensity of the streamwise velocity is significantly reduced inside the canopy due to the blocking of the flow by the plants, resulting in a high-shear region at canopy top. This scenario resembles the classical mixing-layer flow from theoretical fluid mechanics, in which two streams with different velocities run in parallel, developing a shear instability at the interface between them that leads to the formation of coherent vortices. Similarly, the shear instability at canopy top is responsible for the development of coherent structures, creating a succession of downward and upward coherent fluid motions (known as *sweeps* and *ejections*, respectively) that produce non-local fluxes and non-Gaussian statistics. All these characteristics differ significantly from the classical surface-layer turbulence, motivating the development of specific theories and models for canopy flows.

In the region corresponding to the lowest $\sim 10\%$ of the ABL, known as the atmospheric surface layer, the mean profile and turbulent transport of momentum and scalars are usually described by the Monin-Obukhov Similarity Theory (MOST). MOST is a set of flux-profile relationships that depend on the atmospheric thermal stability, obtained from dimensional analysis for the flow field over an infinite, rough, horizontally homogeneous, flat surface (Kaimal and Finnigan, 1994). Under these conditions, the mean flow can be separated into a *roughness sublayer* (within and immediately above the roughness elements) and an *outer sublayer* (the region above the roughness sublayer). MOST is valid in the outer sublayer, a region where the different types of roughness cause a shift in the mean profiles without affecting their shape (Flack et al., 2007). For that reason, any surface type can be represented by a single length scale z_0 known as roughness height, which determines the height at which the mean wind profile goes to zero. In the roughness sublayer, on the other hand, the flow statistics are dominated by turbulent structures related to specific features of the roughness elements (Florens et al., 2013), as is the case with the coherent structures present at canopy top. Typically, the roughness sublayer extends up to two to five times the roughness height (Flack et al., 2007), which in the case of grass and low vegetation corresponds to a small portion of the atmospheric surface layer. Conversely, the roughness sublayer created by tall crops

and forests can extend tens of meters in height, significantly reducing the size of the atmospheric surface layer. This fact needs to be taken into account, for example, when performing mesoscale and global circulation modeling, as they use MOST as surface parameterization for fluxes of momentum and scalars (e.g. Jiménez et al., 2012; Lindvall et al., 2013; Molod et al., 2015; Xu et al., 2015). When the first vertical grid of the model is above the roughness sublayer (and within the surface layer), MOST is adequate given that the roughness height parameter is specified for each type of surface present in the model. For tall canopies, a second parameter representing the displacement height of the MOST profile is also needed. Raupach (1994) proposed simplified expressions that relate both parameters with canopy height and leaf area index, quantities typically measured in the characterization of crops and forests. For cases where the lowest level of the large-scale model is located within the roughness sublayer, specific corrections to MOST have to be applied (De Ridder, 2010; Wouters et al., 2012). When detailed information about the flow field within the canopy or in the roughness sublayer is required, other models that provide profiles of mean wind or other flow statistics need to be used. These models can go from simple empirical equations for the mean wind profile (Yamazaki et al., 1992) to numerical solutions of the simplified Reynolds Averaged Navier-Stokes (RANS) equation (Wilson and Shaw, 1977), a choice that depends on the specific application and the computational resources available.

A wide range of models have been proposed to represent the flow field within the canopy and in the roughness sublayer. The simplest ones correspond to empirical one-dimensional equations used to represent profiles of mean wind under equilibrium (steady-state) conditions. Within the canopy, the most widely used equation for mean wind is an exponential function of three canopy parameters: canopy height, mean velocity at canopy top and a canopy flow index (which is empirically determined for each type of plant) (Cionco, 1978). A model that shifts from the exponential inside the canopy to the MOST above has been used to represent the mean streamwise velocity from the canopy bottom up to the top of the surface layer under neutral conditions (Yamazaki et al., 1992). Harman and Finnigan (2007) improved this model to include the effect of atmospheric stability. This simple approach is commonly used within empirical models focused on representing the bulk effect of canopy on heat, moisture and carbon budgets. These so-called “land surface-atmosphere exchange” models are the parameterizations typically used on

the surface of global circulation models, which due to computational limitations only allow highly simplified flow information within the canopy layer.

The next level of complexity in canopy modeling is obtained from the numerical solutions of the RANS equations for the flow field and the Reynolds-averaged conservation equations for temperature and any other scalars of interest, assuming steady-state and horizontally homogeneous conditions. In this case, the effect of the canopy on the flow is represented by a drag force term proportional to the plant's leaf area index and the square of the flow velocity (the proportionality constant is the drag coefficient). The solution of these equations produces one-dimensional flow and scalar field statistics, and requires the use of closure models for the vertical turbulent flux terms ($\overline{w's'}$, where w is vertical velocity, s is velocity or any scalar, overbar and primes represent the mean and perturbation parts of the Reynolds average, which can be a time, spatial or ensemble average). The simplest approach is to use an eddy-viscosity model (or eddy-diffusivity model for scalars), in which $\overline{w's'} = -K\partial\bar{s}/\partial z$ (z is height), i.e., the vertical turbulent flux is proportional to the mean vertical gradient and the proportionality parameter is the eddy viscosity (or eddy diffusivity). This first-order closure (also known as flux-gradient or K -theory) assumes that the vertical turbulent flux is local, i.e., it depends only on the local gradient, which is well-known to fail in the canopy region due to the dominant non-local transport caused by the coherent structures (Wilson and Shaw, 1977). In spite of that, the simplicity of this closure makes it an attractive option if its limitations are carefully taken into account (Finnigan et al., 2015). Better results are obtained when second-order closure models (SOCMs) are used, in which additional equations for the fluxes are solved (instead of resorting to eddy-diffusivity parameterizations). However, these extra equations present third-order terms (the closure-problem of turbulence), which are then modeled using eddy-diffusivity type models (Katul and Albertson, 1998; Massman and Weil, 1999; Wilson and Shaw, 1977). SOCM has the advantage of providing, in addition to the mean quantities, the profiles of variances and vertical fluxes, which can be used in dispersion problems, for example. The SOCM developed by Massman and Weil (1999) also provides profiles of turbulent intensities, dissipation rates, Lagrangian time scale and turbulent diffusivities. The final set of equations (typically five for the flow field plus three for each scalar) are iteratively solved, and a set of adjustable constants (one for each equation) needs to be obtained from experimental data. In

addition, boundary conditions at the top of the canopy are needed for all variables represented. Although SOCM is already a significant improvement from first-order closure in canopy flows, the fact that turbulence is non-Gaussian in the canopy layer motivated the development of third-order closure models (TOCM), which correspond to solving the governing equations of the triple correlation terms by parameterizing the correlations of fourth order (Katul and Albertson, 1998). As expected, the number of equations and constants to be adjusted (and consequently the computational cost) increases significantly in SOCM and TOCM, especially if multiple scalar species are represented, and the final choice between different closure schemes needs to be based on the specific application and the cost-benefit relation of using each model. For example, Juang et al. (2008) found that first-order closure was sufficient to represent seasonal and inter-annual variations in scalar fluxes, whereas SOCM improved scalar concentration profiles within the canopy and TOCM did not provide any gain in terms of scalar concentration and flux within a forest. In large-scale models, first-order closure is typically preferred due to the low computational cost, but higher-order closures have been used in studies interested in the specific impact of canopy on the atmosphere (e.g. Weather Research and Forecasting model study with canopy represented by TOCM by Xu et al. (2015)).

As discussed by Deardorff (1978), the use of homogeneous RANS and scalar conservation equations with higher-order closures is not ideal for dispersion studies in the ABL, as all closures rely on flux-gradient relations that are not valid when non-local fluxes are present. This is particularly problematic in the case of scalars with distributed sources and sinks within the canopy, as the length scales of mean concentration gradients can become significantly smaller than the size of the most energetic eddies (which scales with the height of the canopy), violating the flux-gradient assumption (Raupach, 1989a). This scenario led to the development of Lagrangian stochastic models (LSM), in which the dispersion of scalars is obtained from the statistics of random paths of thousands of tracers present in a flow field with prescribed turbulence statistics (Wilson and Sawford, 1996). In the case of plant canopies, LSM has been used to represent dispersion of scalars (Balocchi, 1992; Poggi et al., 2006; Reynolds, 1998) and particles (Aylor and Flesch, 2001; Gleicher et al., 2014) in one- (Balocchi, 1992; Rodean, 1995), two- (Aylor and Flesch, 2001) and three-dimensional (Gleicher et al., 2014; Poggi et al., 2006) fields. These studies typically assume horizontally-homogeneous Gaussian turbulence, limiting the flow

statistics to first- and second-order moments. Because turbulence statistics inside the canopy are highly non-Gaussian, the inclusion of non-Gaussian statistics has been tested but no significant improvement was observed (Flesch and Wilson, 1992; Reynolds, 2012). The main advantage of using LSM is that it accounts for the non-local turbulent fluxes caused by coherent eddies, through the persistence that exists in the trajectories during times smaller than the Lagrangian timescale of the flow (Balocchi, 1992). Besides flow statistics (mean, standard deviation and Lagrangian timescale), the model requires specification of sources' location and intensity. For cases in which sources and concentrations are coupled (such as heat and water vapor within the canopy), Raupach (1989a) developed a Lagrangian dispersion matrix capable of simultaneously solving source and concentration fields (a method known as "localized near-field theory"), a useful tool for coupling the flow field with plant biophysical models (Gu et al., 1999) and for deriving source distributions from concentration profiles (known as the "inverse-problem") (Raupach, 1989a; Siqueira et al., 2000). The downside of the LSM approach is the dependency on higher-order velocity statistics that are not always easy to obtain (Juang et al., 2008).

At the other extreme of complexity of canopy-flow simulations, there is the three-dimensional numerical solution of the filtered Navier-Stokes equation using the Large-Eddy Simulation (LES) technique. LES explicitly resolves the large scales of the flow, which are more energetic and anisotropic, while the small, more isotropic and dissipative scales are filtered out and parameterized (Moeng, 1984). LES is a powerful tool in simulating canopy flows because it explicitly generates the coherent eddies that are most relevant and hard to represent by other modeling approaches. Similarly to RANS, in LES the effect of the canopy on the flow is represented by a drag force. Together with field and wind-tunnel experimental data, LES results have been fundamental to the advancement of knowledge of three-dimensional turbulence and dispersion within the canopy and in the roughness sublayer. However, due to the high computational cost, most LES with resolved canopy have a domain with sizes on the order of the ABL surface layer (as found in Albertson et al., 2001; Dwyer et al., 1997; Huang et al., 2013; Pan et al., 2014; Su et al., 1998), and only very recently a simulation resolving the canopy flow and the entire ABL simultaneously has been performed (Patton et al., 2016). Hence, with the increasing demand for inclusion of complex processes (such as chemical

reactions and particle dispersion) combined with the use of large domains and higher resolutions close to the surface, the technique is currently limited by the computational power available, creating an opportunity for the development of alternative modeling approaches.

As described thus far, the characterization and modeling of turbulent transport in the canopy roughness sublayer still has room for improvement. In the present work, two aspects of the problem are explored: (i) the characterization of turbulent transport efficiency within the canopy using field experiment data and simple theoretical models, in order to identify situations in which turbulence can potentially impact chemical and biophysical processes happening locally; and (ii) the development of a general, low-cost modeling approach capable of representing canopy flows with non-local turbulent fluxes and multiple scalar fields (including their coupled source/sink and concentration profiles), for different atmospheric stabilities and with little requirement of case-specific information. The first topic is discussed in Chapter 2 and the second one in Chapters 3 and 4.

In the work presented in Chapter 2, a year-long turbulence dataset measured in the Amazon rainforest is used to characterize turbulence transport efficiency within the canopy. The turbulent flow is classified as having poorly, partially or well-mixed conditions based on measured levels of local mixing of ozone. This classification leads to the definition of a turbulent mixing timescale (i.e., the time required to achieve well-mixed conditions). The data set is used to characterize this timescale as a function of height within the canopy and time-of-day. The mixing timescale information is useful because when chemical and biophysical processes happen slower than the turbulent mixing, they can be assumed to occur in a well-mixed environment and their results are independent from the details of the turbulent flow. However, when timescales are comparable, turbulence needs to be taken into account. Since most chemical and biophysical processes happening in the canopy environment depend on the diurnal cycle and depth into the canopy, the turbulent mixing timescale information provided on this spatiotemporal scale can be valuable information for many fields of study.

In Chapter 3, a new modeling approach for the ABL with plant canopies is proposed and tested. The one-dimensional turbulence (ODT) model developed by Kerstein (1999) is used, in which a time-evolving diffusion process simulated along a line is superposed with the effects of stochastic eddies mimicking three-dimensional

turbulence. This modeling approach has been successfully used to represent homogeneous turbulence, shear flows, and buoyant stratified flows (Kerstein, 1999), free-shear flows (Kerstein et al., 2001), turbulent jet diffusion flames (Echekki et al., 2001), profiles of the stable ABL (Kerstein and Wunsch, 2006), and particle transport within a turbulent flow (Schmidt et al., 2009; Sun et al., 2014). In this work we adapt the ODT model to a “LES mode”, in which the large scales of the flow are simulated, and a subgrid-scale model is used to parameterize the small scales. This ODT version behaves as a low-cost homogeneous LES, as it provides instantaneous profiles of the resolved flow and scalar fields, including the effects of atmospheric stability and presence of plant canopies. This modeling approach has the potential to be the most general and realistic one-dimensional representation of canopy flows, given that, as in LES, the driving forces, sources and sinks can be directly applied, non-local fluxes are represented by non-local stochastic eddies without the need of closures, and the domain can extend up to the top of the ABL. Another advantage compared to other one-dimensional canopy models is the possibility of simulating transient (non-equilibrium) conditions or converting the time dimension into the streamwise dimension, allowing the representation of two-dimensional steady-state flows (useful for plume-growth studies, for example). As disadvantages, ODT results have to be evaluated in terms of ensemble averages (due to the stochastic nature of the turbulence in the model) and there is one adjustable parameter, which reduces the independent nature of the model (although it still presents less case-specific adjustments than the other 1D models listed above). ODT also has a high computational cost compared to other 1D models, although the increase in cost when including new scalar fields is much lower compared to the increase obtained in the other models. This ABL version of ODT was tested for cases without canopy under different atmospheric stabilities (including a diurnal cycle) and for cases with canopy of four different types. It provided very promising results especially in terms of flexibility, motivating its use not only as a stand-alone option, but also as superparameterization of complex surface processes in large-scale models.

Several important and complex physical processes happen on the surface of the ABL, and the study of such processes in the context of large-scale flows is often a challenge. As already discussed, the parameterization of surface processes is an unsolved issue in all types of atmospheric modeling. Because ODT is a general

and reliable tool for turbulence modeling, it has the potential to be used as a surface parameterization for LES and large-scale models. In Chapter 4, we test this approach by performing simulations of canopy flows in which LES is used to represent the entire ABL, but with a vertical resolution coarser than the height of the canopy, and ODT is used to model the flow field in the canopy and in the roughness sublayer. This two-way coupling between ODT and LES has already been tested by Schmidt et al. (2003) to simulate smooth channel flows, in which ODT represented the viscous and buffer layers (close to the wall) and LES resolved the outer region of the flow. Here, the ODT in “LES mode” developed for ABL flows with canopy is used. This ODT-LES coupling has the potential to improve the modeling of several other complex surface-atmosphere interactions, such as chemical reactions happening in the canopy environment and the processes of emission and deposition of particles (e.g. dust, snow, pollen).

Chapter 2 |

Turbulent mixing and removal of ozone within an Amazon rainforest canopy

2.1 Introduction

The significance of the Amazon rainforest on climate and global biogeochemical cycling is rarely disputed. Current subjects of discussion and inquiry are the role of biogenic volatile organic compounds (BVOCs) (e.g. Kesselmeier et al., 2000; Jardine et al., 2015) that undergo rapid photochemical oxidation and their contribution to driving ozone dynamics in the lower atmosphere. These hydrocarbon species represent a large sink for the hydroxyl radical (OH), which is deemed crucial for the regional oxidation capacity of the atmosphere. Ozone is reactive and substantially contributes to the oxidation of terpenes (e.g. Paulson and Orlando, 1996; Aschmann et al., 2002). In the Amazon, the oxidation of BVOCs leads to numerous reaction pathways and thus influences the forest environment photoxidative capacity through the OH generation (Lelieveld et al., 2008; Gerken et al., 2016; Lelieveld et al., 2016).

Ozone mixing ratio in the atmospheric boundary layer (ABL) over the Amazon shows pronounced diurnal cycles in response to source and sink processes. Daytime increases are governed by entrainment of ozone into the ABL, efficient vertical mixing promoted by convective turbulence, and photochemical production (Gregory et al., 1988; Kirchhoff, 1988; Sigler et al., 2002). Ozone deposition onto the forest and chemical reaction with biogenic hydrocarbons dominate the dynamics of nighttime ozone mixing ratios. These nocturnal ozone sinks can be sufficiently

strong to promote complete ozone depletion in the ABL (Kirchhoff, 1988). Given that most of the ozone available for oxidation originates above the forest and the hydrocarbon emissions occur within the forest canopy, the mixing of gases promoted by turbulence plays an important role in the chemical processes occurring both within and above the forest.

The wide ranges of timescales associated with ABL and canopy turbulence on one hand, and chemistry on the other hand, invariably lead to overlaps in timescales and strong coupling between physical and chemical processes. In the absence of advection and/or deposition, if the chemical timescales are large compared to those associated with turbulent mixing, the system is mostly well-mixed and its bulk evolution is determined by the chemistry. Conversely, if turbulent mixing timescales are larger, strong segregation of chemical species occurs, reactions take place in relatively thin layers where limited mixing occurs (in this case near the top of the canopy), and the evolution of the system is determined by turbulent mixing (Hill, 1976; McRae et al., 1982; Stockwell, 1995). These processes are usually re-cast in terms of a dimensionless number, the Damköhler number $Da = \tau_{\text{mix}}/\tau_{\text{chem}}$ (Damköhler, 1940), with τ_{mix} and τ_{chem} being timescales characterizing turbulent transport (or mixing) and chemical reactions, respectively. In the specific case of interest here, ozone removal by nonchemical processes (stomatal uptake and dry deposition) with their own characteristic timescale $\tau_{\text{su,dd}}$ is also important, and the ozone dynamics within the canopy is then dependent on the relationships between these three timescales.

One issue that typically arises is the choice of timescale associated with the turbulent mixing in dense and tall forests such as the Amazon. Trumbore et al. (1990) estimated the flushing time for the entire vertical extent of the Amazon forest during the night using measurements of radon (^{222}Rn) and carbon dioxide (CO_2), obtaining 3.4 and 5.5 hours respectively (the difference being attributed to the production of CO_2 in the canopy). Martens et al. (2004) used the same approach based on radon measurements at a different site (with slightly larger canopy height) and obtained nighttime estimates between 2 and 10 hours (even though they also show estimates of daytime flushing times and cite those to reach values as small as a few minutes, no detailed analysis or discussion is presented). Simon et al. (2005) combined ^{222}Rn and the localized near-field model (Raupach, 1989a) to predict height-dependent turbulence exchange for another site in the Amazon forest.

For a height of 15 m ($z/h = 0.375$, where z is the variable representing height and $h = 40$ m is the canopy height), they obtained exchange times of 40 min for nighttime and 11 min for daytime conditions. Simon et al. (2005) conclude that convective mixing inside the canopy during nighttime is important and that typical values of exchange timescales are 10 min for daytime and 1 hour for nighttime.

In the present study, two research objectives are addressed. The first one is the definition and estimation of a turbulent mixing timescale representing the ability of turbulence in creating a well-mixed environment in the region inside the forest. This is accomplished by combining a simple one-dimensional turbulent diffusion model with a large data set of turbulence statistics inside and above the canopy. The second goal is to compare the obtained values of turbulent mixing timescales with those for chemical and nonchemical sinks of ozone inside the forest, allowing an assessment of the importance of each process to ozone mixing ratio during different periods of the diurnal cycle. Results from the current investigation can help the understanding of the impact of turbulence on the distribution of reactive gases such as ozone and biogenic hydrocarbons in the forest environment.

2.2 Methods

2.2.1 Data set

The data set used was collected during a field campaign at the Cuieiras Biological Reserve, commonly referred to as ZF2, located 60 km north-northwest of the city of Manaus, Amazonas, Brazil. The experiment was part of the GoAmazon (Observations and Modeling of the Green Ocean Amazon) 2014/5 project (Martin et al., 2016), and it is described in detail elsewhere (Fuentes et al., 2016). In summary, data were collected between March 2014 and January 2015 at the 50-m tall tower ($2^{\circ} 36' 33''$ S, $60^{\circ} 12' 33''$ W, 130 m ASL, labeled as T_{0k} for the GoAmazon campaign) located on top of a plateau and surrounded by a dense primary forest. Canopy height at the measurement site varied between 30 and 40 m, with leaf area index (LAI) estimated to be between 5.7 and $7.3 \text{ m}^2 \text{ m}^{-2}$ (McWilliam et al., 1993; Marques Filho et al., 2005; Tóta et al., 2012). Hereafter, $h = 35$ m is used as the mean canopy height and LAI = 6.0 is adopted as a representative value. At the site, the prevailing wind direction was from the northeast, a direction covered

Table 2.1. Vertical location of the ten sonic anemometers and number of data blocks used in the analyses for the current study. Canopy height $h = 35$ m is used.

Height z [m]	Number of 30-min data blocks	
	z/h	
1.5	0.04	5,138
7.0	0.20	5,801
13.5	0.39	5,820
18.4	0.52	5,537
22.1	0.63	5,757
24.5	0.70	7,076
31.6	0.90	6,875
34.9	1.00	7,014
40.4	1.15	7,694
48.2	1.38	7,633

mostly by undisturbed forest. High frequency time series of the three wind velocity components within and immediately above the canopy were continuously measured by ten triaxial sonic anemometers (model CSAT3, Campbell Scientific Inc, Logan, UT) from March 23, 2014 to January 16, 2015. Measurement frequency was 20 Hz, and all sensors were facing the east direction on the 50 m tower. The sensors were vertically deployed in an array designed to sample the vertical structure of turbulence inside the canopy (see Table 2.1).

Ozone mixing ratios (and other trace gases) above the canopy were continuously measured throughout the experiment. An air-inlet was placed at a height of 40 m above the ground ($z/h = 1.15$) on the tower. A pump (KNF Neuberger, Baden-Württemberg, Germany) drew ambient air through a Teflon tubing (1.9-cm outer diameter, OD) to the gas analyzers which were housed in an environmentally controlled hut located 5 m from the base of the tower. Foam pipe insulation (1.9-cm wall thickness) covered the Teflon tubing to minimize actinic irradiance reaching the air in the tube. The air inlet had a filter holder and a Teflon membrane (1 μm pore size) to keep the inside of the tubing free of dust and pollen. The filter membrane was replaced on a weekly basis. Flow rate through the Teflon tube was $22 \times 10^3 \text{ cm}^3$ per minute. This flow rate resulted in an air residence time in the air sampling tube of about 2.5 minutes. Inside the hut, a pyrex manifold unit with several outlet ports allowed the ambient air to pass through the gas analyzers. Tubing and air manifold remained heated at a constant temperature to

prevent condensation. The ozone analyzer (model 49i, Thermo Fisher Scientific Inc, Waltham, MA) sub-sampled air from the manifold at the flow rate of $1.5 \times 10^3 \text{ cm}^3$ per minute. During October, November, and December of 2014, several days were selected to perform vertically resolved measurements of mean ozone mixing ratios within the canopy. A roving sampling system was designed to carry the air inlet up and down along the 50 m tower. At the beginning of a profile measurement, the intake was moved to the top position (at 50 m height), and measurements were sequentially taken at every descending 5 m until the bottom position located at 5 m above the ground was reached. Ambient air was sampled for 5 minutes at each level, and the movement of the intake to each subsequent height required about 10–15 seconds. The measurements were recorded at 1 Hz frequency, and the start and end times were logged from each level. Seventy ozone profiles were obtained between October 5 and December 6, 2014.

Concurrent to ozone observations, nitric oxide (NO) measurements (model 43i-TLE, Thermo Fisher Scientific, Waltham, MA) were made at 40 m above ground. In the absence of biomass burning, the NO levels at the study site remained below 0.4 ppb (similar NO levels were recorded in another study where mean NO mixing ratios were $0.035 \pm 0.032 \text{ ppb}$ (Liu et al., 2016)). In addition, a Proton Transfer Reaction-Mass Spectrometer (PTR-MS, Ionicon Analytik Ges.m.b.H., Innsbruck, Austria) measured ambient levels of hydrocarbon compounds. The PTR-MS only characterizes compounds and fractions of compounds by molecular weight, and the identities of the hydrocarbons measured should be considered putative with the exception of isoprene, with mass (m) and charge number of ions (c) ratio (m/c) of 69. A dynamic dilution technique allowed the PTR-MS calibration for the measured compounds that was applied before, during, and after the measurement campaign.

To complement the ozone profile measurements, profiles of monoterpenes and sesquiterpenes measured during the BrazilianAir 2010 Field Campaign and reported by Jardine et al. (2011, Figure 3a,b) are also used here. Measurements were taken at six levels ($z = 2, 11, 17, 24, 30$, and 40 m) at a site less than 2 km away from the K34 tower between the months of September and December, 2010. Profiles of isoprene from the same experiment were obtained from Alves et al. (2016, Figure 2a). In addition to these profiles, vertically averaged mixing ratios inside the forest were independently estimated from their data and are presented in Table 2.2.

Table 2.2. Approximate values of vertically averaged mixing ratios of isoprene, monoterpenes, and sesquiterpenes obtained from Jardine et al. (2011) and Alves et al. (2016)

Species	Symbol	Ozone reaction rate coefficient [cm ³ molecule ⁻¹ s ⁻¹]	Daytime [ppbv]	Nighttime [ppbv]
Isoprene	$\overline{[\text{ISOP}]_{avg}}$	^a $k_{[\text{ISOP}]} = 1.28 \times 10^{-17}$	2.820	0.815
Monoterpenes	$\overline{[\text{MT}]_{avg}}$	^b $k_{[\text{MT}]} = 1.82 \times 10^{-16}$	0.750	0.200
Sesquiterpenes	$\overline{[\text{SQT}]_{avg}}$	^c $k_{[\text{SQT}]} = 1.00 \times 10^{-14}$	0.160	0.220

^a Atkinson (1997) for temperature of 300 K

^b Weighted geometric mean of monoterpene species reported by Jardine et al. (2015) and rates from Atkinson et al. (1999)
^c Following Jardine et al. (2011) we use the rate constant for β -caryophyllene from Shu and Atkinson (1994)

2.2.2 Data analysis

Turbulence data were divided into 30-minute blocks and error flags produced by the sonic anemometer were monitored. Blocks with more than 1 second of consecutive error flags were eliminated from further analysis. These error flags occurred frequently due to precipitation or obstruction of the sonic path by plant elements. Only blocks corresponding to the sensors impacted by error flags were removed, producing an uneven distribution in the number of ‘acceptable’ blocks with height. In the remaining data set, the rare cases of measurements flagged with error were replaced by the previous acceptable measurement. To avoid contaminating turbulence statistics with flow distortion caused by the presence of the tower, data blocks with mean wind direction with a western component were discarded (i.e. only blocks corresponding to mean wind directions with an angle within $\pm 90^\circ$ of the instrument axis were used). For this purpose, the wind direction at the highest measurement ($z/h = 1.38$) was used and the blocks from all heights were discarded when the criterion was not satisfied. The total number of blocks remaining for each height is presented in Table 2.1. Finally, the vertical velocity time series were filtered using a Gaussian filter with a window of 3 minutes to eliminate low-frequency non-turbulent oscillations that can be significant during nighttime periods (e.g. Campos et al., 2009; Santos et al., 2016) and can lead to large integral timescales that are not associated with turbulence.

In prior work, the degree of mixing inside the canopy has been empirically correlated to the friction velocity (u_*) at the top of the canopy (e.g. Pleijel, 2008) and the vertical velocity variance, σ_w^2 (Thomas et al., 2013). The premise is that u_* at the canopy top is related to the mechanical production of turbulent kinetic energy ($\sim u_*^3$) whereas σ_w is related to the turbulent kinetic energy component directly responsible for vertical mixing. Here, the eddy diffusivity ($K(z)$) is used as a proxy for the vertical mixing capacity of turbulence. While different estimates of eddy diffusivity exist (e.g. $l_m^2 |\partial \bar{u} / \partial z|$, where l_m is a mixing length and $|\partial \bar{u} / \partial z|$ is the mean velocity gradient), the expression

$$K(z) = \sigma_w^2(z) T_L(z) \quad (2.1)$$

is selected here as derived for the far-field diffusion regime defined by Taylor (1922), where $T_L(z)$ is a characteristic timescale representing the coherency of the

momentum transporting eddies. This description of $K(z)$ ensures that turbulent diffusivity is positive within the canopy and can readily accommodate the zero-mean gradient flow conditions ubiquitous to canopy flows. However, the definition of $T_L(z)$ requires further clarification. In the original Lagrangian diffusion theory, $T_L(z)$ must be interpreted as a Lagrangian turbulence timescale. One commonly used estimate suggests that $T_L(z) \sim h/u_*$ is a constant within the canopy but increases linearly above the canopy (Raupach, 1989a; Poggi et al., 2006). This estimate partly shows that $K(z) \sim (\sigma_w(z)/u_*)\sigma_w(z)h$ accommodates both u_* and σ_w as flow variables when establishing the degree of mixing. Other estimates of $T_L(z)$ employ well-established relations between Eulerian and Lagrangian integral timescales (Corrsin, 1963; Angell et al., 1971; Hanna, 1981; Koeltzsch, 1998; Anfossi et al., 2006; Poggi et al., 2008). The Eulerian integral timescale of w , $T_E(z)$, is computed by numerically integrating the autocorrelation function of w up to its first zero-crossing (e.g., see Sreenivasan et al., 1978; Lenschow and Stankov, 1986; Chamecki, 2013). Here, a simplified relation obtained from Lagrangian and Eulerian expressions for second-order structure functions based on the approach outlined by Poggi et al. (2008) is used and yields

$$T_L(z) = \frac{C_2^{3/2}}{\sqrt{2}C_0}\frac{\bar{u}(z)}{\sigma_w(z)}T_E(z), \quad (2.2)$$

where $C_2 \approx 2.8$ and $C_0 \approx 5.5$ are universal constants (see Appendix 2.A for a derivation of this relation).

Last, it is to be noted that ozone is a reactive gas and that for application to ozone exchange the eddy diffusivity may be different from that for a passive tracer. As noted by Lamb (1973), the issue is well characterized by the timescales of turbulence and chemistry. This correction can be incorporated by introducing a Schmidt number Sc , and its importance can be estimated using the simple modeling framework developed by Hamba (1993) which yields $Sc_{O_3} = K/K_{O_3} = (1 + \tau_{\text{eddy}}/\tau_{\text{chem}})$. It is important to realize that τ_{eddy} is different from τ_{mix} , as the former is the turbulent timescale associated with eddies that contribute the most to the turbulent fluxes and the latter is the timescale for the ozone profile to reach a well-mixed condition. Our estimates using $\tau_{\text{eddy}} = h/(3u_*)$ (Patton et al., 2001) suggest that $1.00 \leq Sc_{O_3} \leq 1.11$ for conditions representative of more than 95% of our data. Hereafter, this effect is included in the analysis by using a constant

Schmidt number $Sc_{O_3} = 1.08$ based on observational data of ozone fluxes under low NO_x concentrations by Launiainen et al. (2013). The final expression for estimating the ozone eddy diffusivity from field data is given by

$$K_{O_3}(z) = \frac{C_2^{3/2}}{\sqrt{2}C_0Sc_{O_3}}\bar{u}(z)T_E(z)\sigma_w(z). \quad (2.3)$$

For simplicity in the notation used in this manuscript, hereafter we refer to K_{O_3} as K , and we emphasize that the difference between the eddy diffusivities for O₃ and a passive scalar is constant and much smaller than the variability of K and the errors associated with its estimation.

The mean ozone mixing ratios $\overline{[O_3]}$ (henceforth the word *mean* is omitted) were obtained by averaging over 4.5 minutes at each level. The first 30 seconds at each level were discarded to avoid contaminating the mean values with air sampled while the air intake was in transit. Each profile was labeled with the time at which the profile measurement was initiated (i.e. the time when the sample at $z/h = 1.43$ was collected). Note that the true time for the lowest sample is about one hour later. The averaging time of 4.5 minutes is short and the presence of random errors in the estimates of the mean mixing ratios is likely not negligible (we estimated relative random errors in the estimates of mean ozone concentrations to be within 10% based on measurements above the canopy top). However, this is a reasonable compromise between required averaging time at each level and the total time needed for the execution of the entire profile sampling.

To accompany the analysis of the ozone profiles, a second set of vertical velocity statistics was calculated employing averaging periods consistent with the ozone sampling durations. An estimated eddy diffusivity was paired to each mean ozone mixing ratio measurement even though the heights were slightly different (ozone measurements at $z/h = 0.29, 0.43, 0.57, 0.71$, and 0.86 were paired with turbulence measurements at $z/h = 0.39, 0.52, 0.63, 0.70$, and 0.90 , respectively). This eddy diffusivity was based on a 10-minute block designed to end simultaneously with the 4.5-minute block used for the ozone (note that here the true time of ozone sampling at each height was used in determining the appropriate window of time for averaging the turbulence). The choice of 10-minute blocks for the turbulence was based on an assessment that the uncertainty in the integral scale was too large for shorter averaging times (and it was more reasonable to include turbulence data

before the ozone sampling than after, since only the former can impact measured ozone mixing ratio).

2.2.3 Mass balance of ozone inside the canopy

A mass balance approach was employed to extract characteristic timescales associated with ozone transport and sources/sinks from the measurements described above. For simplicity and data limitations, the net result of chemical production and destruction ($R_{\text{chem}}(z)$), stomatal uptake ($D_{\text{su}}(z)$), and dry deposition ($D_{\text{dd}}(z)$) were lumped together into a single source/sink term $S(z)$. Thus, upon assuming horizontal homogeneity, zero mean vertical velocity and negligible molecular diffusion, the mass balance for the ozone mixing ratio can be expressed as (e.g., see Rummel et al., 2007; Launiainen et al., 2013)

$$\frac{\partial \overline{[\text{O}_3]}}{\partial t} = -\frac{\partial \overline{w'[\text{O}_3]'}}{\partial z} + S(z). \quad (2.4)$$

If the eddy diffusivity model is invoked to parameterize the ozone kinematic turbulent flux, then

$$\frac{\partial \overline{[\text{O}_3]}}{\partial t} - K \frac{\partial^2 \overline{[\text{O}_3]}}{\partial z^2} - \frac{\partial K}{\partial z} \frac{\partial \overline{[\text{O}_3]}}{\partial z} = S(z). \quad (2.5)$$

This buuget yields a non-homogeneous partial differential equation for the mean ozone mixing ratio that can be solved for given $K(z)$, a closure model linking $S(z)$ to $\overline{[\text{O}_3]}$, and appropriate initial and boundary conditions. The approach sought here is to employ two approximations to Equation (2.5) as a means to obtain timescales associated with (i) turbulent mixing, (ii) chemical destruction, and (iii) vertically-integrated nonchemical removal processes. A discussion of the applicability of the eddy diffusivity approach in the present application is deferred to subsection 2.2.3.4.

2.2.3.1 Turbulent mixing timescale

The homogeneous solution to Equation (2.5) (i.e. the one obtained when setting $S = 0$) represents the time evolution of the ozone mixing ratio due to turbulent mixing in isolation. The turbulent mixing timescale can be obtained by solving the homogeneous equation for an idealized scenario in which an initial ozone mixing ratio

is zero everywhere except at $z/h = 1$ (layer across which ozone enters the canopy volume), where it assumes a known fixed value $\overline{[O_3]}_h$. It is to be noted that if this concentration value is set to unity, then the desired homogeneous solution becomes the well-known Green's function of Equation (2.5). For simplicity and analytical tractability, the term including the vertical variation of $K(z)$ in Equation (2.5) is neglected. To reconcile a solution using a constant eddy diffusivity with one impacted by vertical variations in $K(z)$, an equivalent eddy diffusivity $K_{\text{eq}}(z_1)$ may be defined. We define two equivalent diffusivities that we infer to represent upper and lower bounds on the solution with a varying $K(z)$ (see Appendix 2.B for more details). The first definition, which can be considered as an upper bound on the eddy diffusivity, simply uses the average eddy diffusivity between the target height z_1 and the top of the canopy

$$K_{\text{eq},1}(z_1) = \frac{1}{(h - z_1)} \int_{z_1}^h K(z) dz. \quad (2.6)$$

The second definition, which is interpreted as a lower bound in the eddy diffusivity, makes use of a resistances-in-series analogy with the resistance to transport across an infinitesimal layer being given by $dz/K(z)$. Thus, the average resistance between target height z_1 and the top of the canopy is

$$\frac{1}{K_{\text{eq},2}(z_1)} = \frac{1}{(h - z_1)} \int_{z_1}^h \frac{dz}{K(z)}. \quad (2.7)$$

Thus, Equation (2.5) is reduced to

$$\frac{\partial \overline{[O_3]}}{\partial t} = -K_{\text{eq}}(z_1) \frac{\partial^2 \overline{[O_3]}}{\partial z^2}, \quad (2.8)$$

where $K_{\text{eq}}(z_1)$ can be $K_{\text{eq},1}(z_1)$ or $K_{\text{eq},2}(z_1)$. When Equation (2.8) is integrated between the top of the canopy and the target height z_1 , $K_{\text{eq}}(z_1)$ is treated as a constant. This approach assumes a different value for each target height z_1 . In this way, the vertical variation of $K(z)$ is not completely neglected and some of its consequences are present in the final solution. Equation (2.8) is, in principle, defined in the domain $z < h$ and a solution subject to the initial condition $\overline{[O_3]}(z, t = 0) = 0$ and boundary condition $\overline{[O_3]}(z = h, t) = \overline{[O_3]}_h$ is sought. If a second boundary condition is set to be a zero ozone mixing ratio at $z \rightarrow -\infty$, then the problem is analogous to the classical fluid mechanics solution for an impulsively started

infinite plate in a fluid at rest often referred to as the Stokes' first problem (e.g., see Batchelor, 2000; Kundu et al., 2012). In the present case, it is more appropriate to set a zero ozone flux at $z = 0$ as the lower boundary condition (formally setting the domain of the solution to be $0 < z < h$). In this case, the transient solution for the ozone mixing ratio inside the canopy can be expressed as (Liu, 2008)

$$\frac{\overline{[O_3]}}{[O_3]_h}(z, t) = 1 - \sum_{n=0}^{\infty} \frac{4}{(2n+1)\pi} \exp\left\{-\left[\frac{(2n+1)\pi}{2}\right]^2 \frac{K_{\text{eq}}(z)t}{h^2}\right\} \sin\left[\frac{(2n+1)\pi}{2} \frac{(h-z)}{h}\right], \quad (2.9)$$

where z_1 is now replaced by a generic height z for convenience. A height-dependent turbulent mixing timescale $\tau_{\text{mix}}(z)$ can be obtained from Equation (2.9) by finding the time required for the ozone mixing ratio to reach a certain fraction of the imposed value at the top of the forest. In the present application, $\tau_{\text{mix}}(z)$ is defined as the time required for $\overline{[O_3]}(z)/[O_3]_h = 0.86$ (the choice of this value is justified in Section 2.3.1).

In practice, Equation (2.9) cannot be rearranged to yield an explicit solution for $t = \tau_{\text{mix}}$. An iterative method is necessary and was applied with t being increased in increments of 0.1 seconds from zero until $\overline{[O_3]}/[O_3]_h$ reached 0.86, yielding an estimate for $\tau_{\text{mix}}(z)$. The truncation of the infinite summation was done so that inclusion of additional terms did not have a contribution larger than 0.1% in the value of $\overline{[O_3]}/[O_3]_h$.

As a final note, the two equivalent eddy diffusivity models $K_{\text{eq},1}(z_1)$ and $K_{\text{eq},2}(z_1)$ are interpreted here as upper and lower bounds on the mixing produced by the vertically variable eddy diffusivity. Therefore, they yield lower and upper bounds on the mixing timescales, respectively (see Appendix 2.B for more details).

2.2.3.2 Ozone chemistry timescale

Due to the strong attenuation of actinic irradiance by the forest crown and the low nitrogen oxides ($\text{NO}_x = \text{nitric oxide (NO)} + \text{nitrogen dioxide (NO}_2\text{)}$) mixing ratios within the forest canopy, photochemical production of ozone is likely to be negligible. For typical mixing ratios of isoprene, monoterpenes, and sesquiterpenes in the Amazon forest, the oxidation of sesquiterpenes represents the largest ozone

sink (Jardine et al., 2011). Nevertheless, for the sake of completeness, oxidation of monoterpenes and isoprene are also included. Therefore, the chemical sink term is modeled as

$$R_{\text{chem}}(z) = - \left[k_{[\text{ISOP}]}^{\text{eff}} \overline{[\text{ISOP}]}(z) + k_{[\text{MT}]}^{\text{eff}} \overline{[\text{MT}]}(z) + k_{[\text{SQT}]}^{\text{eff}} \overline{[\text{SQT}]}(z) \right] \overline{[\text{O}_3]}(z), \quad (2.10)$$

where $\overline{[\text{ISOP}]}$, $\overline{[\text{MT}]}$, and $\overline{[\text{SQT}]}$ are the mean mixing ratios of isoprene, monoterpenes, and sesquiterpenes, respectively. Additionally, the effective reaction rate constant for the reaction of the chemical species $[\text{A}]$ with ozone is defined as

$$k_{[\text{A}]}^{\text{eff}} = k_{[\text{A}]}(1 + I_{S,[\text{A}]}), \quad (2.11)$$

where $k_{[\text{A}]}$ is the true reaction rate constant for the reaction and $I_{S,[\text{A}]} = \frac{\overline{[\text{A}']}[\text{O}_3']}{(\overline{[\text{A}]}[\text{O}_3])}$ is the intensity of segregation between spatial distributions of ozone and $[\text{A}]$ (e.g., see Schumann, 1989; de Arellano et al., 1993). The rate constants for the reactions of isoprene, monoterpenes and sesquiterpenes with ozone are needed (see Table 2.2). Hereafter we use the notation $k^{\text{eff}} \overline{[\text{BVOC}]}(z)$ to represent the sum of the three terms inside square brackets in Equation (2.10) and define a time timescale associated with the ozone loss in the oxidation of the BVOCs as

$$\tau_{\text{chem}}(z) = \frac{1}{k^{\text{eff}} \overline{[\text{BVOC}]}(z)}. \quad (2.12)$$

The intensity of segregation cannot be determined from the measurements available as this would require simultaneous, high-frequency measurements of the two species involved. While the intensity of segregation between isoprene and OH may be significant (e.g. Kaser et al., 2015), the reactivity between ozone and terpenes is much lower (due to the much lower ambient levels of terpenes compared to isoprene) and segregation effects are expected to be much smaller (e.g., see Ouwersloot et al., 2010). These effects are neglected hereafter and the approximation $k_{[\text{A}]}^{\text{eff}} \approx k_{[\text{A}]}$ is employed.

2.2.3.3 Ozone nonchemical removal timescale

In addition to turbulent mixing and chemical destruction, the processes of stomatal uptake and dry deposition can be taken into account together in the estimation

of a nonchemical ozone removal. For that, the mass balance of ozone within the canopy (Equation (2.5)) is now considered. In principle, the profile of source/sink $S(z)$ can be estimated from data as the residual of the three terms on the left hand side of Equation (2.5). All the three terms can be estimated directly from mean ozone mixing ratio profiles and turbulence data, and the nonchemical sinks can be obtained by removing the chemical contribution to the residual. However, estimating the profile of $S(z)$ from observed mean mixing ratio profiles is difficult even for passive scalars (Siqueira et al., 2000). For this reason, the present analysis follows a different approach limited to determine a timescale associated with the total sink integrated over the entire height of the forest. Vertical profiles of eddy diffusivity and mean ozone mixing ratio are used in the determination of a vertical ozone flux profile (see Appendix 2.C for more details) and the mean ozone flux at the top of the canopy is then used in the calculation of a bulk deposition velocity at canopy top

$$V_S = -\frac{\overline{w'[\text{O}_3]'}_h}{[\text{O}_3]_h}. \quad (2.13)$$

The bulk deposition velocity V_S includes all sink processes, namely chemical loss, stomatal uptake and dry deposition. Here we split V_S into the components associated with chemical loss (V_{chem}) and nonchemical removal processes (stomatal uptake plus dry deposition, $V_{\text{su,dd}}$)

$$V_S \approx \underbrace{\bar{g}\text{LAI}}_{V_{\text{su,dd}}} + \underbrace{k\overline{[\text{BVOC}]}_{\text{avg}}h}_{V_{\text{chem}}}, \quad (2.14)$$

where \bar{g} is an average canopy conductance, $\overline{[\text{BVOC}]}_{\text{avg}}$ is the mean mixing ratio of BVOCs averaged within the vertical extent of the canopy and by definition $\text{LAI} = \int_0^h a(\xi)d\xi$. More details related to the assumptions leading from (2.13) to (2.14) are given in Appendix 2.C. Following Rannik et al. (2016), timescales can be defined from deposition velocities as $\tau = h/V$. The partitioning of the deposition velocity, given by Equation (2.14), yields a timescale for the chemistry which is in agreement with (2.12) and a nonchemical removal timescale given by

$$\tau_{\text{su,dd}} = \frac{h}{V_{\text{su,dd}}}. \quad (2.15)$$

Note that $\tau_{\text{su,dd}}$ is a timescale associated with the vertically integrated loss of ozone

due to stomatal uptake and dry deposition. As Equation (2.15) is used to estimate the order of magnitude of $\tau_{\text{su,dd}}$ rather than exact values, the assumptions required to progress from (2.13) to (2.15) are likely justifiable.

2.2.3.4 Applicability of the eddy diffusivity model

The use of eddy diffusivity closures to model fluxes within plant canopies has received much criticism (e.g., Finnigan, 2000). Its applicability is in fact dependent on the characteristics of the mean concentration profile for the scalar in question (Corrsin, 1975), as well as the spatial distribution of sources and sinks. Second-order closure modeling suggests that in the present case, the magnitude of deviations from the eddy diffusivity model can be approximated by the dimensionless number (see Appendix 2.D for more details)

$$N_{GD} \sim \frac{\tau_{\text{eddy}} \overline{w'[\text{O}_3]'}_h}{h \overline{[\text{O}_3]}_h} = \frac{V_S}{3u_*}. \quad (2.16)$$

The equality follows from adopting $\tau_{\text{eddy}} = h/(3u_*)$ (Raupach, 1989b) and the definition of the deposition velocity by Equation (2.13). The eddy diffusivity approach is expected to yield a reasonable model for the fluxes if $N_{GD} \ll 1$.

2.3 Results

2.3.1 Turbulent mixing of ozone into the forest

To establish the validity of eddy diffusivity as a proxy for mixing of ozone into the canopy, three days (October 30, December 3, and December 4, 2014, with 5 profiles on each day) in which consecutive profiles of ozone mixing ratio were measured inside the forest were selected. In particular, the early morning evolution of ozone mixing ratios inside the canopy is evaluated. Early morning profiles are ideal to establish a connection between eddy diffusivities and mixing because ozone mixing ratio and turbulence inside the forest before sunrise are typically low. During this early morning period, photochemical production of ozone is limited by the low levels of both radiation and NO_x. Inside the forest, main source of ozone is transport from the air layers above the canopy. Therefore, in the morning the onset

of turbulence is key for increases in ozone mixing ratios inside the forest canopy, providing an ideal scenario for linkages between turbulence levels and mixing states. Profiles of $\sigma_w(z)$, $T_L(z)$, $K(z)$, $\overline{[O_3]}(z)$ and $\overline{[O_3]}/\overline{[O_3]}_h$ for the three selected days are shown in Figure 2.1. Low levels of turbulence, characterized by low values of $\sigma_w(z)$ and $K(z)$ were observed before 07:00 hours (local time). At these early morning times, not only ozone mixing ratios were low inside the forest, but the mean ozone mixing ratio profiles exhibited large vertical gradients as evident in the $\overline{[O_3]}/\overline{[O_3]}_h$ shown in Figure 2.1j,o. As turbulence mixing increased, mixing ratio of ozone inside the forest increased and the shape of the ozone profiles became more uniform (i.e. the ozone mixing ratios became nearly constant with height). This is particularly clear in the upper region of the canopy, $0.4 \leq z/h < 1.0$. Note that $K(z)$ for $z/h < 0.4$ is always small compared with values observed in the upper canopy, a characteristic feature of many tall and dense forests.

A strong relation between ozone mixing (characterized by $\overline{[O_3]}/\overline{[O_3]}_h$) and $K(z)$ exists in the upper canopy (Figure 2.2). The relation with $K(z)$ is even clearer than the one obtained by plotting normalized ozone mixing ratio against σ_w alone (not shown). This result lends support to the assertion that the main source of ozone in this morning period is entrainment from the region above the canopy. The pattern of the scatter in Figure 2.2 suggests an exponential form

$$\frac{\overline{[O_3]}}{\overline{[O_3]}_h} = 1 - \exp\left(-\frac{K(z)}{K_e}\right), \quad (2.17)$$

where $K_e = 0.09 \text{ m}^2\text{s}^{-1}$ is the best fit e-folding eddy diffusivity. This e-folding eddy diffusivity is used to set the limits between three distinct regimes of ozone turbulent mixing within the forest. The value $0.5K_e = 0.045 \text{ m}^2\text{s}^{-1}$ is henceforth used as the limit between poorly mixed and partially mixed regimes and $2K_e = 0.18 \text{ m}^2\text{s}^{-1}$ is used as the limit between partially mixed and well-mixed regimes. The only motivation for the curve fitting is to provide an objective determination of these regime transition limits, which are expected to be canopy-dependent. A summary of the basic characteristics of the three regimes defined here is presented in Table 2.3. Note that the threshold $\overline{[O_3]}/\overline{[O_3]}_h = 0.86$ used for the definition of τ_{mix} in Subsection 2.2.3.1 is the mixing corresponding to $2K_e$. Thus, the mixing timescale is, by definition, the time needed to achieve a well-mixed condition according to the analytical model used to represent turbulence mixing.

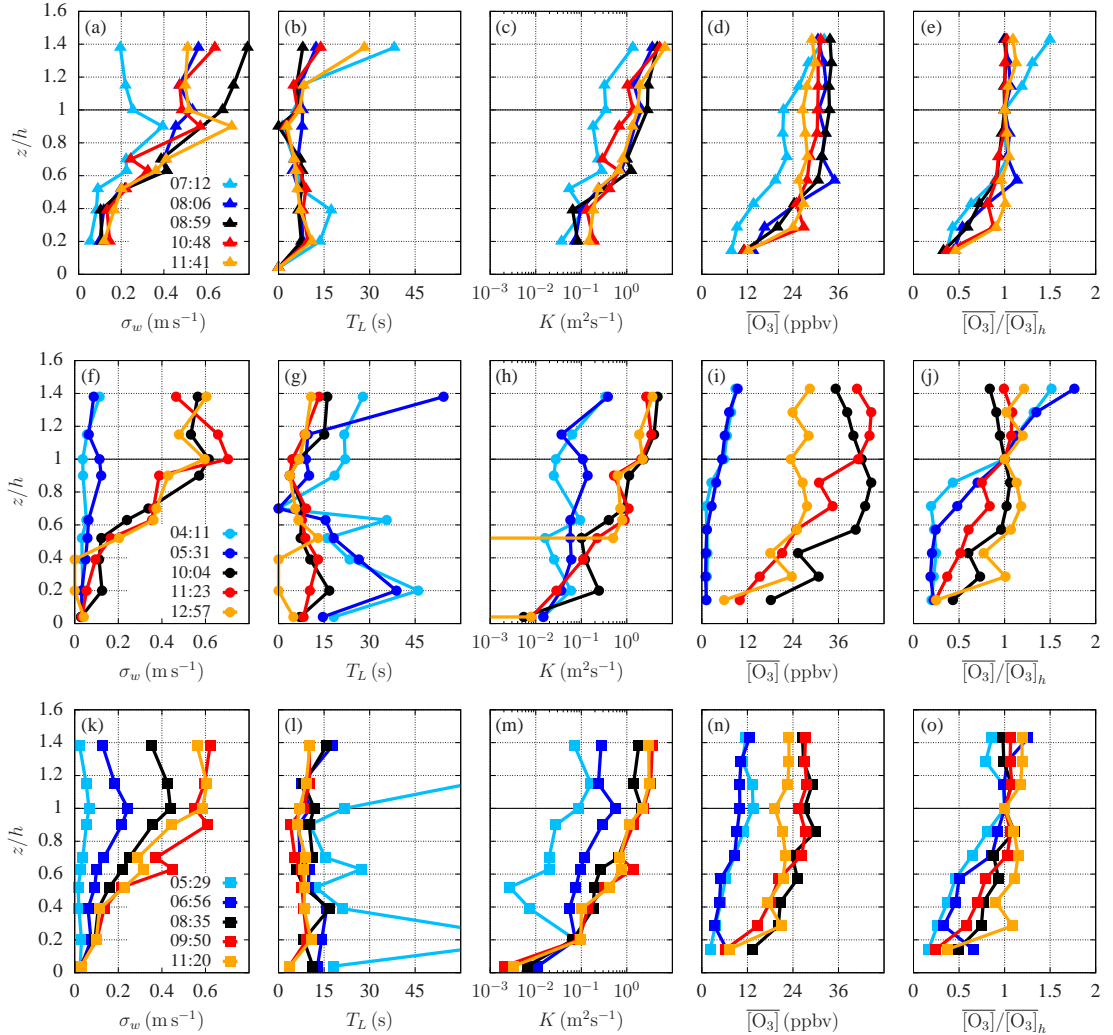


Figure 2.1. Profiles of [(a), (f) and (k)] standard deviation of vertical wind velocity (σ_w), [(b), (g) and (l)] Lagrangian integral timescale of the vertical velocity (T_L), [(c), (h) and (m)] eddy diffusivity (K), [(d), (i) and (n)] ozone mixing ratio ($\overline{[O_3]}$) and [(e), (j) and (o)] normalized ozone mixing ratio ($\overline{[O_3]}/\overline{[O_3]}_h$) for the morning transition of (a)-(e) October 30, (f)-(j) December 3, and (k)-(o) December 4, 2014.

The large spread for the poorly mixed regimes in Figure 2.2 originates mostly from early morning profiles measured on December 4, which were more mixed than the early morning profiles observed on December 3, 2014. This result can be understood when the entire nighttime evolution of the eddy diffusivity is considered (Figure 2.3). The three selected mornings were preceded by different nighttime mixing patterns. October 30 was characterized by significant mixing in the upper

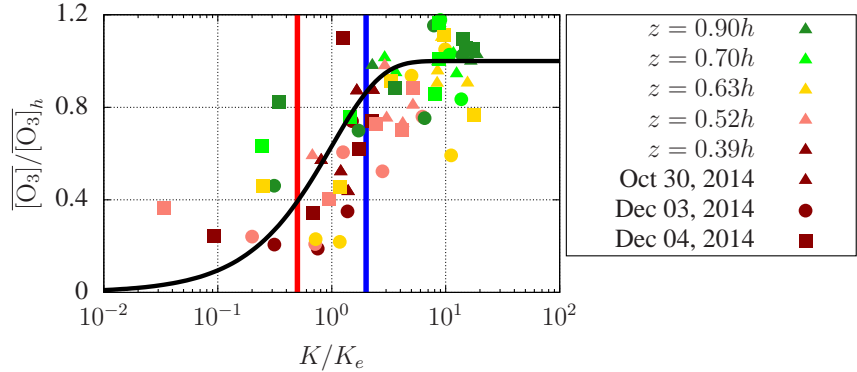


Figure 2.2. Normalized ozone mixing ratio ($\overline{[\text{O}_3]} / [\text{O}_3]_h$) as a function of eddy diffusivity normalized by the e-folding eddy diffusivity (K/K_e) for the morning transition of October 30, December 3, and December 4, 2014. Equation (2.17) (black line), $K = 0.5K_e$ (red line) and $K = 2K_e$ (blue line)

Table 2.3. Three mixing regimes defined for the Amazon rainforest canopy

Regime	Eddy diffusivity	Ozone mixing
Poorly mixed	$K < 0.045 \text{ m}^2 \text{s}^{-1}$	$\overline{[\text{O}_3]} / [\text{O}_3]_h < 0.39$
Partially mixed	$0.045 \text{ m}^2 \text{s}^{-1} \leq K < 0.18 \text{ m}^2 \text{s}^{-1}$	$0.39 \leq \overline{[\text{O}_3]} / [\text{O}_3]_h < 0.86$
Well-mixed	$K \geq 0.18 \text{ m}^2 \text{s}^{-1}$	$\overline{[\text{O}_3]} / [\text{O}_3]_h \geq 0.86$

canopy and extremely small eddy diffusivities below $z/h = 0.6$. The lower measurement heights of the ozone profile labeled as 7:12 were actually sampled closer to 8:00 hours, when mixing was much more pronounced. Interestingly, the first morning profile of December 3 was sampled in the middle of a period of extremely low eddy diffusivity, while on December 4 a significant event of enhanced diffusivity spanning the entire vertical extent of the forest took place right before the ozone measurements. This was likely the cause for a more mixed profile despite low diffusivities computed for December 4. All three days were characterized by strong mixing during the daytime, but large differences in mixing were evident after sunset, providing an example of large day-to-day variability of turbulent mixing within the Amazon forest (much stronger contrasts were observed in the data set). Analysis of the kinematic heat flux profiles within the canopy (not shown) suggest that enhanced nighttime mixing on December 3 and 4 (as compared to the very weak mixing on October 30) is associated with positive heat fluxes and, consequently, unstable thermal stratification below $z/h = 0.7$. This convective mixing is likely caused by longwave radiative cooling in the upper canopy (Kruijt et al., 2000;

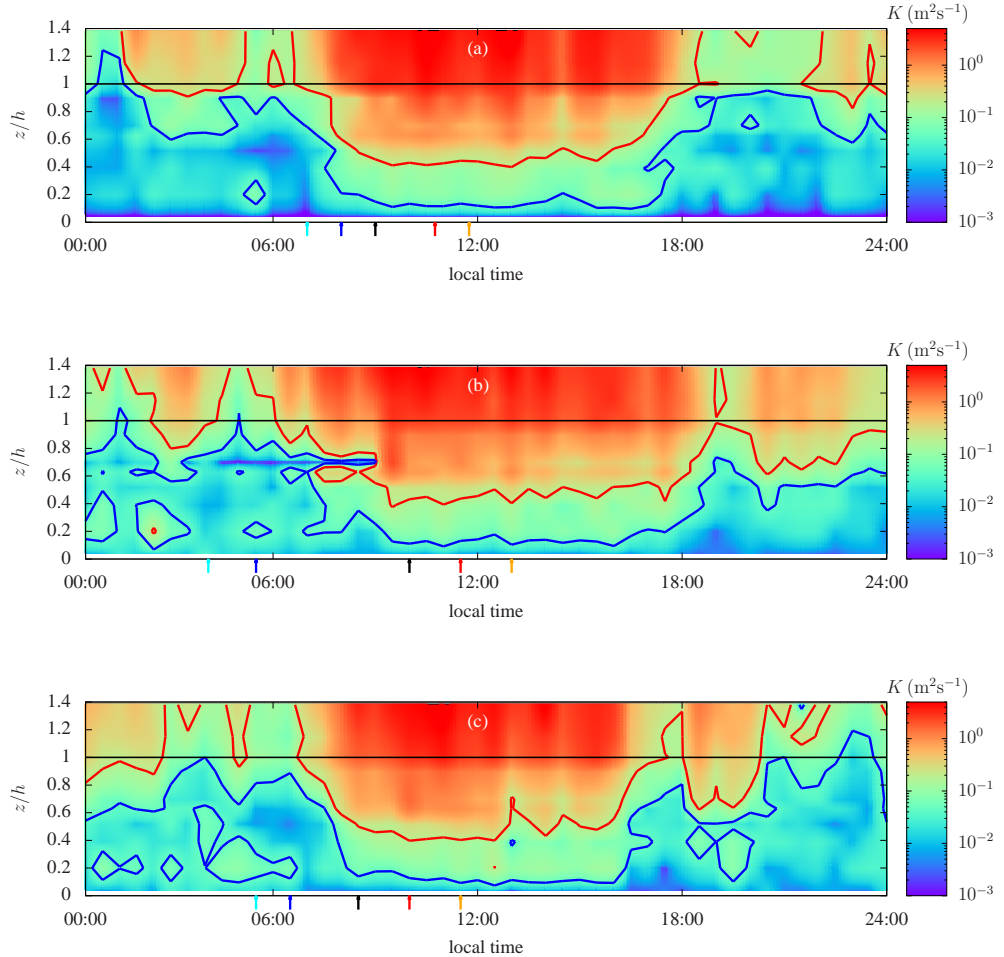


Figure 2.3. Eddy diffusivity (K) as a function of local time and height. (a) October 30, 2014, (b) December 3, 2014 and (c) December 4, 2014. Blue and red lines indicate the limits $K = 0.5K_e$ and $K = 2K_e$, respectively. The arrows at the bottom indicate the times of the profiles presented in Figure 2.1.

Santos et al., 2016).

A general average picture of the diurnal cycle of turbulent mixing within the Amazon forest is presented in Figure 2.4, where $\langle K \rangle$ is the yearly averaged eddy diffusivity. Between 6:30 and 18:00 hours, a period starting 30 minutes after sunrise and ending at sunset, the upper half of the canopy was in the well-mixed regime while most of the lower half was still partially mixed. Conversely, during nighttime, the uppermost 40% of the canopy (above $z/h \approx 0.6$) was in the partially mixed regime while the rest was poorly mixed. An interesting region of slightly enhanced

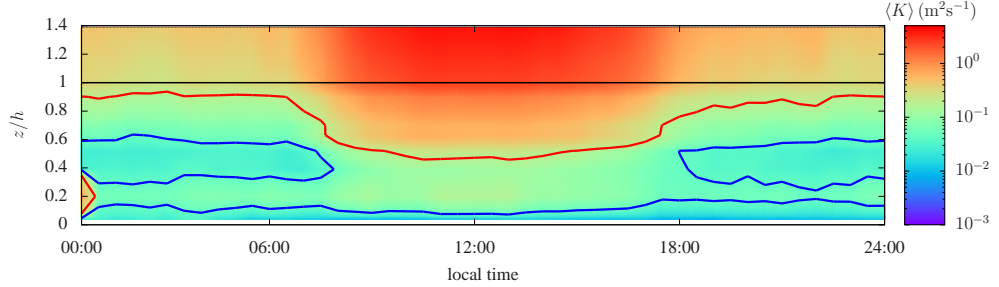


Figure 2.4. Yearly averaged eddy diffusivity ($\langle K \rangle$). Blue and red lines indicate the limits $\langle K \rangle = 0.5K_e$ and $\langle K \rangle = 2K_e$, respectively.

mixing was present in the lower canopy during the night (around $z/h \approx 0.2$). This region was coincident with the location where a secondary peak in the mean velocity forms at night (e.g., see Santos et al., 2016). Even though this increased mixing likely diluted trace gases locally, it was decoupled from the top of the canopy and therefore unlikely to cause significant exchanges of trace gases with the air above the forest. Based on the average diurnal cycle alone, one can expect that on average, trace gases emitted by the forest may accumulate inside the canopy during nighttime. Gases are thereafter transported out of the forest, though not as a spatially uniform diffusive front (assumed here) but as spatially intermittent plumes (not considered here). Also, on average, gases present above the canopy undergo significant levels of mixing within the entire vertical extent of the forest during the period between sunrise and sunset. The day-to-day variability in eddy diffusivity was quantified via σ_K (the standard deviation around the yearly averaged eddy diffusivity; not shown). Values of $\sigma_K/\langle K \rangle$ tend to be larger than unity in the lower canopy (below $z/h \leq 0.4$) during the entire diurnal cycle. In the upper canopy, the values are much smaller during daytime ($\sigma_K/\langle K \rangle < 0.5$) but it is still slightly larger than unity during most of the night.

A better measure of the variability in the data set can be gained from Figure 2.5, which shows the fraction of the time spent in each of the three mixing regimes as a function of height. Results were separated into three periods: nighttime (18:00-24:00 and 0:00-6:30 hours), sunrise and sunset transitions (6:30-9:00 and 16:00-18:00 hours), and daytime (9:00-16:00 hours). Daytime periods exhibited little variability, and the average results shown in Figure 2.4 were dominant throughout the year. Conversely, nighttime periods displayed more variability, specially in

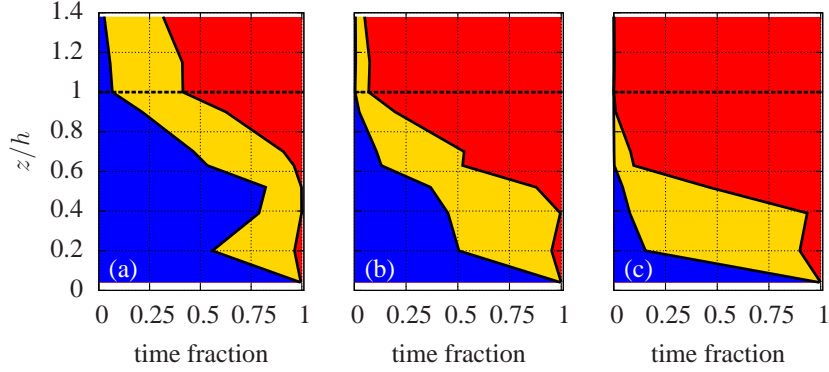


Figure 2.5. Time fraction spent in the poorly mixed (blue), partially mixed (yellow) and well-mixed (red) regimes as a function of height for (a) nighttime, (b) sunrise and sunset transitions, and (c) daytime. See text for more details.

the upper canopy layers where most of the time was evenly distributed between partially mixed and poorly mixed. This variability was likely associated with the distinct behaviors of calm nights with weak turbulence, fully turbulent nights, and intermediate cases in which intermittent turbulence was present at the site (Santos et al., 2016). A summary of these results is also presented in Table 2.4.

2.3.2 Timescales for turbulent mixing

The proposed model (Equation (2.9)) can now be used to translate eddy diffusivity estimates into timescales associated with a chosen level of mixing. Here, τ_{mix} is defined as the time required to reach $\overline{[\text{O}_3]}/[\text{O}_3]_h = 0.86$. This timescale illustrates the significance of the large space-time differences in eddy diffusivity observed within the Amazon forest as the day progresses. As a first example, consider two hypothetical situations in which K is constant within the entire depth of the canopy and equal to the two limits used to separate the three mixing regimes defined in the previous section (see Table 2.3). The time evolution of normalized ozone mixing ratios inside the forest obtained from Equation (2.9) is shown for these two cases in Figure 2.6. After two hours, the entire depth of the canopy is well mixed for the larger $K = 2K_e$, while the well-mixed region only encompasses the uppermost 15% of the canopy for the lower $K = 0.5K_e$. Thus, a rough interpretation of the mixing limits inferred from Figure 2.2 in terms of how much mixing can be accomplished in 2 hours can be established. For the poorly mixed regime, only the uppermost 15%

Table 2.4. Summary of occurrence of the three mixing regimes (numbers represent fraction of time in poorly mixed; partially mixed; well-mixed regimes).

Canopy region	Heights	Nighttime periods	Transition periods	Daytime period
Upper canopy	0:00-6:30	6:30-9:00	16:00-18:00	9:00-16:00
	18:00-24:00	16:00-18:00		
Lower canopy	$z/h > 0.5$	0.40; 0.43; 0.17	0.09; 0.33; 0.58	0.00; 0.06; 0.94
	$z/h < 0.5$	0.79; 0.20; 0.01	0.58; 0.38; 0.04	0.32; 0.50; 0.18

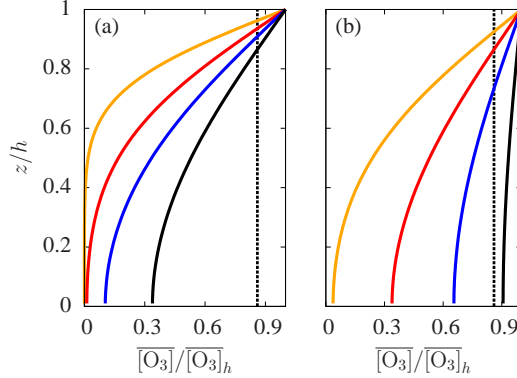


Figure 2.6. Time evolution of ozone mixing ratio inside the forest for the two values of eddy diffusivity used to separate the mixing regimes. (a) $K = 0.045 \text{ m}^2 \text{s}^{-1}$ and (b) $K = 0.18 \text{ m}^2 \text{s}^{-1}$. Yellow, red, blue and black lines indicate mixing times equal to 10, 30, 60, and 120 min, respectively. The vertical dashed line represents the limit for well-mixed regime $\overline{[O_3]}/\overline{[O_3]}_h = 0.86$.

of the canopy is mixed within 2 hours, while for the well-mixed regime the entire canopy becomes mixed within 2 hours or less. Other cases fall into the partially mixed regime.

Turbulent mixing timescales obtained from the yearly averaged diurnal patterns of eddy diffusivity are shown in Figure 2.7 for the two equivalent eddy diffusivities. These timescales can be interpreted as lower and upper bounds on the “response timescale” associated with turbulent mixing. It is the time it would take for a given level within the forest to respond to changes in ozone concentration above the forest. Between 10:00 and 13:00 hours, most of the forest responded to such ozone concentration changes, on average, in less than 60 minutes. This may be surprisingly fast given how stagnant air flow may be inside the forest on an average day. In contrast to daytime conditions, during most of the night only the upper 20% of the forest responded within an hour or so as a consequence of the weak turbulence associated with the nighttime calm conditions.

The case of December 3, 2014 is shown in Figure 2.8, as an example of the possible variability of individual days instead of an ensemble averaged day (where ensemble averaging is applied across the hour of the day). The nighttime evolution for this day presented patterns of effective atmospheric mixing. During nighttime, mixing was slow with timescales much longer than 2 hours throughout most of the forest depth and most of the time. However, this pattern was interrupted by events

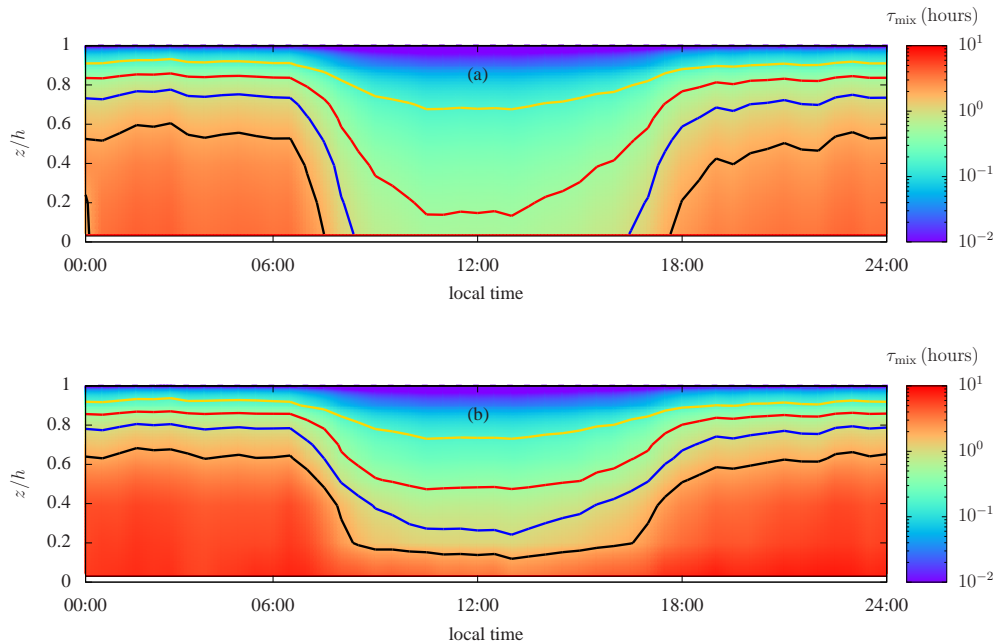


Figure 2.7. Turbulent mixing timescale (τ_{mix}) as a function of local time and height obtained from the yearly averaged eddy diffusivity $\langle K \rangle$ using (a) $K_{\text{eq},1}$ and (b) $K_{\text{eq},2}$, representing lower and upper bounds on the expected timescales, respectively. Yellow, red, blue and black lines indicate mixing times equal to 10, 30, 60, and 120 min, respectively.

of enhanced turbulence that lasted one or two hours (during this specific night) in which significant mixing can occur (because a significant portion of the canopy has a mixing timescale shorter than the duration of the events). These events, which are associated with bursts of intermittent turbulence, have the capability of mixing ozone into the forest and, more importantly, promoting the transport of gases emitted by the forest during nighttime that would, otherwise, be accumulating until morning hours.

Average profiles of turbulent mixing timescales for nighttime and daytime are shown in Figure 2.9 (sunrise and sunset transitions fall in between and are not shown). The entire vertical extent of the forest is mixed in 1 hour or less during daytime, with the exception of the lowermost levels where the uncertainty in the estimates is quite large. During nighttime, between 3.5 and 6.5 hours are required to accomplish the same level of mixing. These values seem to be in reasonable agreement with the 3.4 hours estimated by Trumbore et al. (1990) and within the large range of 2 to 10 hours suggested by Martens et al. (2004), both based on ^{222}Rn

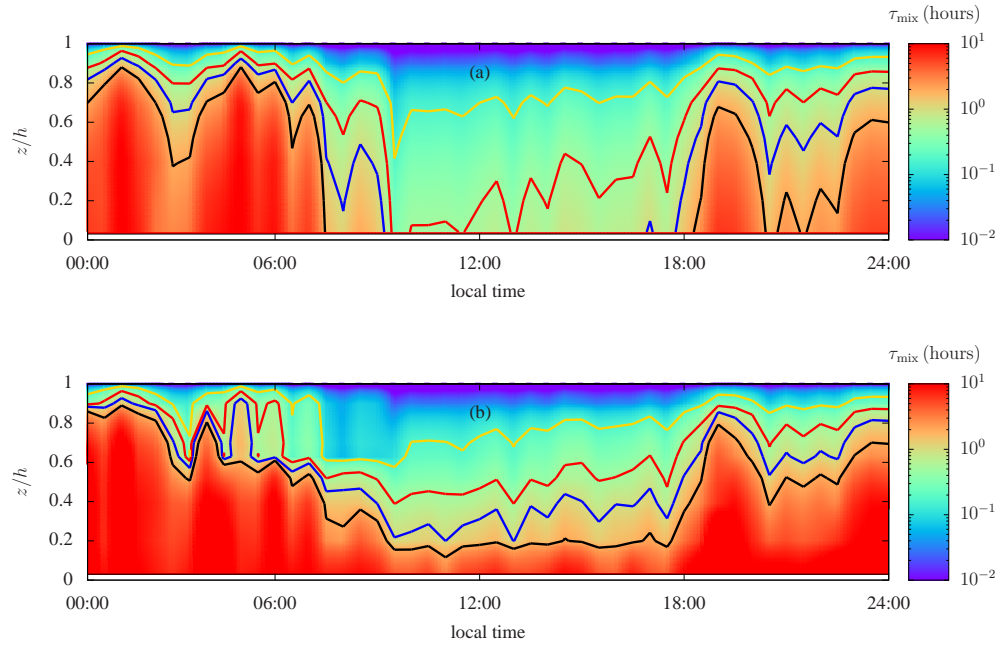


Figure 2.8. Same as Figure 2.7 but for December 3 2014.

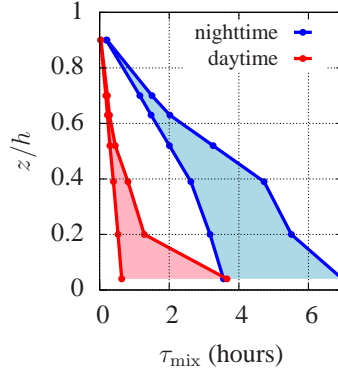


Figure 2.9. Average turbulent mixing timescale (τ_{mix}) as a function of height obtained from the yearly averaged eddy diffusivity $\langle K \rangle$ for nighttime (blue) and daytime (red). Periods are divided as in Figure 2.5. The bounds are estimates of timescales using $K_{\text{eq},1}$ and $K_{\text{eq},2}$, while the true timescale is expected to fall somewhere in the filled area in between.

measurements. Note that at $z/h \approx 0.375$, $\tau_{\text{mix}} > 2.5$ hours, which is significantly larger than the 40-minute estimate of Simon et al. (2005), despite the fact that the data set used here also presents cases of convective mixing inside the canopy produced by nighttime radiative cooling in the upper canopy (Santos et al., 2016).

2.3.3 Timescales for ozone sink within the forest

The bulk deposition velocities at the canopy top obtained from the ozone mass balance were compared to those reported by Fan et al. (1990) for the Ducke Forest and by Rummel et al. (2007) for a site in the Reserva Biológica Jarú (90 km north of the city of Ji-Paraná, approximately 900 km southwest of ZF2 site). The values reported by Fan et al. (1990) and Rummel et al. (2007) were obtained using eddy covariance estimates of the ozone flux and are more reliable than those obtained from the ozone budget model employed here. Comparisons between different experiments must take into account the time of the year, as the lower specific humidity in the dry season leads to a reduction in stomatal activity and ozone deposition in the Amazon (Rummel et al., 2007). Data from the other experiments correspond to average values for wet or dry seasons, and our comparison here hinges on the assumption that variations in atmospheric and surface conditions are dominated by the seasonal cycle between wet and dry seasons. The ozone profiles presented here were obtained at the beginning of the wet season (October–December), whereas the data presented by Fan et al. (1990) correspond to the end of the wet season (April–May, which is the peak of rainfall near Manaus). Therefore, it is reasonable that the data from the GoAmazon field campaign fall between the wet period of Fan et al. (1990) and Rummel et al. (2007) and the dry period of Rummel et al. (2007). The reasonable agreement with deposition velocity inferred from eddy covariance measurements (Figure 2.10a) serves as a partial verification of the fidelity of the ozone budget model outcome.

Values of the dimensionless number $N_{GD} = V_S/(3u_*)$ are never larger than 0.06, satisfying the criteria $N_{GD} \ll 1$ (see Figure 2.10b). This result lends some support to the validity of eddy diffusivity model for estimating ozone fluxes. At first, it seems to be at odds with the general idea that eddy diffusivity models fail in the canopy region. Differently from heat or CO₂, in the present case ozone has no net sources inside the canopy and the timescales associated with the sink processes are in general quite large. This combination leads to monotonic and fairly smooth ozone profiles within the canopy, being more amenable to the application of eddy diffusivity models.

The daytime and nighttime average values of ozone deposition velocity are summarized in Table 2.5. These results suggest that the chemical sink is responsible

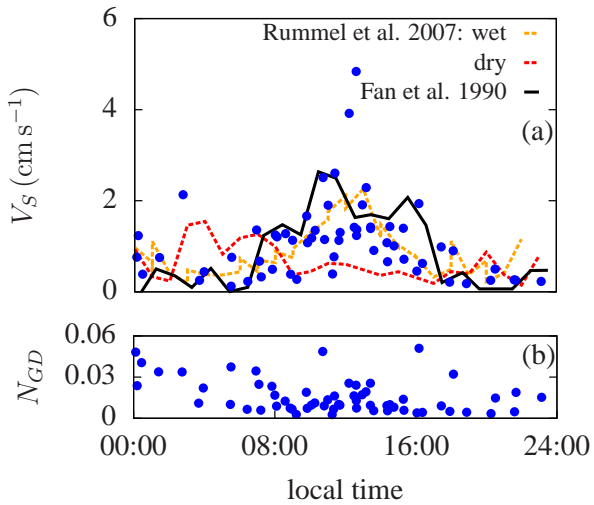


Figure 2.10. (a) Deposition velocity (V_S) as a function of time. Black line corresponds to results presented by Fitzjarrald et al. (1990) and Fan et al. (1990) for a similar site in the Amazon forest, dashed lines correspond to results presented by Rummel et al. (2007) for wet (yellow) and dry (red) in the Amazon forest. (b) Values of the criteria $N_{GD} = V_S/(3u_*)$ for applicability of the eddy diffusivity model.

for about 10% of the total sink into the canopy during the day, and 39% during the night. As expected from the dominant role of sesquiterpenes in the chemical sink, these values of V_{chem} are not impacted by concentrations of monoterpene and isoprene (deposition velocities due to reactions with isoprene and monoterpenes are between 10 and 300 times smaller than those associated with sesquiterpene oxidation). The larger chemical deposition during nighttime is caused by the inverse relationship between ambient mixing ratios of ozone and sesquiterpene (Jardine et al., 2011). Due to smaller nighttime O_3 mixing ratios, nighttime ozone fluxes due to sesquiterpene oxidation may still be smaller than daytime fluxes. The bulk timescale at canopy top resulting from chemical sink is equal to $\tau_{\text{chem}} = 6.1$ hours for daytime and $\tau_{\text{chem}} = 4.4$ hours for nighttime. For the nonchemical loss, values of $V_{\text{su,dd}}$ were estimated by inserting these estimates of V_S and V_{chem} into Equation (2.14), which combined with Equation (2.15) yields a rough estimate of the bulk timescale associated with nonchemical processes of $\tau_{\text{su,dd}} = 0.71$ hours for daytime and $\tau_{\text{su,dd}} = 2.8$ hours for nighttime.

Perhaps at this point, a caveat in this analysis must be discussed. The definition of chemical lifetimes as a characterization of the canopy chemical environment must

Table 2.5. Values of bulk sink deposition velocity V_S , chemical deposition velocity V_{chem} and nonchemical deposition velocity $V_{\text{su,dd}}$.

	V_S (cm s $^{-1}$)	V_{chem} (cm s $^{-1}$)	$V_{\text{su,dd}}$ (cm s $^{-1}$)	V_{chem}/V_S	$V_{\text{su,dd}}/V_S$
daytime	1.53	0.16	1.37	0.10	0.90
nighttime	0.57	0.22	0.35	0.39	0.61

be based on the true ambient concentration of the reactive species. However, the mixing ratios of isoprene, monoterpenes, and sesquiterpenes obtained from the measurements and used in the estimates of V_{chem} (and indirectly in the estimates of $\tau_{\text{su,dd}}$) already include effects of ozone oxidation. Ideally, concentration of these gases before oxidation should be used, as the oxidation can be quite significant for the most reactive sesquiterpenes (Stroud et al., 2005). The concentrations of BVOCs used in the calculation of the V_{chem} likely represent the lower bound values, and therefore the ozone chemical sink could be greater than the ones estimated here and consequently the values of $\tau_{\text{su,dd}}$ could be smaller.

The three timescales representing turbulent mixing, chemical reaction and nonchemical loss are shown in Figure 2.11 for daytime and nighttime conditions. During the day turbulent mixing is clearly much faster than chemical reactions for the entire canopy, indicating that the well-mixed assumption is a good representation for modeling chemical reactions of ozone inside the forest. During the night, turbulent mixing timescales remain much smaller than the chemistry in the upper canopy (where the eddy diffusivity remains large). However, deeper in the canopy, turbulence becomes weak and the timescales of turbulence and chemistry become similar (i.e. the Damköhler number is of order unity), suggesting a strong link between physical and chemical processes.

Some care is needed in comparing the nonchemical removal timescale to chemistry and turbulent mixing, as this is a bulk timescale for the entire canopy and it is not vertically resolved as the others. Nevertheless, as it represents an integration through the canopy height, this bulk timescale can be seen as an average value of the profile observed in the forest. In this case, the nonchemical loss timescale can have values comparable to the turbulence timescale during both daytime and nighttime periods, whereas it is likely much larger than the chemical timescale during the day.

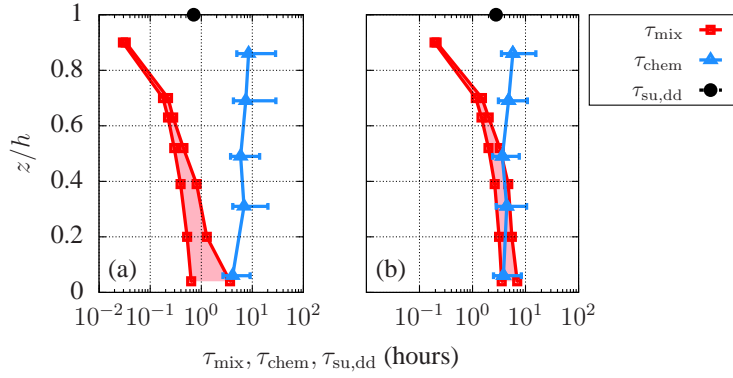


Figure 2.11. Timescales for turbulent mixing (τ_{mix}), chemical reaction with BVOCs (τ_{chem}), and nonchemical removal processes ($\tau_{\text{su,dd}}$) for (a) daytime and (b) nighttime conditions.

2.4 Conclusions

The analysis of profiles of ozone mixing ratio within and above the Amazon forest suggested a dependency on local eddy diffusivity, indicating an impact of turbulent mixing on the evolution of ozone concentration. This observed relationship was used to establish threshold values in eddy diffusivity that define regimes of poorly, partially, and well-mixed turbulence conditions. Based on a 10-month period for which turbulence data is available, it was observed that the upper half of the forest is well mixed 94% of the time during the day and it is either partially or poorly mixed (43% and 40% of the time, respectively) during the night. For the lower half of the forest, prevailing conditions are partially mixed during the day (50% of the time with well mixed conditions occurring 18% of the time) and poorly mixed (79% of the time) during the night. This scenario describes the average conditions in which chemical and physical processes happen in the Amazon.

A simplified model was developed to convert the eddy diffusivity data into a meaningful turbulent mixing timescale as a function of canopy depth and time-of-day. The values of turbulent mixing timescales can assist in interpreting the potential impact of turbulence on other processes happening in the forest environment. In the case of the Amazon forest, on average, the entire vertical extent of the forest responds to changes above the canopy in less than 60 minutes during the hours around local noon. During nighttime, only the uppermost 20% of the forest responds to changes within an hour or so and 3.5 to 6.5 hours are needed for the entire

forest to respond to changes above the canopy. At a given height inside the canopy, τ_{mix} presented not only a significant diurnal cycle, but also great variability among individual nights, depending on the episodic nature of intermittent turbulence that exerts a dominant role in nighttime mixing. Results also showed that in the morning transition the change in turbulent mixing can be quite fast, creating a transient scenario that limits the use of equilibrium or steady-state models and well-mixed assumptions when representing chemical and physical processes happening in the forest environment during the first hours of the day. The mixing timescales estimated here can be used as a reference for comparison with other processes happening within the Amazon rainforest. In addition, the new methodology applied here can be a useful tool for the estimation of mixing timescales in other types of canopy.

Ozone sinks inside the canopy were estimated using a one-dimensional ozone mass balance and typical values of BVOCs observed in the Amazon forest. While dry deposition and stomatal uptake dominate the daytime ozone sink, the oxidation of sesquiterpenes is responsible for some 40% of the nighttime ozone loss, highlighting the importance of within-canopy chemical reactions. Results also showed that turbulence is much faster than ozone chemistry during daytime, whereas chemistry and turbulence are comparably slow in the lower half of the canopy during nighttime. Timescales of nonchemical removal processes are comparable to mixing timescales, indicating that stomatal uptake and dry deposition of ozone is possibly dependent on the efficiency of turbulence on transporting ozone to the canopy environment. These ozone results exemplify the important role of turbulent mixing in the air chemistry of a forest.

2.A A simplified relation between Eulerian and Lagrangian timescales

A simplified relation between Eulerian (T_E) and Lagrangian (T_L) timescales can be obtained following the approach proposed by Poggi et al. (2008). Here, the Eulerian and Lagrangian second-order structure functions of vertical velocity ($D_{33}^E(r)$ and $D_{33}^L(\tau)$, respectively) are used to link these two timescales. At the cross-over from production to inertial, it is assumed that the largest scales populating the inertial

subrange follow their respective Kolmogorov scaling (e.g., see Monin and Yaglom, 2013)

$$D_{33}^E(r) = C_2 \epsilon^{2/3} r^{2/3}, \quad (2.18)$$

$$D_{33}^L(\tau) = C_0 \epsilon \tau, \quad (2.19)$$

where r and τ are space and time lags, ϵ is the mean turbulent kinetic energy (TKE) dissipation rate and C_2 and C_0 are universal constants. For simplicity, it is also assumed that both formulations already yield most of the vertical velocity variance at the cross-over point from production to inertial (indicated by R_E and T_L) so that

$$D_{33}^E(R_E) = D_{33}^L(T_L) = 2\sigma_w^2. \quad (2.20)$$

If Taylor's frozen turbulence hypothesis is used to define $R_E = \bar{u}T_E$, then we can rewrite (2.20) as

$$T_L = \frac{C_2}{C_0} \epsilon^{-1/3} (\bar{u}T_E)^{2/3}. \quad (2.21)$$

However, using (2.20) the rate of TKE dissipation can be expressed in terms of the vertical velocity variance $\epsilon = 2\sigma_w^2/(C_L T_L)$, which yields the desired relation between the aforementioned timescales

$$T_L = \frac{C_2^{3/2}}{\sqrt{2}C_0} \frac{\bar{u}}{\sigma_w} T_E. \quad (2.22)$$

Finally, the constants C_2 and C_0 must be specified. The constant C_2 can be related to the Kolmogorov constant for the energy spectrum $C_k \approx 0.53$ (Sreenivasan, 1995) via $C_2 \approx (4/3) \times 4 \times C_k$, where the factor $4/3$ arises from the assumption of isotropy in the inertial subrange and the factor 4 is a conversion between constants in the energy spectrum and the second-order structure function (Pope, 2000). As for C_0 , a wide range of estimates is available in the literature (e.g., see values listed by Lien and D'Asaro, 2002; Poggi et al., 2008). Recent high resolution Lagrangian experiments performed by Ouellette et al. (2006) in anisotropic turbulence suggest that the value is impacted by anisotropy and it varies between 5.0 and 6.2 for their

largest Reynolds numbers. We adopt an intermediate value of $C_0 \approx 5.5$, which is in agreement with the classic value of Pope and Chen (1990) and the experimental value for model canopies reported by Poggi and Katul (2006).

2.B Equivalent eddy diffusivity

Consider a system with two homogeneous layers with thicknesses $z_1 = z_2 = h/2$ and eddy diffusivities K_1 and K_2 . To make the argument clearer, we consider an extreme case in which $K_2 \gg K_1$ with $K_2 \sim 1 \text{ m}^2 \text{s}^{-1}$ and $K_1 \ll 1 \text{ m}^2 \text{s}^{-1}$ (note in Figure 2.4 that typical values of K are of order $1 \text{ m}^2 \text{s}^{-1}$ at the top of canopy and $10^{-2} \text{ m}^2 \text{s}^{-1}$ deeper into the canopy). As in the ozone transport into the canopy, assume that the scalar of interest must first travel through the layer with higher diffusivity to reach the layer with lower diffusivity. Given that $K_2 \gg K_1$, transport across layer 2 occurs efficiently and the time for transport across the entire layer is approximately the diffusion time across layer 1. We seek to replace K_1 and K_2 by an equivalent eddy diffusivity K_{eq} that can be used uniformly through the entire depth h . An arithmetic average estimate yields $K_{\text{eq}} = (K_1 + K_2)/2 \approx K_2/2$. This is equivalent to $K_{\text{eq},1}$ given by Equation (2.6). Transport across layer 2 will still be very fast, but the transport time across layer 1 will be strongly underestimated. Therefore, using the average K will yield a lower bound on the diffusion time across the entire layer. Alternatively, one can use an electrical circuit analogy and consider K_1 and K_2 as conductivities across each layer. Thus, the resistances across the layers are $h/(2K_1)$ and $h/(2K_2)$. Given that the two pathways are in series (in the sense that the scalar must first travel across layer 2 and then across layer 1), the equivalent resistance is $h/K_{\text{eq}} = h/(2K_1) + h/(2K_2)$ and yields $K_{\text{eq}} = 2K_1K_2/(K_1 + K_2) \approx 2K_1$. This model is equivalent to $K_{\text{eq},2}$ given by Equation (2.7). This model will provide a reasonable estimate of transport time across layer 1, but it will overestimate the transport time across layer 2, yielding an upper bound on the diffusion time across the entire layer. Finally, a geometric mean between K_1 and K_2 would yield an intermediate transport time and it could be written in a general form using the product integral, but it is not clear that the results would be an upper or lower bound on the transport time.

2.C Determination of the deposition velocity

A partitioning of the deposition velocity into chemical and nonchemical removal processes can be obtained using the ozone mass balance. The storage term ($\partial[\overline{O_3}]/\partial t$) was always the smallest term in the mean ozone budget, being more than one order of magnitude smaller than the other terms during the day. This result is similar to the ozone budget estimated by Jacob and Wofsy (1990) for the Ducke Forest (a different site less than 60 km away from the ZF2), and it implies an approximate equilibrium between the sink term and the flux divergence. Therefore, the reduction in the flux must be approximately balanced by chemical loss, stomatal uptake, and dry deposition. Neglecting the storage term and the ozone deposition to the ground surface ($\overline{w'[\overline{O_3}']}_0 \approx 0$), integration of Equation (2.4) over the entire canopy height yields

$$\overline{w'[\overline{O_3}']}_h = \int_0^h S(\xi) d\xi. \quad (2.23)$$

At this point, additional information about the nature of $S(z)$ is required. Following Launiainen et al. (2013), the stomatal uptake (D_{su}) and dry deposition (D_{dd}) can be modeled using

$$D_{su}(z) = -a(z)g_{eff}(z)\overline{[O_3]}(z), \quad (2.24)$$

$$D_{dd}(z) = -a(z)g_{cut*}(z)\overline{[O_3]}(z), \quad (2.25)$$

where $a(z)$ is the leaf area density and $g_{eff}(z)$ and $g_{cut*}(z)$ are conductances associated with stomatal uptake and dry deposition, respectively (see Launiainen et al., 2013, for more details).

Thus, the overall bulk sink term can be expressed as

$$S(z) = -a(z)g(z)\overline{[O_3]}(z) - k\overline{[BVOC]}(z)\overline{[O_3]}(z), \quad (2.26)$$

with $g(z) = g_{eff}(z) + g_{cut*}(z)$. It is of interest to obtain approximate expressions for the two components of $S(z)$ in terms of the ozone concentration at the top of the canopy so that the result can be recast in terms of the deposition velocity. We choose to re-write (2.26) as

$$S(z) \approx -a(z)\bar{g}\overline{[O_3]}_h - k\overline{[BVOC]}(z)\overline{[O_3]}_h \quad (2.27)$$

where \bar{g} is an average conductance. Inserting (2.27) into (2.23) yields

$$\overline{w'[O_3]'}_h \approx -\bar{g}\overline{[O_3]}_h \text{LAI} - k\overline{[BVOC]}_{avg}\overline{[O_3]}_h h. \quad (2.28)$$

Here, $\overline{[BVOC]}_{avg}$ is the mean mixing ratio of BVOCs averaged within the vertical extent of the canopy and by definition $\text{LAI} = \int_0^h a(\xi)d\xi$. Dividing by $-\overline{[O_3]}_h$ allows for a partitioning of the deposition velocity into chemical and nonchemical sinks given by Equation (2.14).

2.D Criteria for validity of eddy diffusivity model

We consider the turbulent flux budget equation for a generic scalar C that can be derived using conventional approaches. Assuming steady state, planar homogeneous flow with no subsidence, and negligible molecular terms (i.e., large Reynolds number), the mean scalar flux budget equation in the vertical direction is given as

$$\frac{\partial \overline{w'C'}}{\partial t} = 0 = -\overline{w'w'}\frac{\partial \overline{C}}{\partial z} - \frac{\partial \overline{w'w'C'}}{\partial z} + \frac{1}{\bar{\rho}}\overline{C'}\frac{\partial \overline{P'}}{\partial z} + \frac{g}{\bar{\theta}}\overline{\theta'C'}. \quad (2.29)$$

On the right hand side, the first term is the production of turbulent flux due to the interaction between turbulence and the mean concentration gradient; the second represents a triple-moment term interpreted as a transport of the flux by turbulence; the third is the pressure-scalar interaction term (i.e., destruction term), which acts to de-correlate w' from C' ; and the fourth is the buoyancy term (can be a source or sink) induced by the covariance between temperature and scalar concentration turbulent fluctuations. To proceed further, the destruction term for the scalar-flux is modeled similarly to the destruction term for momentum flux and is given as

$$\frac{1}{\bar{\rho}}\overline{C'}\frac{\partial \overline{P'}}{\partial z} = -C_R \frac{\overline{w'C'}}{\tau} + C_1 \sigma_w^2 \frac{\partial \overline{C}}{\partial z}, \quad (2.30)$$

where C_R is the Rotta constant, $C_1 = 3/5$ (derived from Rapid Distortion Theory), and $\tau(z)$ is a relaxation timescale. Combining the above two equations, the scalar

flux can be expressed as

$$\overline{w' C'} = -\frac{\tau}{C_R} \left[(1 - C_1) \overline{w' w'} \frac{\partial \bar{C}}{\partial z} + \frac{\partial \overline{w' w' C'}}{\partial z} - \frac{g}{\theta} \overline{\theta' C'} \right]. \quad (2.31)$$

Formulated in this manner, the necessary conditions leading to the validity of the eddy diffusivity approach become evident. When the sum of the flux transport term and buoyancy terms are small compared to the production, the eddy diffusivity model is recovered with $K = (\frac{1-C_1}{C_R})\tau\sigma_w^2$. Therefore, it is possible to derive a dimensionless number N_{GD} to represent the modeled expected deviation from the eddy diffusivity model, given by

$$N_{GD} = \left| \frac{\frac{\partial \overline{w' w' C'}}{\partial z} - \frac{g}{\theta} \overline{\theta' C'}}{(1 - C_1) \overline{w' w'} \frac{\partial \bar{C}}{\partial z}} \right|. \quad (2.32)$$

The use of an eddy diffusivity closure is acceptable when $N_{GD} \ll 1$. However, determining N_{GD} from data is difficult as it requires fast-response sensors to measure $\overline{\theta' C'}$ and multi-level flux measurements to determine $\overline{w' w' C'}$. For operational purposes, these measurements are rarely available in canopy studies necessitating additional approximations. For the purposes of evaluating N_{GD} , the buoyancy term is ignored and the flux transport term is modeled as

$$\overline{w' w' C'} = -C_2 \tau \sigma_w^2 \frac{\partial \overline{w' C'}}{\partial z}, \quad (2.33)$$

where C_2 is a closure constant. Hence, when combined with the mass balance equation (2.4), $\overline{w' w' C'}$ scales as $\tau \sigma_w^2 S(z)$ (this is analogous to the near-field effect arising in Lagrangian models). To a first approximation, N_{GD} scales as

$$N_{GD} = \frac{C_2}{1 - C_1} \left| \frac{\frac{\partial}{\partial z} [\tau \sigma_w^2 S(z)]}{\overline{w' w'} \frac{\partial \bar{C}}{\partial z}} \right| \sim \frac{\tau S_{avg}}{\Delta \bar{C}}. \quad (2.34)$$

Here, $\Delta \bar{C}$ may be estimated from the overall change in mean concentration across the entire canopy depth and τ may be estimated from T_E or $h/(3u_*)$. Assuming that S_{avg} scales as $\overline{w' C'} h/h$ and taking $\bar{C}(0) = 0$ leads to Equation (2.16).

Chapter 3 |

A one-dimensional stochastic model of turbulence within and above plant canopies

3.1 Introduction

The development of reduced-order models to represent turbulence and transport of scalars in the canopy roughness sublayer has been the subject of much interest for nearly 40 years. The interaction between the turbulent flow and canopy elements leads to a complex flow field that presents a challenge to simple parameterizations. Even if the problem is significantly simplified to a horizontally homogeneous distribution of canopy elements, the resulting flow field is still too complex to be modeled via simple mixing-length eddy-viscosity approaches (e.g., see review by Finnigan, 2000). Therefore, the first successful approaches to model turbulence in the roughness sublayer were based on second-order closure of the Reynolds-Averaged Navier-Stokes (RANS) equations (Wilson and Shaw, 1977; Wilson, 1988; Massman and Weil, 1999). However, in this approach a number of closure assumptions are required and the final model equations usually involve a large number of constants that need to be determined. Furthermore, the number of equations increases fast if the transport of many scalar fields (e.g. temperature, water vapor, carbon dioxide, etc.) are to be included (Juang et al., 2008). With the exception of the analytical model developed by Massman and Weil (1999), the set of closed RANS equations must be discretized and a numerical solution is then obtained.

In many applications, the transport of scalars inside canopies is simulated using

a Lagrangian stochastic methodology based on the Langevin equation (e.g., see Thomson, 1987; Wilson and Sawford, 1996). However, this modeling approach is incomplete, as it requires specification of the profiles of turbulence statistics. These profiles are typically obtained from experiments (e.g. Reynolds, 1998; Cassiani et al., 2007) or from high-order closure RANS models described above (e.g. Katul et al., 2011; Gleicher et al., 2014).

In the design of reduced-order models, a minimum representation of turbulence in the roughness sublayer must include the effects of surface layer eddies and the effects of eddies produced by the shear instability caused by the inflected mean velocity profile. Therefore, a reasonable representation of shear production of turbulent kinetic energy (TKE) is critical. In addition, the model must include a description of the vertical structure of the sources and sinks of momentum and scalars within the vegetation. In this work we investigate the suitability of the One-Dimensional Turbulence (ODT) model (Kerstein, 1999) as a reduced-order model of canopy turbulence embedded in the atmospheric boundary layer (ABL). The ODT model was designed to provide a stochastic representation of three-dimensional turbulence along a one-dimensional line. Therefore, in the context of ABL simulations, ODT can be viewed as a single-column model with a stochastic representation of turbulence. In the ODT framework, the unsteady, one-dimensional diffusion equations of momentum, temperature and other passive scalars are solved numerically on a discrete grid, and the turbulent transport is represented by stochastic non-local eddy events described by a mapping. The ODT model was formulated by Kerstein (1999), who also showed that the model produces flow statistics in overall agreement with observations and theoretical predictions for homogeneous turbulence and wall-bounded flows with and without buoyancy. The modeling approach was then significantly extended to include the evolution of the entire velocity vector (as opposed to one single velocity component) by (Kerstein et al., 2001). The model has been applied to a wide range of flows including free-shear laboratory-scale flows (Kerstein et al., 2001), turbulent flames (Echekki et al., 2001), the stable ABL (Kerstein and Wunsch, 2006), and particle-laden flows (Schmidt et al., 2009). In addition, ODT can be modified to simulate spatially evolving flows such as jets and wakes by a simple conversion of time into streamwise distance using an appropriate advection velocity (Echekki et al., 2001).

Although the ODT model is typically used to represent all the scales of the

flow down to the Kolmogorov scales, its application to simulate the entire vertical extent of the ABL leads to a fairly high computational cost defeating the purpose of a reduced-order modeling approach. Therefore, it is convenient to introduce a filter separating resolved and sub-grid scales as usually done in the context of Large-Eddy Simulation (LES). In fact, the stable ABL simulations of the GABLS case (Cuxart et al., 2006) performed by Kerstein and Wunsch (2006) adopt an eddy-viscosity parameterization. However, their eddy-viscosity parameterization was found to produce unsatisfactory results when compared to other GABLS single-column model simulations and to high-resolution ODT simulations. Thus, the applicability of ODT as a model for ABL flows hinges on the development of a sub-grid scale (SGS) model capable of representing the effects of unresolved scales on the ODT-modeled flow dynamics. To this end, a one-dimensional adaptation of the classic Smagorinsky eddy viscosity model used in LES (Deardorff, 1970) is developed and tested here.

Even though the focus of this work is on the applicability of the filtered ODT model to simulating canopy flows, a secondary goal is to assess the potential of ODT as a column model for ABL flows in general. Thus, the new SGS model is first evaluated by assessing simulation results for neutral, unstable and stable ABLs with the surface roughness being parameterized by a roughness length scale. These ABL tests are followed by simulations that explicitly resolve the presence of plant canopies, whose domain is the entire neutral ABL (from the ground below the canopy) plus a layer of the free troposphere above the entrainment zone. The canopy-resolving simulations were designed to match three observational data sets from the literature. The first two cases were designed to reproduce field experiments in a walnut orchard (Patton et al., 2010) and a maize field (Gleicher et al., 2014). The third test case is for a model canopy wind-tunnel experiment with an elevated line source of a passive scalar (Raupach et al., 1986; Coppin et al., 1986).

The basic details of the ODT model, including the modifications introduced to represent the canopy and the new SGS model, are presented in Section 3.2. A brief description of the experimental data sets used and the model setup are given in Section 3.3 and simulation results are presented in Section 3.4. Conclusions and potential uses for the ODT model are presented in Section 3.5.

3.2 Model description

3.2.1 The One-Dimensional Turbulence model

In this subsection a short but complete description of the ODT model is presented. For a more detailed discussion of the model approach, the reader is referred to Kerstein (1999) and Kerstein et al. (2001).

The ODT model represents the time evolution of the velocity vector, temperature and additional scalar fields along a line. One-dimensional unsteady diffusion equations are discretized and solved numerically while the effect of turbulence (i.e. the effects of advection and pressure) is modeled by instantaneous non-local stochastic eddy events. In the present work, the ODT domain corresponds to a vertical line representing the time evolution of a horizontally homogenous ABL column, and the governing equations of the model can be written as:

$$\frac{\partial u_i}{\partial t} = -g\delta_{i3} + f(u_2\delta_{i1} - u_1\delta_{i2}) + \nu \frac{\partial^2 u_i}{\partial x_3^2} + \text{eddy events}, \quad (3.1)$$

$$\frac{\partial \theta}{\partial t} = Q + \frac{\nu}{Pr} \frac{\partial^2 \theta}{\partial x_3^2} + \text{eddy events}, \quad (3.2)$$

where x_i is the vector representing the three spatial directions (x_3 is the vertical direction), t is time, $u_i(x_3, t)$ is the velocity vector, $\theta(x_3, t)$ is the potential temperature, ρ is the air density, \bar{p} is the mean pressure, g is the gravitational acceleration, f is the Coriolis parameter, Q is a heat source/sink, ν is the kinematic viscosity, Pr is the Prandtl number, and δ_{ij} is the Kronecker delta. The time evolution of any additional non-reactive passive scalar can be represented in the model by Equation (3.2), after replacing the Prandtl number Pr by the appropriate Schmidt number Sc .

The instantaneous eddy events in Equations (3.1) and (3.2) consist of two mathematical operations representing the effects of advection and pressure. In practice, when an eddy event is selected, the variables at the position z (hereafter z corresponds to the vertical direction x_3) are replaced by the values at $M(z)$ (a mapping function) in the following way:

$$u_i(z) \rightarrow u_i(M(z)) + c_i K(z), \quad (3.3)$$

$$\theta(z) \rightarrow \theta(M(z)). \quad (3.4)$$

The first term on the right hand side of Equations (3.3) and (3.4) is a model for advection by a turbulent eddy based on a triplet map. The mapping function is chosen so that it is conservative (via measure preservation) and does not introduce discontinuities. In addition, it mimics the energy cascade in turbulence by transferring energy from large to small scales in a scale-local fashion (via stretching-folding approach). Defining z_b as the position of the bottom of the eddy and l as its vertical size, the triplet map can be mathematically expressed as (Kerstein et al., 2001)

$$M(z) = z_b + \begin{cases} 3(z - z_b), & \text{if } z_b \leq z \leq (z_b + l/3), \\ 2l - 3(z - z_b), & \text{if } (z_b + l/3) \leq z \leq (z_b + 2l/3), \\ 3(z - z_b) - 2l, & \text{if } (z_b + 2l/3) \leq z \leq (z_b + l), \\ z - z_b, & \text{otherwise.} \end{cases} \quad (3.5)$$

As described by (Kerstein and Wunsch, 2006), the triplet map “takes a line segment, shrinks it to a third of its original length, and then places three copies on the original domain. The middle copy is reversed, which maintains continuity of advected fields and introduces the rotational folding effect of turbulent eddy motion.”

The second term on the right hand size of Equation (3.3) is a kernel function that captures the pressure-induced energy redistribution among velocity components, creating a tendency towards isotropy in the flow. In this term, $K(z) = z - M(z)$ is the distance that the fluid parcel is displaced during an eddy event, and c_i corresponds to the amplitude of energy redistribution, which can be obtained by requiring the change of total energy due to the eddy event to be zero. The variation of kinetic energy ΔE_i and potential energy ΔE_g during an eddy event can be written as

$$\Delta E_i = \frac{\rho}{2} \int_{z_b}^{z_b+l} [(u_i(M(z)) + c_i K(z))^2 - u_i^2(z)] dz, \quad (3.6)$$

$$\Delta E_g = -g \int_{z_b}^{z_b+l} [\theta(M(z)) - \theta(z)] zdz. \quad (3.7)$$

Determination of the coefficients c_i in Equation (3.3) is based on the flow energetics. By requiring total energy conservation $\sum_i \Delta E_i + \Delta E_g = 0$ and equipartition of the

energy changes caused by the eddy among the three velocity components (Kerstein et al., 2001; Kerstein and Wunsch, 2006), one obtains

$$c_i = \frac{27}{4l} \left[-u_{K,i} \pm \sqrt{\frac{1}{3} \left(u_{K,1}^2 + u_{K,2}^2 + u_{K,3}^2 + \frac{8gl}{27} \frac{\theta_K^2}{\theta_0} \right)} \right], \quad (3.8)$$

where θ_0 is a reference temperature and

$$n_K = \frac{4}{9l^2} \int_{z_b}^{z_b+l} n(z) [l - 2(z - z_b)] dz, \quad (3.9)$$

for $n = u_i$ or θ . Note that with this definition, the total energy available for the eddy (i.e. kinetic and potential) is proportional to

$$E_a \sim u_{K,1}^2 + u_{K,2}^2 + u_{K,3}^2 + \frac{8gl}{27} \frac{\theta_K}{\theta_0}. \quad (3.10)$$

The key feature that determines the success of the model is the sequence of eddy events that occur during a simulation. The probability distribution that governs the occurrence of stochastic eddies in ODT is linked to the instantaneous velocity and temperature fields being simulated. At a given time t , λ is defined as the probability of occurrence of eddies with a size l at the location z_b . From dimensional arguments, λ is proportional to $(l^2\tau)^{-1}$, where $\tau(z_b, l, t)$ is the eddy turnover time scale,

$$\lambda(z_b, l, t) \equiv \frac{C_\lambda}{l^2\tau(z_b, l, t)}, \quad (3.11)$$

and C_λ is a constant of proportionality. Furthermore, the total available energy required for the eddy can be related to the time scale $\tau(z_b, l, t)$ by dimensional arguments by

$$\frac{l^2}{\tau^2} \sim E_a - \frac{Z\nu^2}{l^2}. \quad (3.12)$$

For simulations resolving the Kolmogorov scales, the last term of Equation (3.12) represents the damping effect of viscosity, because any eddy with a time scale much longer than the viscous time scale should be prohibited (Z is a constant of order 1). For simulations that do not resolve the Kolmogorov scales, which is the case in

this work (see next subsection), $Z = 0$ and

$$\lambda(z_b, l, t) = \frac{C_\lambda}{l^3} \sqrt{u_{K,1}^2 + u_{K,2}^2 + u_{K,3}^2 + \frac{8gl\theta_K}{27\theta_0}}. \quad (3.13)$$

The value of C_λ in Equation (3.13) is the only adjustable parameter in the model, and it regulates the number of eddies allowed for a given energy availability in the flow, setting the turbulent intensity.

An important detail in the ODT model is that the three velocity components evolve in time as independent fields. Because continuity cannot be enforced in a one-dimensional domain, the velocity components are not coupled to each other and they do not represent a physical turbulent structure. One consequence of this characteristic of the model is that velocity fluctuations are completely uncorrelated. Therefore, the vertical turbulent fluxes have to be estimated from the accumulated transport caused by a series of stochastic eddy events, rather than by correlations between fluctuating variables. For a time interval Δt , the mean vertical turbulent flux of any quantity n ($n = u_i$ or θ) is obtained from the sum of changes on its value due to stochastic eddies, calculated as

$$\text{eddy flux}_n(z) = \frac{1}{\Delta t} \int_z^\infty \sum_t^{t+\Delta t} [n(z')_{\text{after}} - n(z')_{\text{before}}] dz' \quad (3.14)$$

where $n(z)_{\text{before}}$ and $n(z)_{\text{after}}$ correspond to the values of n at given position z before and after the occurrence of an eddy event. Equations (3.1) to (3.14) represent the basis of the ODT model, which has been shown to produce a reasonable representation of many theoretical turbulent flows (Kerstein, 1999; Kerstein et al., 2001).

3.2.2 The filtered ODT model

In most of the previous applications the ODT model has been used to represent turbulent flows down to the Kolmogorov scale (e.g. Kerstein, 1999; Schmidt et al., 2009). However, the number of grid points is proportional to the Reynolds number and for ABL flows with Reynolds numbers of $\sim 10^6$, the number of grid points required leads to considerable computational cost (especially considering the stochastic nature of the model). Therefore, following the common practice in

LES, we introduce a filter to formally separate resolved and sub-grid scales. In this filtered ODT model, resolved scales can be defined by filtering the velocity and temperature fields at the scale $\Delta = dz$. Equations (3.1) and (3.2) become

$$\frac{\partial \tilde{u}_i}{\partial t} = -g\delta_{i3} + f(\tilde{u}_2\delta_{i1} - \tilde{u}_1\delta_{i2}) + \nu \frac{\partial^2 \tilde{u}_i}{\partial x_3^2} - \frac{\partial \tau_i}{\partial x_3} + \text{eddy events}, \quad (3.15)$$

$$\frac{\partial \tilde{\theta}}{\partial t} = Q + \frac{\nu}{Pr} \frac{\partial^2 \tilde{\theta}}{\partial x_3^2} - \frac{\partial q}{\partial x_3} + \text{eddy events}, \quad (3.16)$$

where \tilde{u}_i and $\tilde{\theta}$ are the resolved velocity and temperature fields, τ_i is the SGS vertical stress vector and q is the SGS vertical heat flux. Perhaps at this stage it is useful to point out that in the present approach, the numerical grid dictates the smallest resolved eddy size and thus effectively sets the scale Δ , as typically done in most LES models.

The SGS terms τ_i and q are modeled using a one-dimensional analogy to the eddy-viscosity model

$$\tau_i = -\nu_{SGS} \frac{\partial \tilde{u}_i}{\partial z}, \quad (3.17)$$

$$q = -\frac{\nu_{SGS}}{Pr_{SGS}} \frac{\partial \tilde{\theta}}{\partial z}, \quad (3.18)$$

where Pr_{SGS} is the SGS Prandtl number (a constant value $Pr_{SGS} = 0.4$ is adopted in all simulations) and ν_{SGS} is the SGS eddy-viscosity represented using a one-dimensional version of the Smagorinsky model (Smagorinsky, 1963)

$$\nu_{SGS} = (C_s \Delta)^2 \left[\frac{\partial \tilde{u}_i}{\partial z} \frac{\partial \tilde{u}_i}{\partial z} \right]^{1/2}, \quad (3.19)$$

where C_s is the Smagorinsky coefficient. For homogeneous isotropic turbulence, Lilly (1967) obtained $C_s \approx 0.17$ as the optimal value for simulations where the filter cutoff was in the inertial subrange. The same value is used in the simulations presented here, despite the fact that there is no reason to expect the optimal value of the coefficient to be the same. In true Navier-Stokes turbulence it is known that this value should be smaller for regions of high shear such as near a wall (Deardorff, 1970), and that significant model performance can be accomplished by using dynamically determined coefficients (Germano et al., 1991; Porté-Agel et al.,

2000). Nevertheless, the use of a wall-damping function (Mason and Thomson, 1992) or dynamically evaluated coefficients did not improve significantly the results in ODT simulations.

For ABL simulations with a rough surface, the no-slip boundary condition for the horizontal velocities cannot be enforced directly, and a wall model is needed. For simplicity, the equilibrium wall-model used in LES of ABL flows is also used here. The specific implementation employed here uses the Monin-Obukhov similarity functions to determine the wall stress as a function of the resolved velocity at the first grid point following the approach described in Kumar et al. (2006):

$$\tau_w = - \left[\frac{\kappa}{\ln(dz/z_0)} - \psi_M \right]^2 (\tilde{u}_1^2(dz) + \tilde{u}_2^2(dz)), \quad (3.20)$$

$$\tau_{i,3}^{wall} = \tau_w \left[\frac{\tilde{u}_i(dz)}{(\tilde{u}_1^2(dz) + \tilde{u}_2^2(dz))^{1/2}} \right], \quad (3.21)$$

where τ_w is the total wall shear stress, $\tau_{i,3}^{wall}$ is the partitioning of the total shear stress into x_1 and x_2 directions, $\tilde{u}_i(dz)$ are the horizontal velocities at the first grid point, z_0 is the roughness height, and ψ_M is defined in terms of the Monin-Obukhov similarity function for the mean velocity gradient as $\int_{z_0/L}^{z/L} \frac{(1-\phi_M(x))}{x} dx$. The same set of similarity functions adopted by Kumar et al. (2006) is employed here.

For the representation of the model canopy in the simulations, two possible approaches exist within the ODT framework. The most straightforward approach is to add a canopy drag to the forcing on the right hand side of Equation (3.15), as first done by Shaw and Schumann (1992). In this case, the drag force d_i is defined as

$$d_i = -C_d a P_{ij} \tilde{u}_j (\tilde{u}_k \tilde{u}_k)^{1/2}, \quad (3.22)$$

where C_d is the drag coefficient, a is the leaf area density and P_{ij} is the projection matrix, which is used to obtain an effective partition of the leaf area density facing the three spatial directions (Pan et al., 2014). An alternative approach would be to include the effect of the canopy directly in the kernel $K(z)$, by removing the requirement that $K(z)$ conserve total energy (i.e., $K(z)$ would represent a net loss of energy to canopy drag). However, this would require significant modification of the ODT framework and the simple approach of including the drag force directly in the momentum equation is adopted here.

3.3 Simulations setup and experimental data

3.3.1 Rough-wall ABL simulations

As a first test of the filtered ODT model with the SGS model described in section 3.2, simulations of an ABL column without resolving the canopy (i.e., rough-wall ABL simulations) were performed. Steady-state simulations for neutral, unstable and stable temperature stratifications were performed. For the neutral and unstable cases, the simulation domain was set to 1000 m and the initial height of the inversion layer was set to $z_i = 800$ m. For the stable case the domain was 400 m and initial $z_i = 100$ m.

For the steady-state simulations, the potential temperature field was initialized with a constant value of $\theta_0 = 290$ K within the ABL and a gradient $d\theta/dz = 0.1 \text{ K m}^{-1}$ above z_i . The simulation was driven by a mean pressure gradient in geostrophic balance above the inversion (i.e., the mean pressure gradient force in Equation (3.15) was replaced by $f(U_g\delta_{i,2} - V_g\delta_{i,1})$). A value of $f = 10^{-4} \text{ s}^{-1}$ was used together with a constant geostrophic wind equal to $(U_g, V_g) = (16, 0) \text{ m s}^{-1}$ for neutral simulations, and equal to $(U_g, V_g) = (10, 0) \text{ m s}^{-1}$ for unstable and stable simulations.

In addition, to assess the behavior of ODT in unsteady conditions, a full diurnal cycle simulation was performed. The same setup of the LES simulation presented by Kumar et al. (2006) was used, with a domain of 2000 m and initial $z_i = 800$ m. The simulation was forced by a smoothed version of the observed diurnal cycle of surface heat flux obtained from the HATS 2000 field experiment (Horst et al., 2004), starting at 17:00 local time. Thus, the simulation comprises the end of the convective period, followed by a 12h-period of nocturnal stable ABL, leading to the development of a new convective ABL. The potential temperature field was initialized with a constant value of $\theta_0 = 300$ K within the ABL and a gradient $d\theta/dz = 0.01 \text{ K m}^{-1}$ above z_i . The geostrophic wind varied in time as proposed by Kumar et al. (2006) (with $f = 1.45 \times 10^{-4} \text{ s}^{-1}$) in order to match the friction velocity observed in the experiment. Note that for consistency the same vertical grid resolution used in the LES by Kumar et al. (2006) is used in the ODT simulations ($dz = 12.5$ m).

Boundary conditions at the ground for horizontal velocity components were

specified using Monin-Obukhov similarity as discussed in the previous section. The vertical velocity was set to zero and an imposed heat flux was used in the equation for temperature. At the top of the domain, no-flux boundary conditions were used for horizontal velocity components and for temperature, while the vertical velocity was set to zero.

The value of the only tunable coefficient, C_λ , was determined to optimize the reproduction of the velocity profile for the mean streamwise velocity in the neutral surface layer. This value was used for all the rough-wall simulations. The steady-state simulations were run for 6 hours and the results presented are averaged over the final 5 hours of the simulation. In addition, to reduce the intrinsic variability due to the stochastic nature of the model, results were further averaged over 15 realizations (time and/or ensemble averages are represented by an overbar). Diurnal cycle results correspond to 15 realizations of the 24-hour cycle. Detailed information about the simulation setups can be found in Table 3.1. Note that a time step is not specified, since ODT uses a variable time step that is dynamically calculated to maintain the probability of eddy events small enough to permit the use of efficient techniques to determine the eddy probability distribution (see Appendix A in Kerstein (1999)).

3.3.2 Canopy-resolving ABL simulations

To test the capabilities of ODT in reproducing turbulence statistics within the canopy roughness sublayer, canopy-resolving simulations of neutral ABL were performed. Simulations corresponded to three experimental data sets. Only a brief description of each experiment is provided here and the reader should refer to the original manuscripts describing each experiment for more details.

The first simulation setup corresponds to the CHATS field experiment (Patton et al., 2010), which consisted of measurements of the flow through a 10 m tall deciduous walnut orchard in Dixon, California. Conditions during no-leaves and with-leaves periods were simulated using the leaf area density data provided by Dupont and Patton (2012). Simulation outputs were compared to thirty-minute turbulence statistics corresponding to near-neutral stability conditions presented by Dupont and Patton (2012).

The second simulation was designed to match the Mahomet cornfield experiment

Table 3.1. Setup for ODT simulations. The canopy-resolving simulations are based on field and laboratory experiments that will be used for assessment of simulation results: ¹orchard data from Patton et al. (2010) (the different LAI and u_* corresponds to no-leaves and with-leaves periods); ²cornfield data from Gleicher et al. (2014); ³laboratory data from Raupach et al. (1986) and Coppin et al. (1986). ⁴Note that the drag coefficient reported by Raupach et al. (1986) is divided by 2 here, because they use a (1/2) in the definition of the drag force.

	Rough wall			Canopy		
	Neutral	Unstable	Stable	Diurnal-cycle	Orchard ¹	Cornfield ²
Domain height [m]	1000	1000	400	2000	1200	240
Initial inversion height (z_i) [m]	800	800	100	800	1000	200
Grid resolution (dz) [m]	0.5, 1, 2, 5 (16,0)	2 (10,0)	0.8 (10,0)	12.5 Figure 3.5	0.5, 1 —	0.2 —
Forcing (U_g, V_g) [m s^{-2}]	—	—	—	—	—	—
Forcing (pressure gradient) [m s^{-2}]	0.0	0.1	-0.005	Figure 3.5	0.0001 0.0	0.00115 0.0
Surface heat flux [K m s^{-1}]	0.02	0.02	0.02	0.02	0.02	0.02
Surface roughness (z_0) [m]	—	—	—	—	10	2
Canopy height (h) [m]	—	—	—	—	0.25	0.25
Drag coefficient (C_d) [-]	—	—	—	—	0.7, 2.5 1/3	3.3 0.28, 0.28, 0.44
Leaf area index (LAI) [-]	—	—	—	—	—	—
LAI projection ($P_{\alpha\alpha}$) [-]	—	—	—	—	—	—
Scalar source [s^{-1}]	—	—	—	—	—	—
ODT coefficient (C_λ) [-]	11	11	11	11	4.5	4.5
Final inversion height (z_i) [m]	800	850	220	Figure 3.5	1000	200
Friction velocity (u_*) [m s^{-1}]	0.50	0.44	0.24	Figure 3.5	0.30, 0.32 —	0.52 —
Scalar scale (s_*) [-]	—	—	—	—	—	—

described by Gleicher et al. (2014). Simulation results were compared to the ensemble mean of 15 30-min runs from the 2 m tall cornfield for the period between 9:30 and 17:00 local time on 10 July 2011 presented by Pan et al. (2014). The leaf area density data provided by Wilson et al. (1982) corrected for the small leaf area index difference was used in the ODT simulations. Simulation results were also compared to the second-order closure model predictions provided by Gleicher et al. (2014) and to the LES results reported by Pan et al. (2014).

The third simulation corresponded to the wind-tunnel model canopy presented by Raupach et al. (1986). This experiment was chosen because it included measurements of scalar dispersion from an elevated plane source (in reality, several line sources oriented in the spanwise direction and separated in the streamwise direction). The model canopy consisted of bluff elements with $h = 60$ mm of height and 10 mm of width, allocated in a diamond array with a free-stream velocity of 11.25 m s^{-1} . The scalar heat source was located at $0.8h$ and had a power of 275 W m^{-2} . The upwind edge of the scalar source was placed at $x/h \approx 7.3$ so that turbulence is close to being fully developed (i.e. far enough from the canopy edge). Turbulence statistics were provided by Raupach et al. (1986) and the analysis of scalar dispersion was presented by Coppin et al. (1986). Note that experimental results reported by Coppin et al. (1986) suggest that even at the farthest downstream measuring station (the one used here, located at $x_1 = 2.47$ m, which corresponds to a distance of 2.03 m or approximately $34h$ from the source edge) the scalar plume is still developing above the canopy but it appears to be fully developed inside the canopy. An ODT simulation with spatial evolution in the streamwise direction, instead of time evolution of a vertical column, was developed in order to better represent the experimental setup (i.e. $u_i(x_3, t)$ is replaced by $u_i(x_1, x_3)$). The conversion of time into streamwise direction was done using a bulk velocity representative of the mean streamwise advection, obtained from the ratio of the momentum flux integral to the mass flux integral across the 1-D domain (Echekki et al., 2001). The ODT simulation was evolved for 100 seconds to reach equilibrium in the flow statistics, after which a constant source equal to 225 s^{-1} was applied. The experimental profiles of mean, standard deviation and vertical flux of scalar obtained in the farthest downstream measuring station were compared to those simulated by ODT at the same distance. As in the ABL diurnal cycle case, in this version time averages are not possible and results from 15 ODT ensembles are

presented. Because in this simulation the time step dt directly controls the spatial resolution in the streamwise direction, a fixed maximum time step $dt = 10^{-4}$ s corresponding to $dx_1 \approx h/100$ was used.

In all plant-canopy ODT simulations the domain was $120 h$ (h is the height of the canopy) with an inversion layer at $100 h$. For the wind-tunnel case, the domain was $10 h$ with the inversion starting at $9 h$ (in order to match the experimental conditions). For simplicity in the evaluation of streamwise statistics, canopy simulations were carried out without the Coriolis term (a constant mean streamwise pressure gradient force F_i was applied). Details of the simulation setup are shown in Table 3.1. For the plant canopy simulations, the value of $C_\lambda = 4.5$ was chosen to provide better agreement with observed data of mean streamwise velocity above the canopy ($C_\lambda = 11$ was used for the wind-tunnel case due to the very low LAI). All the other parameters are the same as the ones used for rough-wall ABL simulations.

3.4 Results and Discussion

3.4.1 Rough-wall neutral ABL simulations

The first critical test of the filtered ODT model is the reproduction of the logarithmic law-of-the-wall in the surface layer under neutral conditions. More specifically, the prediction for the mean streamwise velocity ($\bar{u}/u_* = (1/\kappa) \log(z/z_0)$), vertical gradient of streamwise velocity ($\phi_M = 1$), vertical eddy diffusivity ($K_M/\kappa z u_* = 1$) and vertical velocity standard deviation ($\sigma_{u_3}/u_* = 1.25$) are assessed. Results of four grid resolutions show similar logarithmic behavior for the same value of C_λ (Figure 3.1a), indicating that the SGS model allowed ODT to be grid-independent, which was not achieved in the previous SGS models proposed by Kerstein and Wunsch (2006). Note that the value of C_λ was chosen in order to obtain a logarithmic profile in the surface layer, which is the only adjustment present in the model (all the other results are not adjustable). The value of ϕ_M close to the wall is close to one (the theoretical prediction, Figure 3.1b), and despite the small overestimation this result is quite encouraging given that ϕ_M is very sensitive to the SGS model. Note that most Smagorinsky-type SGS models used in LES provide inaccurate predictions of ϕ_M near the wall, with large overpredictions in most of the surface layer (e.g., see Andren et al., 1994; Porté-Agel et al., 2000; Bou-Zeid

et al., 2005; Brasseur and Wei, 2010). This overestimation is also present in the ODT simulations, but it is less accentuated and more localized than in most LES models that use a constant Smagorinsky coefficient. As the total flux of momentum in the neutral ABL is constrained by momentum balance, the overestimation of velocity gradients leads to an underestimation of the eddy diffusivity, as seen in Figure 3.1c. The underestimation in velocity standard deviation (see Figure 3.1d) is a characteristic of the ODT model (e.g. Kerstein et al., 2001; Schmidt et al., 2003), but because the vertical turbulent transport is caused by stochastic eddies rather than by the vertical velocity fluctuations, this ODT feature does not necessarily result in underprediction of vertical transport of scalar. In general, this first set of results reaches the overall goal of making ODT not dependent on SGS-model adjustments, avoiding the inclusion of a second parameter to be defined for different types of simulations.

The contribution of stochastic eddies and SGS model to the total mean momentum flux is shown in Figure 3.2a for the coarse simulation with $dz = 5$ m. It can be observed that the stochastic eddies capture well the dominant momentum transport caused by turbulence throughout the domain, while the SGS model compensates the insufficient resolution of the model very close to the wall. As expected, the contribution from the SGS model close to the wall is reduced with increasing grid resolution (see Figure 3.2b). The effect of the temperature inversion in suppressing stochastic eddies above z_i is also clear from the vanishing stress above z_i .

The two main components of the resolved turbulent kinetic energy (TKE) balance, namely shear production (estimated as $P_s = -\text{eddy flux}_{u_i}(\partial \bar{u}_i / \partial z)$) and SGS dissipation ($\epsilon_{SGS} = \overline{\tau_i \partial \tilde{u}_i / \partial z}$) are investigated next. Figure 3.2c shows that the SGS dissipation rate is grid-independent and reasonably matches the production of turbulence kinetic energy, suggesting that the SGS model is removing energy at the appropriate rate from the simulation.

The spectral density of streamwise (E_{u_1}) and vertical (E_{u_3}) velocity components for simulations with $dz = 0.5$ and 1 m are analyzed in Figure 3.3a-b. The spectra were calculated from time series outputs using Taylor's frozen turbulence hypothesis. In addition, the variable time step of ODT presents some difficulties and the time series was first mapped into a constant time step series using linear interpolation. The spectra for several heights in the surface layer (i.e. in the range $0.01 \leq z/z_i \leq 0.1$) collapse when normalized by the surface-layer scales. The spectra for the

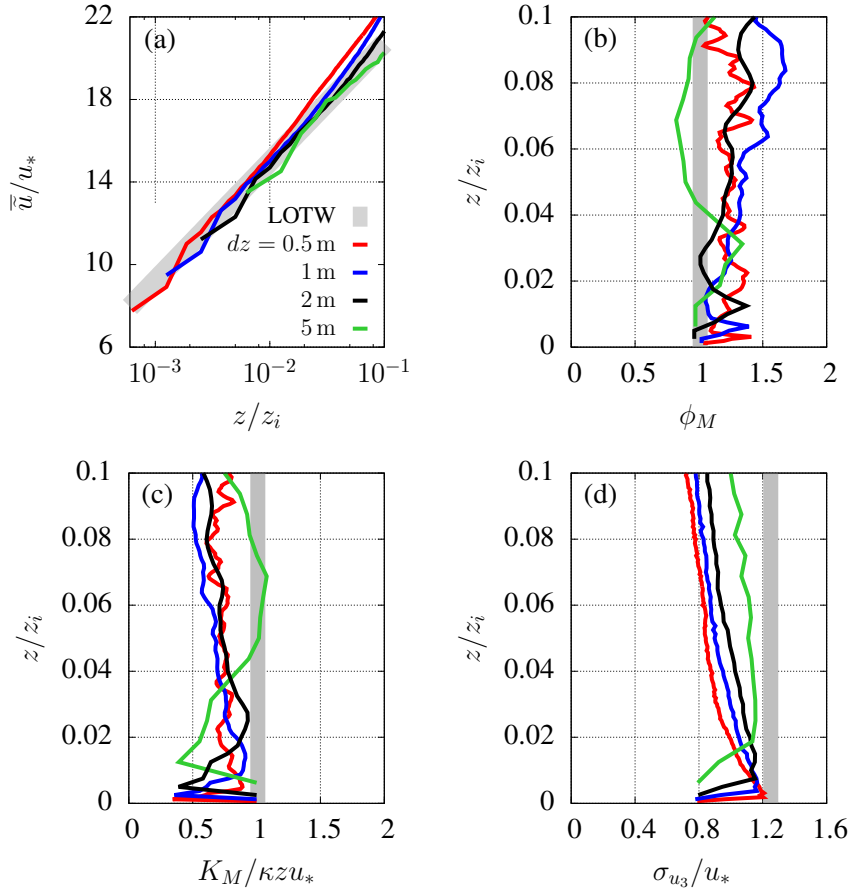


Figure 3.1. Surface layer results for neutral ABL simulations. (a) Normalized mean streamwise velocity, (b) normalized vertical gradient of streamwise velocity, (c) eddy viscosity and (d) vertical velocity standard deviation for four different resolutions ($dz = 0.5, 1, 2$ and 5 m in red, blue, black and green lines, respectively). The gray line represents the law-of-the-wall (LOTW) predictions.

streamwise velocity presents a transition from an approximate k^{-1} slope in the production range to a $k^{-5/3}$ inertial sub-range. The vertical velocity spectra also displays a $k^{-5/3}$ inertial subrange. Note that in the log-log scale plots shown in Figure 3.3a-b, the performance of the SGS model proposed here is much better than that obtained by the same model in LES (e.g., see Bou-Zeid et al. (2005) results for Smagorinsky model with constant coefficient).

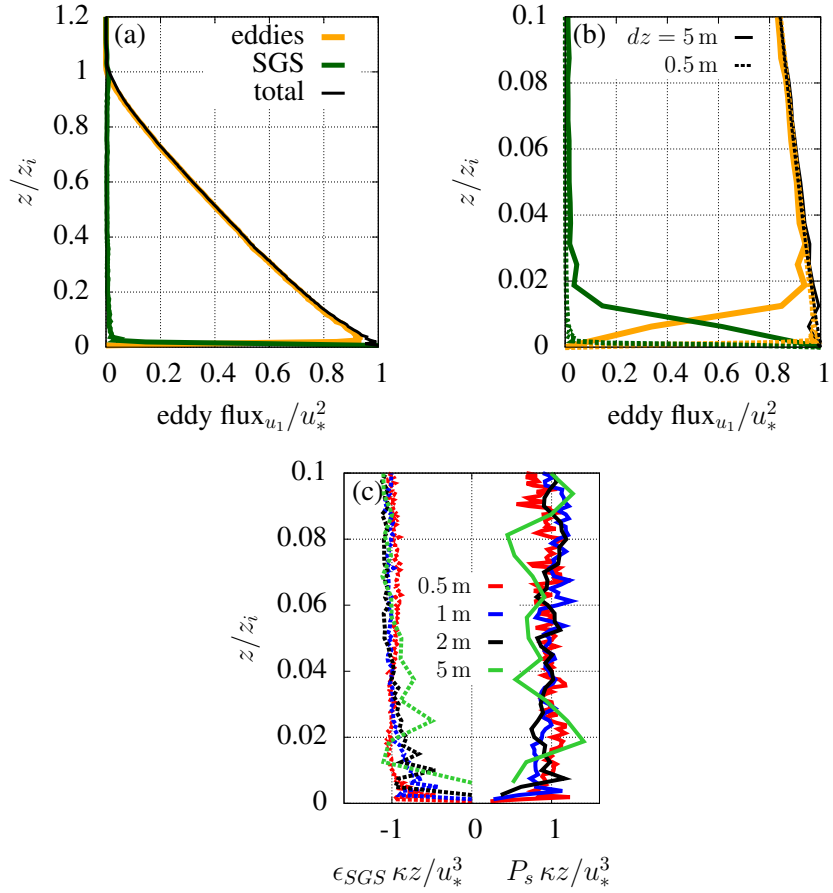


Figure 3.2. Results for neutral ABL simulations. (a) Vertical flux of streamwise velocity caused by the stochastic eddy events (yellow), SGS model (green) and total flux (black), for $dz = 5\text{ m}$. (b) Same as (a) for surface layer and $dz = 5$ and 0.5 m (solid and dashed lines, respectively). (c) TKE shear production (positive values) and SGS dissipation rate (negative values) normalized by $u_*^3/\kappa z$

3.4.2 Rough-wall stratified ABL simulations

Figure 3.4 shows the same basic statistics presented in Figure 3.1, but for the ODT simulations with imposed positive and negative surface heat fluxes (see Table 3.1). Although a specific C_λ adjustment would likely improve the results, we chose to present results generated with the same C_λ value used for neutral simulations, in order to evaluate the model's ability to represent the ABL under different conditions without case-specific adjustments. Results for stable ABL are in very good agreement with theory for all four variables shown. For the unstable ABL, on the other hand, small deviations are observed, including a smaller gradient in

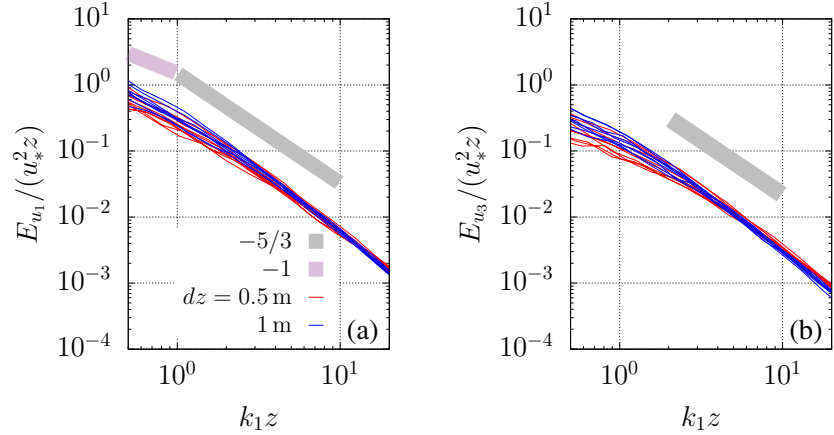


Figure 3.3. (a) Streamwise and (b) vertical velocity spectra for different heights (from 0.01 to $0.1 z_i$), normalized by surface-layer scales.

the \bar{u}/u_* profile, indicating the presence of more mixing than it should exist for the imposed value of heat flux and wind shear. This increased mix resulted in an overestimation of ϕ_M and K_M (in absolute values). Also, the profile of σ_{u_3} for the unstable case has a trend with increasing height that is opposite to MOST.

Despite the discrepancies compared to theory, the ODT model predictions for the unstable case provide a good opportunity to emphasize an important characteristic of the ODT model: the fact that vertical transport is completely dissociated from the vertical velocity fluctuations. Vertical transport is represented by the eddy events, being determined by the sequence of eddy events and the instantaneous concentration profiles upon which these eddy events act. The vertical velocity is produced by redistribution of energy and it is only a small factor in the determination of the probability distribution that governs the occurrence of eddies. Therefore, it is possible in the ODT model framework that the vertical transport be properly represented even if the statistics of the vertical velocity are not well represented. In the present simulation for unstable conditions, the vertical eddy diffusivity has the correct behavior (despite the variability and overestimation) while the vertical velocity variance is misrepresented. Overall, the results presented in Figure 3.4 confirm that the inclusion of the potential energy in Eqn. (3.13) is effective in representing some of the main features caused by buoyancy forcing in ABL flows. Once again, the ODT model predictions seem to be less sensitive to the Smagorinsky coefficient than LES predictions, which require modifications of the

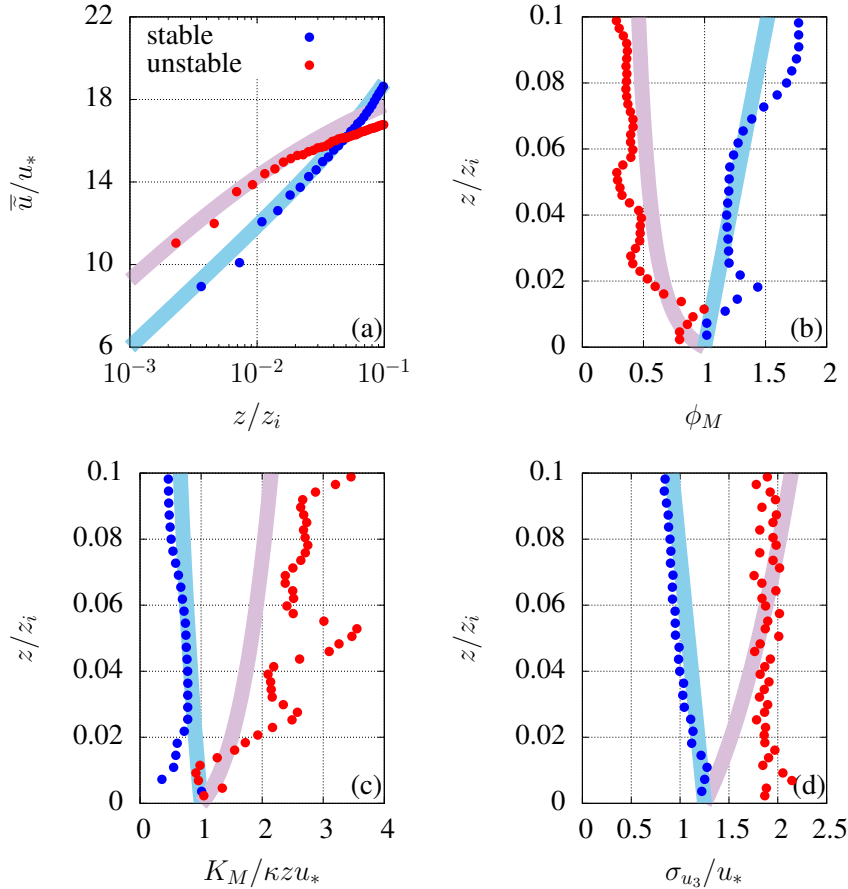


Figure 3.4. Surface layer results unstable (red) and stable ABL simulations (blue). (a) Normalized mean streamwise velocity, (b) normalized vertical gradient of streamwise velocity, (c) eddy viscosity and (d) standard deviation of vertical velocity. The thicker lines represent the MOST

coefficient depending on atmospheric stability (usually accomplished via dynamic modeling approaches (Kleissl et al., 2006)).

The ODT filtered model is also capable of reproducing non-equilibrium conditions fairly well, as illustrated by the results for the diurnal cycle presented in Figures 3.5 and 3.6. Figure 3.5a shows the forcing applied to the model, with a negative surface heat flux and lower geostrophic wind during the night (creating the nocturnal stable ABL) and a positive heat flux and higher geostrophic wind during the day (causing the development of a convective ABL). This is the same forcing applied in a LES simulation by Kumar et al. (2006), and ODT results are comparable to their LES results of time evolution of friction velocity (Figure 3.5b)

and ABL height normalized by Obukhov length (Figure 3.5c). ODT simulations track the time evolution of u_* surprisingly well, except that the values tend to fluctuate more and are $\sim 20\%$ lower during stable night time period. Nevertheless, the two transition periods in which the changes in the geostrophic velocity and surface heat fluxes cause large variations in u_* are well represented by ODT.

ODT results are also in fairly good agreement with LES predictions for the stability parameter z_i/L . The larger scatter during the stable period can be attributed to the lower and more variable values of u_* in the ODT simulation. The lower absolute values of z_i/L during the convective period is a consequence of the lower values of z_i obtained by ODT. This seems to be one of the weaknesses of the ODT model, as it tends to underestimate the growth rate of the CBL.

Examples of profiles of mean potential temperature and streamwise velocity obtained during the stable period and profiles of mean potential temperature and heat flux for the convective period are shown in Figure 3.6. Agreement with LES is reasonable, except for the height and intensity of the low-level jet during the night time period and the already mentioned underestimation of z_i during the convective period. Note that the slower growth of the ABL also causes an excessive heating of the air within the ABL, apparent in the profiles of mean temperature. Two features of the ODT results for the convective boundary layer (CBL) merit discussion. First, the bulk of the CBL is characterized by large fluxes of heat in the presence of very small or negligible gradients in mean temperature (the same is true for other scalars). This feature leads to a failure of simple eddy diffusivity models that use the local mean gradient to model the local flux, leading to the development of models for the “non-local flux” component (e.g., see Deardorff, 1966; Holtslag and Moeng, 1991). The profiles of heat flux presented in Figure 3.6d provide evidence that the ODT model is capable of reproducing the non-local fluxes that dominate the CBL.

The second feature of interest in Figure 3.6d is the small magnitude of the entrainment flux of heat at the top of the ABL. This is the cause for the lower values of z_i obtained by ODT during the convective period. Typically, the ratio between entrainment to surface heat fluxes R ranges between -0.15 and -0.5, with a typical value of $R = -0.2$ (Moeng and Wyngaard, 1989; Sorbjan, 1991; Cancelli et al., 2014). The average value for the convective period (between 10:00 and 16:00 hours) in the ODT simulation is about ten times smaller ($R = -0.02 \pm 0.007$).

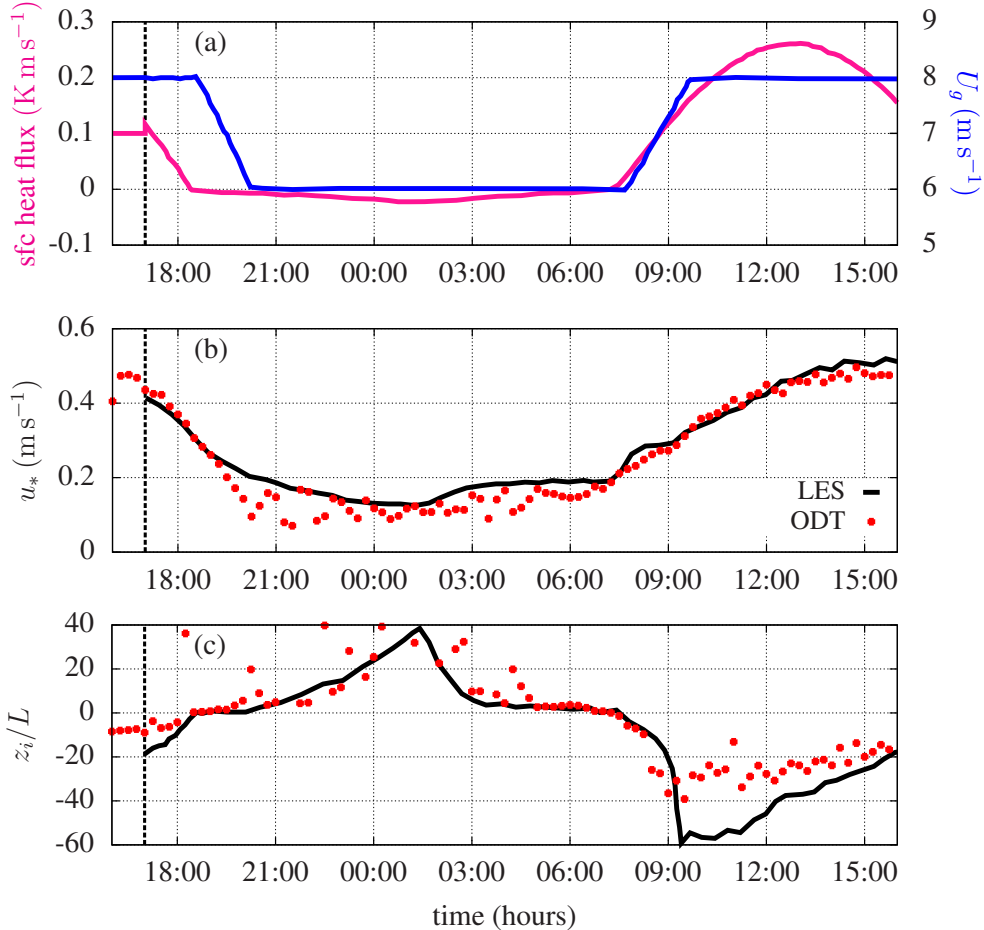


Figure 3.5. Time evolution of (a) the kinematic heat flux (magenta) and streamwise geostrophic wind (blue) applied in the LES and in the ODT ($V_g = 0$). Comparison between LES (black, Kumar et al. (2006)) and ODT (red) results for (b) friction velocity and (c) ABL height divided by Obukhov length

Although ODT is capable of representing buoyancy-driven turbulence through the potential energy included in the probability distribution of stochastic eddies, this representation does not incorporate the thermal plume inertia that drives the air penetration into the inversion layer and causes a significant part of the entrainment flux.

The results presented so far suggest that the filtered version of the ODT model with a Smagorinsky-like SGS model and a wall model based on Monin-Obukhov similarity is capable of reproducing many features of ABL turbulence.

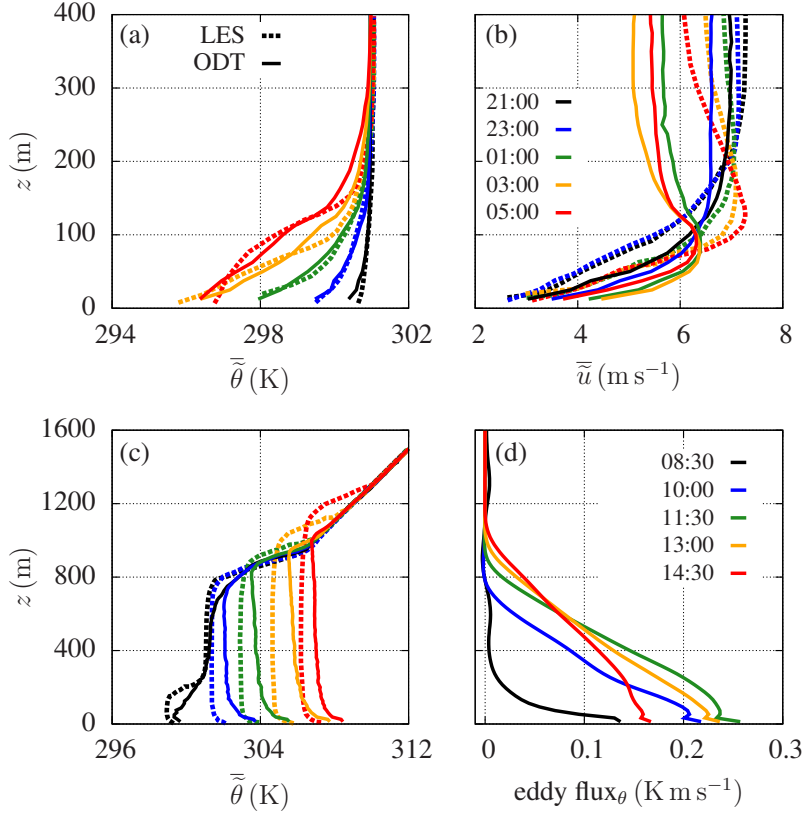


Figure 3.6. Profiles of ABL diurnal cycle. Comparison between LES (dashed, Kumar et al. (2006)) and ODT (solid) results for (a) potential temperature profile and (b) mean streamwise wind velocity during the stable ABL period and (c) potential temperature profiles and (d) heat flux for the unstable ABL period.

3.4.3 Canopy flow, case 1: CHATS experiment

Figure 3.7 shows the profile of turbulence statistics for the no-leaves and with-leaves seasons. In both cases, the observed mean momentum flux is well reproduced by the ODT model, suggesting a good representation of the canopy drag force in the model. The mean streamwise velocity is in good agreement with observations inside the canopy, even though predictions above the canopy are not as good for the case with leaves. The streamwise and vertical velocity standard deviations are underestimated both inside and above the canopy but present the correct profile shape. In addition, the differences between with and without leaves is also well captured by the model. The isotropization of the TKE inside the canopy seems to be well reproduced by the ODT model. Finally, it is important to emphasize

that, as discussed in the context of the unstable surface layer, the underestimation of the vertical velocity variance has no implications for the vertical transport of momentum and scalars inside the canopy.

The characteristic distribution of sweeps and ejections in canopy turbulence can be identified by the positive and negative skewness of streamwise and vertical velocity, respectively. The positive skewness of the streamwise velocity is a direct consequence of the shear in the mean profile and, as such, is captured by the ODT model. However, the negative skewness in the vertical velocity is an indirect consequence of the shear, in the sense that it is actually caused by conservation of mass and the physical shape of the eddies. Because the vertical velocity in the ODT model is not a true velocity associated with physical eddies (it is not related to the stochastic eddies) and continuity is not directly enforced in the model, it yields a vertical velocity field that has no skewness. Given that until very recently LES simulations were unable to capture the correct magnitude of the skewness in canopy turbulence (Pan et al., 2014), it is very encouraging that the streamwise velocity skewness predicted by ODT presents the correct profile shape. In addition, the magnitude is very close to the observed skewness in the upper canopy, and it is overpredicted in the lower canopy. This overprediction is probably related to the stochastic nature of the model, that produces excessive occurrences of large fluctuations in the lower canopy.

Finally, note that Figure 3.7 shows results that are nearly grid independent, demonstrating that the SGS model is behaving properly also for cases with canopy.

3.4.4 Canopy flow, case 2: Mahomet cornfield experiment

For the cornfield experiment, the agreement between ODT results and field data is similar to the one obtained for the CHATS experiment (see Figure 3.8). The two main differences are that in the cornfield case the standard deviation of the streamwise velocity is overestimated above the canopy but well reproduced inside and that the overestimation of the skewness of the streamwise velocity is more pronounced in the lower portion of the canopy. This result demonstrates the ability of ODT in simulating canopy flows for different types of plant canopies, without specific adjustments of the model for each case.

Figure 3.8 also shows simulation results for the same experiment obtained using

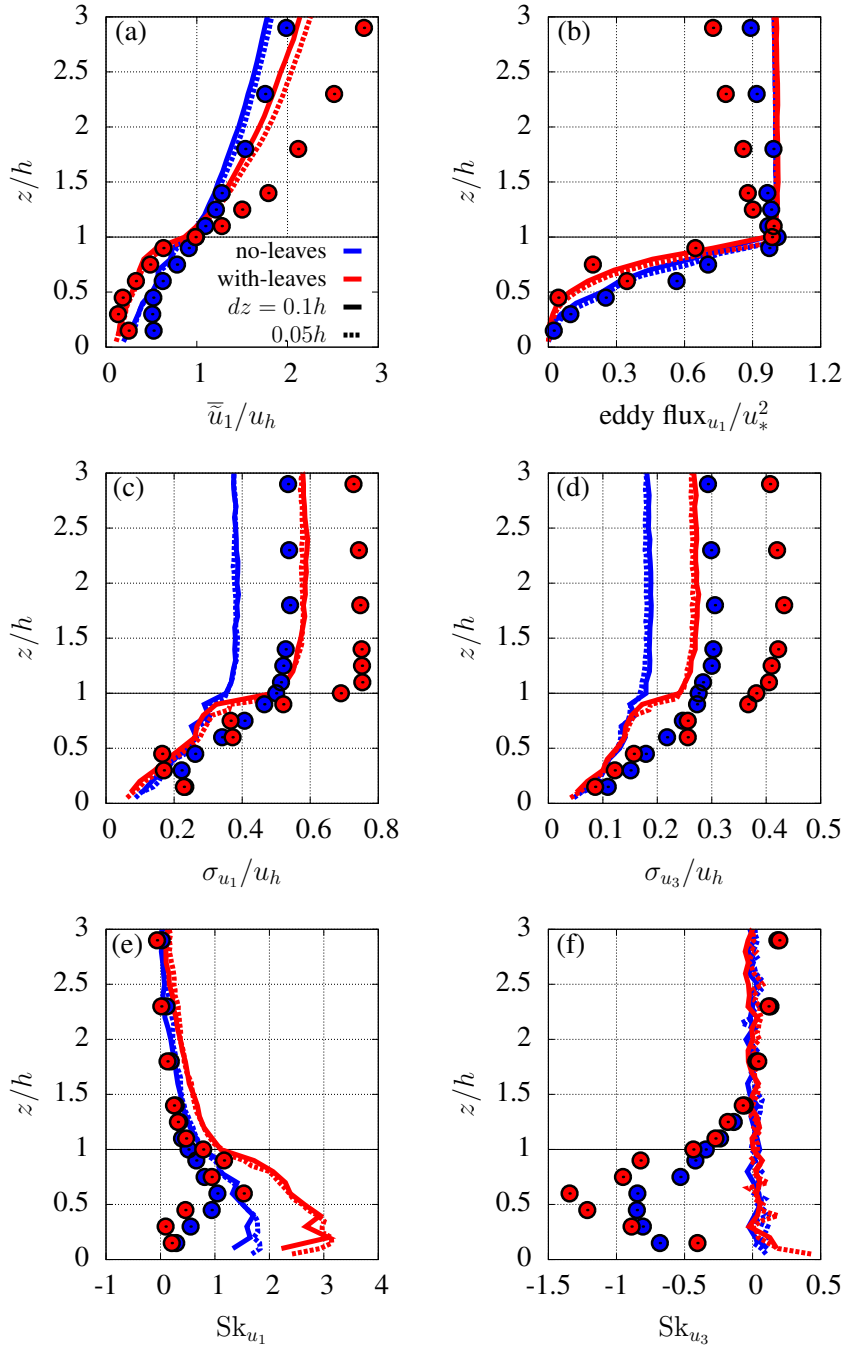


Figure 3.7. Results for neutral surface layer with walnut orchard without leaves (in blue, $h = 10\text{ m}$, $u_h = 2.03\text{ m s}^{-1}$ and $u_* = 0.30\text{ m s}^{-1}$) and with leaves (in red, $h = 10\text{ m}$, $u_h = 1.44\text{ m s}^{-1}$ and $u_* = 0.32\text{ m s}^{-1}$). Circles correspond to experimental results, solid and dashed lines correspond to ODT results for $dz = 0.1h$ and $dz = 0.05h$ respectively. (a) Mean streamwise velocity, (b) mean vertical flux of streamwise velocity, standard deviation of (c) streamwise and (d) vertical velocity, skewness of (e) streamwise and (f) vertical velocity.

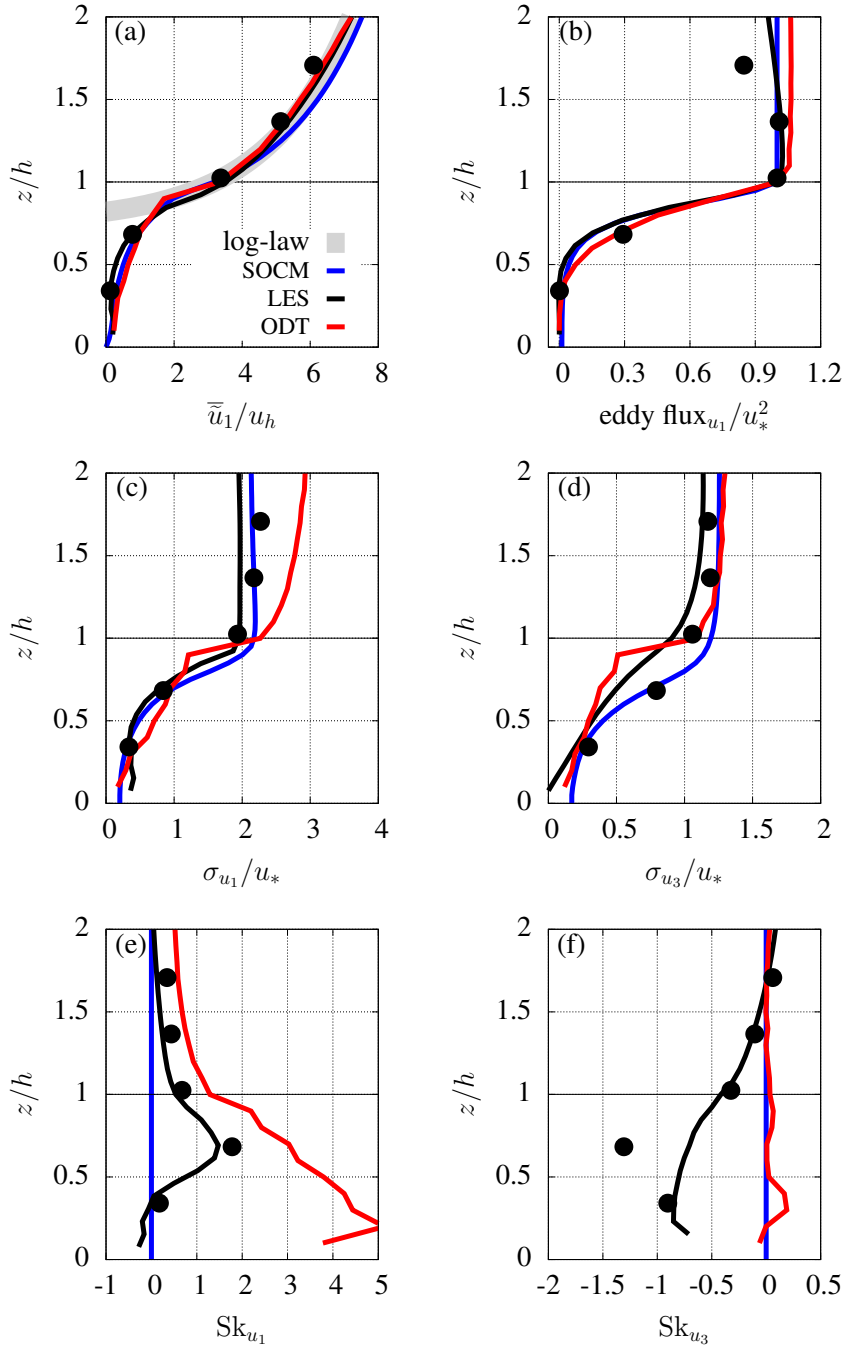


Figure 3.8. Results for neutral surface layer with cornfield ($h = 2$ m and $u_* = 0.52 \text{ m s}^{-1}$). Circles correspond to experimental results, red lines correspond to ODT results for $dz = 0.05h$, blue lines correspond to Second Order Closure Model (SOCM, Gleicher et al. (2014)), and black lines correspond to Large-Eddy Simulation (LES) with plant reconfiguration. (a) Mean streamwise velocity, (b) mean vertical flux of streamwise velocity, standard deviation of (c) streamwise and (d) vertical velocity, skewness of (e) streamwise and (f) vertical velocity.

LES (Pan et al., 2013) and a second-order closure model (SOCM, Gleicher et al. (2014)). Although the SOCM provides good results for first and second-order statistics (by definition the skewness in SOCM is zero), it requires a number of closure assumptions and tuning of several coefficients. As expected, LES results are closer to observed values for all statistics evaluated, and its underestimation of vertical velocity skewness is a good example of how difficult it can be to fully represent the sweep-ejection features even in a model that can explicitly resolve three-dimensional eddies.

The budget for the resolved TKE in the canopy simulations can be written as

$$P_s + T_t + W_d + \epsilon_{SGS} = 0. \quad (3.23)$$

In this equation, which assumes steady-state conditions, P_s is the shear production, T_t is the turbulent transport, W_d is the work done by the resolved velocity field against canopy drag, and ϵ_{SGS} is the SGS dissipation rate (e.g., see Dwyer et al., 1997). In the present ODT simulations, these terms are calculated from

$$P_s = -\text{eddy flux}_{u_i} \frac{\partial \bar{u}_i}{\partial z} \quad (3.24)$$

$$T_t = -\frac{\partial (\text{eddy flux}_{u_i u_i})}{\partial z} \quad (3.25)$$

$$W_d = \bar{u}'_i d'_i \quad (3.26)$$

$$\epsilon_{SGS} = \tau_i \partial \bar{u}_i / \partial z, \quad (3.27)$$

where \tilde{u}'_i and d'_i are the fluctuation part of the resolved velocity and drag force, respectively.

The profiles of the terms in the resolved TKE budget are presented in Figure 3.9. As expected, the shear production of TKE has a peak at the canopy top. The turbulent transport term shows a loss of energy above and in the uppermost levels of the canopy and a gain inside the canopy, representing the net transport of energy into the canopy. This transport feature is also associated with the coherent mixing-layer type eddies present in the canopy roughness sublayer (Finnigan, 2000), and its representation in simple models requires at least second-order closure. The loss of TKE is a combination of the energy dissipation by the SGS model and the work against drag inside the canopy. The overall shape of the profiles is qualitatively

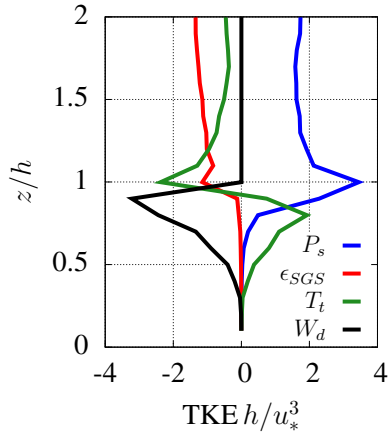


Figure 3.9. TKE budget terms (production in blue, transport in green, SGS dissipation in red, work agains drag in black) for neutral surface layer with corn field ($h = 2$ m and $u_* = 0.52 \text{ m s}^{-1}$).

in agreement with profiles obtained experimentally and using LES (see for example Brunet et al., 1994; Dwyer et al., 1997). Similar results were obtained for the CHATS simulations presented in the previous subsection (not shown).

3.4.5 Canopy flow, case 3: Scalar transport in lab experiment

A two-dimensional plume produced by the ODT simulation is shown in Figure 3.10, which exemplifies the turbulence-like features present in the flow simulated by ODT. Mean profiles (averaged over 15 realizations) of the flow and the scalar concentration statistics are presented in Figure 3.11. As in previous cases, profiles of mean velocity and vertical momentum flux are in reasonable agreement with observations. As in most of the previous cases, the standard deviation of vertical velocity is highly underestimated by ODT. In spite of that, the results for scalar statistics (Figures 3.11d to f) are very good. More specifically, the very good agreement inside the canopy confirms that the filtered ODT model is capable of producing a good representation of vertical transport inside the canopy, a highly non-local process. The large oscillations in the profiles of mean and standard deviation of scalar concentration stem from the small sample (note that no time averaging is performed, so the averaging is limited to only 15 realizations. Overall, this example illustrates the ODT capabilities in simulating turbulent transport of scalars inside canopies, emphasizing the disconnection between vertical velocity

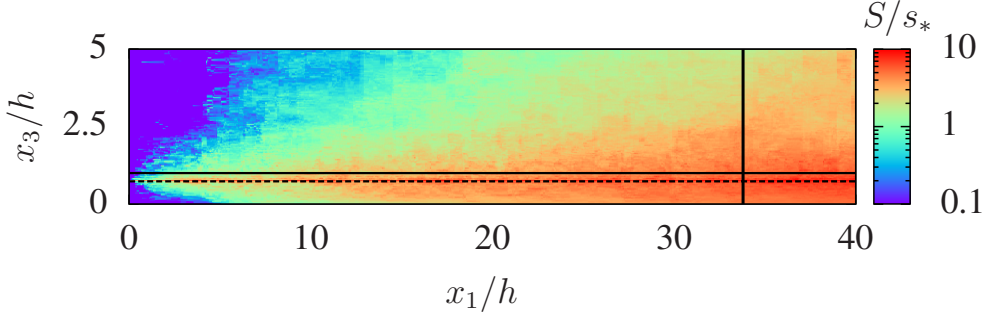


Figure 3.10. Scalar concentration field S normalized by $s_* = (\text{eddy flux}_s/u_*)_h$ as a function of streamwise and vertical directions. Dashed horizontal line represents the source location, solid horizontal line represents the canopy height, and solid vertical line corresponds to measurement position

variance and turbulent transport in this modeling framework. Figures 3.11d and f also show results obtained using a two-dimensional Lagrangian Stochastic (LS) model for the same experiment (Cassiani et al., 2007). The predictions of the LS model are closer to the observations and have much less noise. However, the LS simulations used the flow statistics from the experiments to drive the dispersion model, while ODT predictions require only information about the forcing for the flow and the scalar source.

3.5 Conclusions

In this work, the ODT model was adapted to perform ABL simulations with the presence of a plant canopy. Compared to the other models currently used for the same purpose, ODT situates in between LES and one-dimensional, steady-state RANS models in terms of computational cost and model's ability. Because LES solves the three-dimensional filtered Navier-Stokes and conservation equations, it produces results that are the closest to the reality as can be achieved today, but at the cost of using a high level of computational resources. Given the proper representation of forces and sources/sinks in the model, LES provides reliable results for multiple scalar fields without the need of any parameter adjustment. RANS models, on the other hand, rely on several parameterizations and case-specific adjustments, especially related to turbulence closure. The advantage of

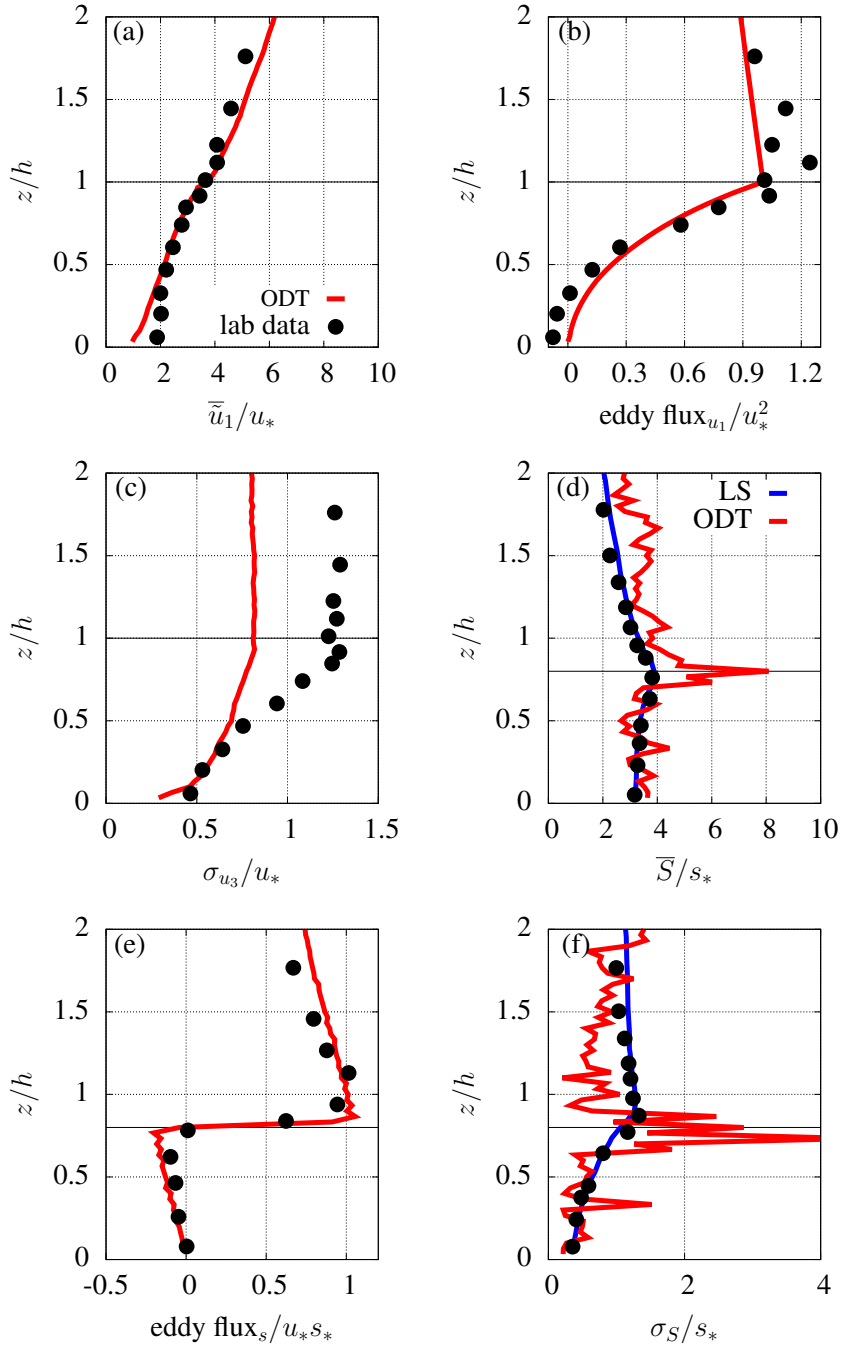


Figure 3.11. Results for canopy model in wind-tunnel ($h = 60$ mm, $u_* = 1$ m s $^{-1}$ and $s_* = 0.23$). Circles correspond to experimental results, red lines correspond to ODT-space, green lines correspond to ODT-time ($dz = 0.03 h$), and blue lines correspond to Lagrangian Stochastic (LS) model (Cassiani et al., 2007). (a) Mean streamwise velocity, (b) mean vertical flux of streamwise velocity, (c) standard deviation of vertical velocity, (d) mean scalar concentration, (e) mean vertical flux of scalar, (f) standard deviation of scalar.

one-dimensional RANS models is the very low computational cost, allowing its use even as a parameterization inside large-scale models, but with the downside of significant increase in computational cost and number of parameterizations when adding new scalar fields. In this work we focused on providing an intermediate tool, in which the computational cost is low compared to LES, turbulence closures are not needed, the addition of new scalar fields is straightforward and case-specific adjustments are kept at a minimum. In order to achieve these goals, a filtered version of the ODT model was developed. In this approach, only the large eddies are represented by stochastic eddies, and an eddy-viscosity SGS model is used to represent the effects of smaller unresolved eddies.

The ODT results presented here achieved the main objectives of the study in a satisfactory way. By keeping only one adjustable parameter, the ODT model generated grid-independent results due to the SGS model developed (previous attempts by Kerstein and Wunsch (2006) did not provide grid-independent results), including coarse-grid simulations whose computational cost is significantly low (compared to LES). The ODT model is not based on flux-gradient closures and captures non-local effects that are very important in cases of unstable ABL and presence of plant canopies. As a low-cost modeling framework for canopy flows, ODT is currently the most complete and general option. Its capabilities include representation of flow and multiple scalars fields simultaneously, transient conditions, coupled source/sink and concentration fields, and a domain that can include the entire ABL. Finally, ODT can be adapted to simulate spatially evolving two-dimensional flows, which may allow for a low cost model to study plume growth, canopy edges and gaps.

Although the cases tested here presented ODT results with similar behavior and trends compared to theory and experimental results, some deviations were observed. For example, the profiles of K_M and ϕ_M in the surface layer in the neutral and unstable cases without canopy, the values of z_i during the unstable period of the diurnal cycle, the mean streamwise velocity above the canopy and the standard deviation of vertical velocity in most of the cases tested did not match the expected values. Some of these divergences are likely related to the inability of the ODT model in representing three-dimensional turbulent eddies. For the canopy case, some discrepancies could potentially be reduced by changing the way the canopy drag is represented in the model, in order to try to eliminate the need of different

C_λ values for the cases with and without canopy.

Finally, we note that due to the SGS model developed and low computational cost achieved, ODT can also be coupled to large scale models instead of being used as a stand-alone single column model. ODT has already been used as a wall-model for LES of high-Reynolds number turbulence in channel flow (Schmidt et al., 2003). In the context of ABL flows, ODT can be couple with LES and used to represent complex physical phenomena close to the ground that cannot be resolved in the numerical grid of LES. In the same line of reasoning, one could envision the use of ODT as an alternative to the traditional surface exchange parameterizations or canopy/urban sub-models used in regional models such as the Weather Research and Forecasting (WRF) model or even in climate models.

Chapter 4

Plant canopy representation in Large-Eddy Simulation using a one-dimensional stochastic wall model

4.1 Introduction

The impact of plant canopies on atmospheric flows is a key component of atmospheric modeling, due to the canopy' ability to extract momentum from the air above and its important role as a source/sink of heat, gases and particles. In numerical models, directly resolving the region inside the canopy would require a vertical grid resolution in the order of $0.1 h$, where h is the canopy height (a resolution of 10 cm for a 1-m tall crop or 1 m for a 10-m tall forest, for example). In Large-Eddy Simulation (LES) studies interested in the effects of plant canopies on the flow, this high resolution typically restricts the model's domain to the lower portion of the atmospheric boundary layer (ABL) (e.g. Huang et al., 2013; Pan et al., 2014). In LES of the entire ABL, or in mesoscale and global circulation models, this level of resolution usually creates a prohibitively high computational cost, and the presence of plants is parameterized through the bottom boundary condition of the model, which provides a net flux of momentum, heat, water vapor, and other variables of interest. Depending the variables studied, parameterizations can go from a simple flux-profile relationship (Kanda et al., 2004) to a set of equations based on energy and moisture budgets that mimics soil-vegetation-atmosphere exchanges (Xue et al.,

2001; Verseghy, 1991). However, these parameterizations do not incorporate the complex effects of canopy turbulence, which involves the development of coherent structures at the top of the canopy and a significant reduction in mean wind and turbulent kinetic energy inside the canopy. These specific characteristics of canopy flows affect the ABL flow within a region as high as two to five canopy heights (Flack et al., 2007) (known as the roughness sublayer), significantly impacting exchanges of momentum, energy and scalars between the atmosphere and biosphere. For instance, the turbulent coherent structures that develop due to the high shear at canopy top are responsible for the dominant, non-local turbulent transport. Conversely, the reduced turbulence inside the canopy can create poorly-mixed environments impacting concentrations and fluxes (Finnigan, 2000). Hence, it is desirable to develop a general and affordable parameterization capable of better representing the flow field and the turbulent transport within different types of plant canopies for large-scale models.

In the atmospheric sciences community, the use of a second numerical model to represent small-scale processes within a large-scale model is known as *superparameterization* (Khairoutdinov et al., 2005). The idea was first developed to improve cloud physics processes in mesoscale and global circulation models (Khairoutdinov et al., 2005; Majda, 2007; Xing et al., 2009), and extended to represent anisotropic turbulence in geophysical flows (Majda and Grote, 2009; Grooms and Majda, 2013). In this work we propose and test a similar approach, in which the representation of the flow within and directly above the canopy is done by a one-dimensional stochastic turbulence model, and the resulting transport of momentum is passed to an LES that simulates the entire ABL. Therefore, the 1D stochastic model can be seen as a superparameterization of the canopy turbulence within a 3D LES of the atmospheric boundary layer.

Most LES models used in atmospheric research have a wall parameterization based on the law-of-the-wall (Piomelli and Balaras, 2002), in which the equilibrium logarithmic relation $\bar{u}/u_* = 1/\kappa \log(z/z_0)$ is applied (in this equation, \bar{u} is the mean streamwise velocity, u_* is the friction velocity, κ is the von Kármán constant, z is height above the wall and z_0 is the roughness length scale). The log-law equation can be directly applied locally and instantaneously (e.g. Bou-Zeid et al., 2005; Moeng, 1984; Shaw and Schumann, 1992) or it can be used to estimate a mean shear stress which is applied locally and instantaneously with the addition

of a perturbation proportional to the local perturbation on the mean streamwise velocity (e.g. Piomelli et al., 1989; Schumann, 1975). In the presence of canopies, the law-of-the-wall can be re-written as $\bar{u}/u_* = 1/\kappa \log[(z + d_0)/z_0]$, where z_0 is enhanced to better represent the canopy' effect on the flow and d_0 (a displacement length scale) is added to lift the height at which the mean streamwise wind velocity goes to zero (Jackson, 1981). Although this relation represents well the flow above the roughness sublayer, it completely neglects the flow complexity present in the canopy layer and essentially imposes a net flux at a reference height. In addition, the parameters z_0 and d_0 need to be defined *a priori* for each type of canopy, and empirical relations that attempt to generalize their values usually require canopy information that is not easily available (Maurer et al., 2015). Another issue with the current wall model is that, since it is based on an equilibrium relation, it is limited to approximately homogeneous conditions in the horizontal domain. In the superparameterization approach proposed here, the one-dimensional stochastic turbulence model replaces the current wall model, eliminating the need to define z_0 and d_0 and providing local vertical and temporal evolution of turbulent transport within and right above the canopy, “extending” the resolved field to the region inside the canopy without changing the LES original domain and resolution.

In this study, we used the One-Dimensional Turbulence (ODT) model developed by Kerstein (1999) and successfully adapted to ABL flows with canopy (see Chapter 3) as a wall model for LES. This ODT-LES combination has already been proposed and tested for simulations of smooth channel flows by Schmidt et al. (2003), providing good agreement on flow statistics (mean and standard deviation profiles) when compared to Direct Numerical Simulation (DNS) results. Here we extend their work by using the ABL-canopy version of ODT to simulate neutral ABL over a cornfield and a walnut orchard with and without leaves, after reproducing the smooth-channel cases and testing a simple rough-wall case. As in the work by Schmidt et al. (2003), we found that despite the different turbulence modeling nature of the two models (stochastic versus deterministic), the two-way coupling provides good results for different types of flows. Another advantage of the ODT model is the possibility of a straightforward incorporation of other variables, such as heat, scalars and particles (see Chapter 3), making ODT a useful tool to represent not only canopy-atmosphere exchanges but also many other ABL surface processes within the LES.

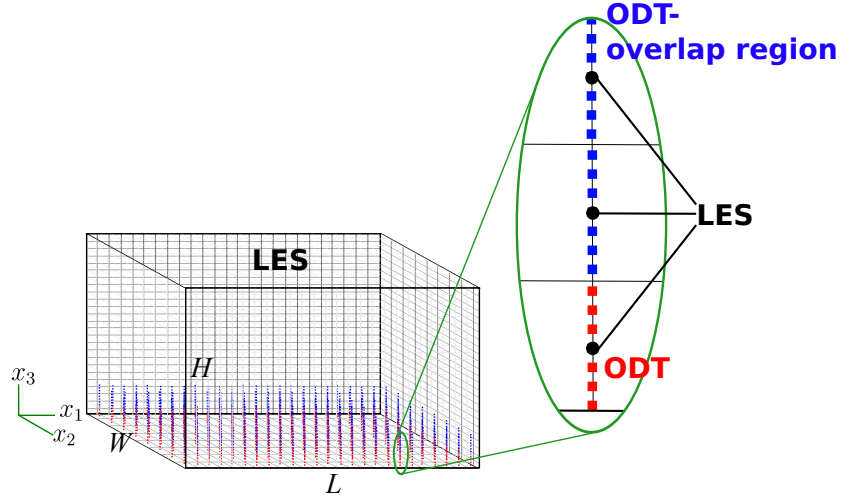


Figure 4.1. Illustration of the ODT-LES model.

The current chapter is organized as follows: Section 4.2 describes the proposed superparameterization approach (hereafter called the ODT-LES model), followed by a description of the simulations performed (Section 4.3). Results of two smooth-channel flows, one rough-channel flow and three flows with canopy are presented in Section 4.4. Suggestions for future improvements to the model and other ABL surface processes that can benefit from the ODT-LES model are discussed in Section 4.5.

4.2 Description of the ODT-LES model

4.2.1 Overview of the two-way coupling approach

In the ODT-LES two-way coupling, the LES part corresponds to a three-dimensional gridded box with size $L \times W \times H$ and grids with size $\Delta x_1 \times \Delta x_2 \times \Delta x_3$ (x_i is the vector representing the three spatial directions and $i = 1, 2$ and 3 correspond to streamwise, spanwise and vertical directions, respectively). The ODT model is introduced as a vertical line inside each LES grid adjacent to the bottom wall, used to represent the flow field close to the surface. An adjustable number of LES grids has an extension of the ODT domain, defined as ODT-overlap region. The LES, ODT and ODT-overlap region comprise the three connected parts of the ODT-LES model (see illustration in Figure 4.1).

The next subsections describe in more details each component of the ODT-LES model. In the notation used here, uppercase letters represent LES variables and lowercase letters represent ODT variables. Tildes represent the LES-resolved scale and hats represent the ODT-resolved scale. Overbars and primes are used to represent mean and fluctuations around the mean, respectively. The ODT-LES model has three different velocity fields, namely

- $\tilde{U}_{i,i=1,3}$: instantaneous LES resolved velocity field,
- $\hat{u}_{i,i=1,3}$: instantaneous ODT resolved velocity field,
- $\tilde{v}_{i,i=1,3}$: average ODT resolved velocity field (averaged over LES timescale).

The LES model resolves the filtered three-dimensional Navier-Stokes equation, whereas the ODT resolves the filtered vertical momentum diffusion equation. On top of the vertical diffusion, two processes are included in the ODT: (i) the effects of stochastic eddies mimicking the vertical turbulent transport of momentum and (ii) the advection caused by the average ODT velocity field \tilde{v}_i (horizontal advection between neighboring ODT columns plus vertical advection within ODT). In summary, ODT provides to LES the velocity field at the first vertical grid points (hereafter “first vertical grid points” refers to the bottom of the domain) and momentum fluxes across the top face of the grids where ODT and ODT-overlap region are present. LES provides to ODT the velocity field for the ODT-overlap region and the ODT top boundary condition. The sequence of steps of the ODT-LES model within one LES time-step Δt can be summarized as follows:

1. at the beginning of a given LES time-step, the current LES velocity field is used to calculate the ODT top boundary condition and the ODT velocity field at the ODT-overlap region;
2. all ODT columns are advanced in time from t to $t + \Delta t$ using a time-step δt which is a fraction of Δt . The values of \tilde{v}_i from the previous LES time-step are used to advect the ODT velocity field;
3. new $\tilde{v}_{i=1,2}$ is obtained as the filtered average of \hat{u}_i over current Δt , and \tilde{v}_3 calculated by imposing continuity within the grid;
4. the accumulated (over Δt) ODT and ODT-overlap region vertical momentum fluxes are passed to the LES subgrid-scale stress tensor;
5. LES is advanced from t to $t + \Delta t$;
6. the values of \tilde{U}_i at the first vertical grid points are replaced by the average ODT values \tilde{v}_i ;

7. the LES pressure-Poisson equation is solved, which imposes continuity in the LES velocity field by correcting the values of \tilde{U}_i ; and
8. the LES pressure correction is applied to \tilde{v}_i and \hat{u}_i .

4.2.2 LES model

The LES model used in this study has been successfully applied in previous works to represent ABL flows under several different conditions, such as neutral (Bou-Zeid et al., 2005), unstable and stable conditions (Kleissl et al., 2006), diurnal cycle (Kumar et al., 2006) and canopy roughness sublayer (Pan et al., 2014). The set of equations that composes the model can be written as

$$\frac{\partial \tilde{U}_i}{\partial x_i} = 0, \quad (4.1)$$

$$\frac{\partial \tilde{U}_i}{\partial t} + \frac{\partial(\tilde{U}_i \tilde{U}_j)}{\partial x_j} = -\frac{1}{\rho} \frac{\partial \tilde{p}}{\partial x_i} + \frac{\partial}{\partial x_j} \left(\nu \frac{\partial \tilde{U}_i}{\partial x_j} \right) + \frac{\partial \tau_{ij}^*}{\partial x_j} + F_i, \quad (4.2)$$

where t is time, \tilde{p} is the resolved pressure field, ν is the kinematic viscosity, τ_{ij}^* is the subgrid-scale stress tensor and F_i is the mean pressure forcing. The scale-dependent Lagrangian Smagorinsky subgrid-scale model described by Bou-Zeid et al. (2005) is used. The continuity constraint (Equation (4.1)) on the velocity field is imposed by solving the Poisson equation for the pressure field \tilde{p} resulting from the divergence of Equation (4.2).

Two aspects of Equation (4.2) are different from the previous versions of this LES model. First, the advection term is traditionally written in rotational form, i.e.,

$$\frac{\partial(\tilde{U}_i \tilde{U}_j)}{\partial x_j} = \tilde{U}_j \left(\frac{\partial \tilde{U}_i}{\partial x_j} - \frac{\partial \tilde{U}_j}{\partial x_i} \right) + \frac{1}{2} \frac{\partial(\tilde{U}_j \tilde{U}_j)}{\partial x_i}, \quad (4.3)$$

in which, for simplification, the second term on the right hand side is combined with the pressure term creating a modified pressure $\tilde{p}^* = \tilde{p}/\rho + \tilde{U}_j \tilde{U}_j/2$, which is then resolved by the pressure Poisson equation. The rotational form is preferred because it conserves kinetic energy (instead of momentum), which is crucial for numerical stability especially when simulating complex unsteady flows (Ferziger and Perić, 2002). Here, we retain the advection term in the divergence form in order to facilitate the incorporation of the vertical turbulent momentum flux from ODT. The second difference is the exclusion of the viscous term due to the high Reynolds

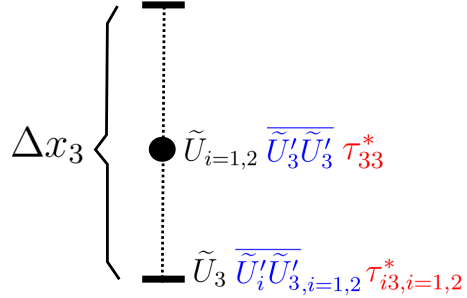


Figure 4.2. Illustration of the velocity and momentum flux vertical positions in the LES staggered grid.

number of the flows. Here the viscous term is included because two smooth channel flow simulations with low Reynolds number are performed (for the rough-wall and canopy-flow simulations the viscous term is neglected).

The numerical code used in this study solves Equations (4.1) and (4.2) using a fully-dealiased pseudo-spectral method in the horizontal directions, a second-order finite difference method in the vertical direction, and a fully-explicit Adams -Bashforth scheme for time advancement. The velocity field and vertical momentum fluxes are arranged in a staggered grid as shown in Figure 4.2. Periodic boundary conditions are automatically enforced by the pseudo-spectral method in the horizontal directions. The top of the domain has stress-free and no-penetration boundary conditions, which correspond to

$$\left. \frac{\partial \tilde{U}_i}{\partial x_3} \right|_{i=1,2} = \tilde{U}_3 = 0. \quad (4.4)$$

The bottom boundary condition comes from the ODT model, as described in Subsection 4.2.6.

4.2.3 ODT model

The ODT model used in this study is equal to the one described by Schmidt et al. (2003) for the smooth-channel simulations, and similar to the one described in Chapter 3 for the rough-channel and canopy-flow simulations. For simplicity, only the model used for the canopy-flow simulation will be described here. The version of the model without the Coriolis force and driven by a constant streamwise pressure force is used, and the governing equation corresponds to

$$\frac{\partial \hat{u}_i}{\partial t} + \frac{\partial \hat{u}_i \tilde{v}_j}{\partial x_j} = PGF + \nu \frac{\partial^2 \hat{u}_i}{\partial x_3^2} - \frac{\partial \tau_i}{\partial x_3} + F_i - C_d a P_{ij} \hat{u}_j (\hat{u}_k \hat{u}_k)^{1/2} + \text{eddies}, \quad (4.5)$$

where \hat{u}_i is the ODT resolved velocity field, τ_i is the subgrid-scale vertical momentum flux vector, C_d is the drag coefficient, a is the leaf area density and P_{ij} is the projection tensor. The models for τ_i and the stochastic **eddies** are defined as described in Chapter 3, in which an adjustable parameter C_λ arises in order to specify the number of stochastic eddies for a given amount of kinetic energy available. A second adjustable parameter Z_λ representing the viscous scale cutoff is also used in the smooth-channel simulations.

The new terms introduced into the ODT model by the ODT-LES coupling are the mean advection term (second term on the left hand side of Equation (4.5)) and the pressure gradient force term (PGF). The former corresponds to a mean horizontal advection among neighboring ODT columns and a mean vertical advection, all driven by the average ODT velocity field \tilde{v}_i . The PGF term is a correction applied in order to re-match the ODT velocities \hat{u}_i and \tilde{v}_i with the LES velocity \tilde{U}_i , since the LES pressure gradient force term $-1/\rho \partial \tilde{p}/\partial x_i$ is responsible for the enforcement of continuity on the velocity field, impacting the entire domain and inevitably changing the velocity field on the first LES vertical grids (which comes from ODT). More details about the pressure correction term is given in Subsection 4.2.7.

In all the simulations without canopy, Equation (4.5) is used with $a = 0$. In addition, in the smooth-channel simulations, the flow is resolved by the ODT down to the dissipation scale, i.e., ODT is ran in “DNS mode” instead of “LES mode”, therefore the subgrid-scale flux term is removed.

Equation (4.5) is solved using a second-order finite difference method for the vertical advection and diffusion terms, a fully-dealiased pseudo-spectral method for the horizontal advection term, and a forward Euler method for the time discretization. The bottom boundary condition is $\hat{u}_i = 0$ for the smooth-channel cases, and a wall model based on the law-of-the-wall for the rough-channel and canopy-flow cases (as defined in Chapter 3). The top boundary condition is an imposed velocity value at $(1+1/n_{ODT})\Delta x_3$ (where n_{ODT} is the number of grid points of the ODT model) obtained from the linear interpolation between $\tilde{v}_i(x_3 = \Delta x_3)$ and $\tilde{U}_i(x_3 = 3\Delta x_3/2)$ (see Figure 4.3).

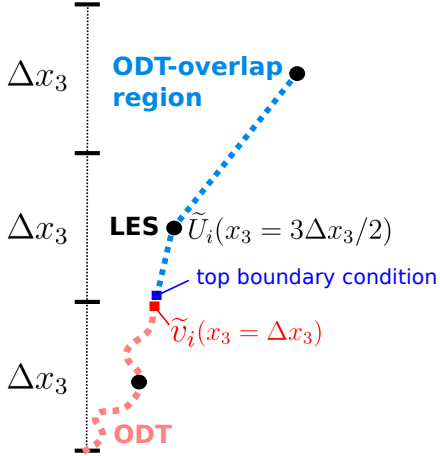


Figure 4.3. Illustration of ODT velocity field top boundary condition and ODT-overlap region velocity field interpolation.

4.2.4 The average ODT velocity field

In order to transfer the ODT velocity information to LES, an LES-scale ODT velocity field (\tilde{v}_i) is defined. For the two horizontal components, $\tilde{v}_{i=1,2}$ corresponds to $\hat{u}_{i=1,2}$ averaged over the previous LES time-step and filtered by a spectral cutoff filter with size $\Delta = (\Delta x_1 \Delta x_2)^{1/2}$. For the vertical component, \tilde{v}_3 is calculated as

$$\tilde{v}_3 = - \int_0^{x_3} \left(\frac{\partial \tilde{v}_1}{\partial x_1} + \frac{\partial \tilde{v}_2}{\partial x_2} \right) dx_3. \quad (4.6)$$

The spectral cutoff filter is used to reduce intrinsic noise in the spectral calculation of the horizontal derivatives of Equation (4.6). Equation (4.6) is defined in such a way as to preserve continuity on the values of \tilde{v}_i that go into the first vertical LES grids (see more in Subsection 4.2.6). The calculation of the average ODT velocity field is done at the end of the ODT time evolution, once every LES time-step.

Because the ODTs are horizontally separated by a distance equal to the LES horizontal grid size, there is no way to estimate an instantaneous horizontal advection between ODT columns. Nonetheless, the value of \tilde{v}_i (from the previous LES time-step) can be used to calculate an advection that behaves as a mean advection for the ODT velocity field, another way for LES to “force” ODT. For the vertical direction, the mean advection is complemented by the stochastic eddies (representing the advection caused by turbulence).

4.2.5 ODT-overlap region

As mentioned above, the ODT-overlap region is the third piece of the ODT-LES model, in which fluxes from stochastic eddies contribute to the LES vertical turbulent flux at a L_{\max} -number of grids above the first vertical grids (see Figure 4.1). The ODT-overlap region is in fact an extension of the stochastic eddies region of the ODT, as the other components of the ODT model (time evolution, vertical diffusion, advection and pressure correction) are not applied in this region. The role of the ODT-overlap region is to allow stochastic eddies with sizes up to $(1 + L_{\max})\Delta x_3$ to exist, and also to allow the turbulent flux caused by them to be computed and added to the LES vertical turbulent flux. Only stochastic eddies with bottom position at $x_3 \leq \Delta x_3$ are allowed. The velocity field inside the ODT-overlap region is obtained as a linear interpolation between $\tilde{v}_i(x_3 = \Delta x_3)$ and $\tilde{U}_i(x_3)$ for $x_3 \leq (1 + L_{\max})\Delta x_3$ (see Figure 4.3). The L_{\max} value is another adjustable parameter of the ODT-LES model. The calculation of the ODT-overlap region velocity field is done at the beginning of the ODT time evolution, once every LES time-step.

4.2.6 LES bottom boundary condition

As mentioned above, the main part of the ODT-LES coupling is done by three ways in which the ODT is used as a bottom boundary condition for the LES. First, \tilde{U}_i at the first vertical LES grid is obtained from \tilde{v}_i . More specifically, due to the staggered grid configuration and the continuity restriction, the matching between the horizontal components of these two velocity fields is

$$\tilde{U}_{i=1,2}(x_3 = \Delta x_3/2) = \hat{\tilde{v}}_{i=1,2} = \frac{1}{n_{\text{ODT}}} \sum_{m=1}^{n_{\text{ODT}}} \tilde{v}_{i=1,2}(x_3 = m\Delta x_3/n_{\text{ODT}}), \quad (4.7)$$

and for the vertical component is

$$\tilde{U}_3(x_3 = \Delta x_3) = \tilde{v}_3(x_3 = \Delta x_3). \quad (4.8)$$

The second coupling element is the total ODT vertical momentum flux at the top of the ODT domain that is passed to the LES subgrid scale stress tensor $\tau_{i3}^*(x_3 = \Delta x_3)$. It includes the ODT momentum flux caused by stochastic eddies (calculated as described in Chapter 3), viscous diffusion, subgrid-scale diffusion

and vertical advection. These fluxes are accumulated (summed) during the ODT time-steps within one LES time-step.

The third step consists on adding to the LES subgrid-scale stress tensor τ_{i3}^* the ODT flux caused by stochastic eddies that extend over the ODT-overlap region. This is done for $\tau_{i3}^*(x_3)$ in which $x_3 \leq (1 + L_{\max})\Delta x_3$.

4.2.7 ODT Pressure correction

As mentioned above, the LES velocity field is adjusted through the pressure gradient force term in order to enforce continuity, which imposes small changes in the values of \tilde{U}_i at the first vertical grid point and makes them different from their original values (that came from \tilde{v}_i). The rematch between the pressure-adjusted \tilde{U}_i and \tilde{v}_i is represented by the *PGF* term in Equation (4.5), which corresponds to the following equation:

$$\tilde{v}_{i=1,2;\text{new}}(x_3) = \tilde{v}_{i=1,2;\text{old}}(x_3) - 2x_3 \frac{\hat{\tilde{v}}_{i=1,2;\text{old}}}{\Delta x_3} + 2x_3 \frac{\tilde{U}_{i=1,2}}{\Delta x_3} \quad (4.9)$$

where $\hat{\tilde{v}}_{i=1,2}$ is obtained from Equation (4.7). After the implementation of the pressure correction at the horizontal components of \tilde{v}_i , Equation (4.6) is used to update the value of \tilde{v}_3 .

The same procedure described above is also implemented to adjust the values of the ODT velocity field (\hat{u}_i), which corresponds to the *PGF* term on Equation (4.5).

4.2.8 Final notes

The ODT-LES coupling described here is similar to the one developed by Schmidt et al. (2003), where more details about the model can be found. The only differences between the two codes are: (i) the LES time and space discretization and subgrid-scale model (the previous model used Runge-Kutta for time discretization and finite differences for all three spatial directions, and the dynamic Smagorinsky model for subgrid-scale stress tensor), (ii) the spectral cutoff filter applied to $\tilde{v}_{i=1,2}$ (non-existent in the previous model) and (iii) the ODT wall, subgrid-scale and canopy models needed for the rough-channel and canopy simulations. As defined by Schmidt et al. (2003), at the beginning of the simulation, the ratio between ODT and LES timesteps ($\delta t / \Delta t$) is set to 15, and it is increased by a factor of two

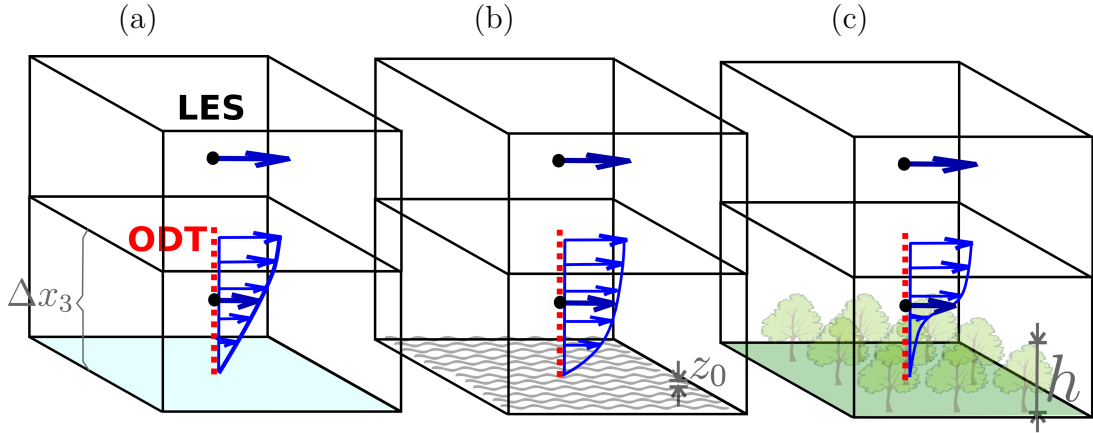


Figure 4.4. Illustration of the three different types of simulations performed with the ODT-LES model: (a) smooth channel, (b) rough channel, and (d) flow through plant canopy.

every time the probability of stochastic eddies reach average values bigger than 0.5 (averaged over one LES time-step). The next section summarizes the simulations performed, followed by the discussion of results in Section 4.4.

4.3 Simulation setup

The ODT-LES model is a useful tool to simulate cases in which the flow close to the wall needs to be resolved, but the computational cost of resolving it with LES is too high. In this study, this modeling approach is tested through three types of simulations, as illustrated by Figure 4.4. The first type corresponds to a smooth channel flow in which the viscous layer present in the region within the first LES grid is simulated by ODT (Figure 4.4a). In the second type, ODT-LES is used to simulate a rough-channel flow with roughness height z_0 smaller than the ODT grid spacing, and both ODT and LES are used to simulate the outer region of the flow (Figure 4.4b). In the third type, LES is used to simulate the entire ABL, and momentum flux caused by the presence of plant canopies with height h smaller than the LES grid spacing is obtained from ODT, which is used to simulate the flow field within the canopy (Figure 4.4c).

Two smooth-channel simulations with Reynolds numbers Re_* corresponding to 395 and 590 were performed ($Re_* = u_* l / \nu$, where u_* and l are the friction velocity and half-channel height, respectively). These simulations were chosen because the

DNS results by Moser et al. (1999) and ODT-LES results by Schmidt et al. (2003) can be used for comparison. It is important to note that the present ODT-LES model only simulates half-channel flows (i.e., the domain goes up to the vertical midpoint of the channel), which may cause small discrepancies around the center of the channel when compared to DNS results (which simulated entire channels). The basic set of parameters used in these simulations is presented in Table 4.1. In both simulations the vertical resolution corresponded to $\Delta x_3 = l/16$, and the viscous layer and buffer zone of the flow were confined within the first grid. ODT was used to resolve the viscous layer and buffer zone using 24 (32) grid points in the simulations with $Re_* = 395$ (590). The initial velocity field corresponded to a linear profile $\tilde{U}_1/u_* = x_3 u_*/\nu$ in the region where $x_3 u_*/\nu \leq 10$ and a logarithmic profile $\tilde{U}_1/u_* = 2.44 \log(x_3 u_*/\nu) + 5.2$ in the region where $x_3 u_*/\nu > 10$, with $\tilde{U}_{2,3} = 0$, plus small random fluctuations in space and among components. These initial profile rules were applied on both ODT and LES velocity fields. Simulations ran for 10000 LES time-steps, each time-step corresponding to $8 \times 10^{-4} u_*/l$, and reached equilibrium on the second half of this period.

After the validation of the model with the smooth-channel simulations, the ODT performance compared with the current LES rough-wall parameterization was tested by one rough-wall channel flow simulation. The chosen case corresponds to the results presented by Bou-Zeid et al. (2005), which used the same LES code used here but with the law-of-the-wall as a wall model instead of ODT. Simulation setup is also presented in Table 4.1, and initial conditions were $\tilde{U}_1 = u_*/0.4 \log(x_3/z_0)$, $\tilde{U}_{2,3} = 0$, plus random fluctuations for both LES and ODT velocity fields. In this case the vertical resolution in the bulk of the flow is $\Delta x_3 = l/64$ in the LES domain, and $\Delta x_3/32$ (or $l/2048$) in the ODT domain. The simulation was carried out through 100000 LES time-steps, each time-step corresponding to $2.5 \times 10^{-4} u_*/l$, and the second half of the simulation time presented steady-state statistics (equilibrium condition).

Finally, the ability to represent canopy flows was tested against three experimental datasets: the Mahomet cornfield experiment (canopy height $h = 2$ m) (Gleicher et al., 2014) and the CHATS experiment during with-leaves and no-leaves periods ($h = 10$ m) (Patton et al., 2010). The canopy information needed for the drag force model, obtained from Pan et al. (2014) and Dupont and Patton (2012), is listed in Table 4.2 together with the other simulation setup parameters. In all three

Table 4.1. Setup for ODT-LES simulations without canopy (l is the half-channel height, u_* is the friction velocity).

	Smooth channel	Rough channel
	$Re_* = 395$	$Re_* = 590$
Domain size ($L \times W \times H$)	$2\pi l \times 2\pi l \times l$	$2\pi l \times 2\pi l \times l$
Grid points ($n_{x_1} \times n_{x_2} \times n_{x_3}, n_{\text{ODT}}$)	$32 \times 32 \times 16, 24$	$32 \times 32 \times 16, 32$
Resolution ($\Delta x_1 \times \Delta x_2 \times \Delta x_3, \Delta_{\text{ODT}}$)	$0.2l \times 0.2l \times 0.0625l, 0.0026l$	$0.2l \times 0.2l \times 0.0625l, 0.002l$
Time-step (Δt)	$0.0008u_*/l$	$0.0008u_*/l$
Surface roughness (z_0)	—	—

Table 4.2. Setup for ODT-LES simulations with canopy.

	CHATS	corn
	with-leaves	without-leaves
Domain size ($L \times W \times H$) [m]	$3840 \times 3840 \times 960$	$3840 \times 3840 \times 960$
Grid points ($n_{x_1} \times n_{x_2} \times n_{x_3}, n_{\text{ODT}}$) [-]	$32 \times 32 \times 32, 30$	$32 \times 32 \times 32, 30$
Resolution ($\Delta x_1 \times \Delta x_2 \times \Delta x_3, \Delta_{\text{ODT}}$) [m]	$120 \times 120 \times 30, 1$	$120 \times 120 \times 30, 1$
Time-step (Δt) [s]	0.3	0.3
Surface roughness (z_0) [m]	0.005	0.005
Canopy height (h) [m]	10	10
Drag coefficient (C_d) [-]	0.25	0.25
Leaf area index (LAI) [-]	2.5	0.7
LAI projection ($P_{\alpha\alpha}$) [-]	1/3	1/3

simulations the ABL height is 960 m, and the LES resolutions are $\Delta x_3 = 30$ m in the CHATS case and 10 m in the corn case, making the canopy confined within the first LES grid. The canopy flow is resolved by ODT with a resolution of $0.1h$ and $0.125h$ in the CHATS and corn case, respectively. The initial profiles and number of time-steps used are the same as in the rough-channel case, and each LES time-step corresponded to 3×10^{-4} eddy-turnover times (one eddy-turnover time is equal to H/u_*).

All simulations presented here were driven by a constant streamwise mean pressure gradient force $F_1 = u_*^2/H, F_2 = F_3 = 0$ (for canopy flows u_* is measured at the top of the canopy). The next section presents the results obtained from these simulations, as well as their comparison with DNS, LES and experimental data. Statistics were obtained by averaging over the horizontal domain and the second half of the simulation time. The ODT parameters C_λ, Z_λ and L_{\max} are discussed as the results are presented.

4.4 Results and Discussion

4.4.1 Smooth channel flow

In order to perform ODT-LES simulations, the ODT parameters C_λ and L_{\max} need to be specified. For the specific case of smooth channels, the parameter Z_λ (viscous cutoff scale) is also needed (it is zero for the other simulations as ODT does not resolve the viscous scale of the flow). As described by Schmidt et al. (2003), Z_λ controls the frequency of small eddies and mostly affects the flow statistics near the buffer zone (where $5 \lesssim x_3 u_* / \nu \lesssim 15$). The importance of Z_λ is clearly seen from the mean streamwise velocity profiles obtained with $Z_\lambda = 0$ and $Z_\lambda \neq 0$ (Figure 4.5), as the small eddies present in the former case destroy part of the viscous layer and the buffer zone, making the profile look logarithmic closer to the wall. Changes in Z_λ from $5 \lesssim Z_\lambda \lesssim 50$ have a small impact on the profile, which can be further adjusted by changing C_λ . In other words, within this Z_λ range, there is a pair (Z_λ, C_λ) that produces good results. Values of $Z_\lambda \gtrsim 50$ caused the simulation to produce incorrect results and destabilize. The adjustment of C_λ is done in order to obtain the correct value of u_* . Higher/lower values than the correct one increases/decreases u_* for a given mean pressure gradient force, violating the

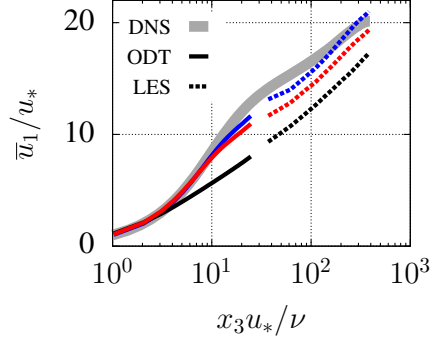


Figure 4.5. Mean streamwise velocity profile for the smooth-channel flow simulation with $Re_* = 395$, $C_\lambda = 20$ and $L_{\max} = 3.5$. ODT (solid lines) and LES (dashed lines) results are shown for $Z_\lambda = 0$ (black), 5 (red) and 20 (blue). DNS result is shown in gray.

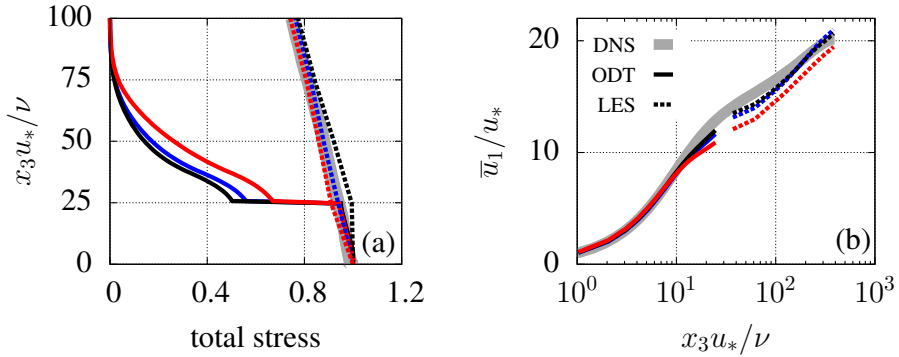


Figure 4.6. Profiles of (a) total stress and (b) mean streamwise velocity for the smooth-channel flow simulation with $Re_* = 395$, $Z_\lambda = 20$ and $L_{\max} = 3.5$. ODT (solid lines) and LES (dashed lines) results are shown for $C_\lambda = 15$ (black), 20 (blue) and 40 (red). DNS results are shown in gray.

mean force balance in the flow. An example can be seen in Figure 4.6, where $C_\lambda = 15$ caused a deviation on the total stress profile from the correct linear profile (obtained with $C_\lambda = 20$), whereas increasing C_λ affected both the total stress and the mean streamwise velocity profiles. Nevertheless, differences among the results are small and only visible when changing C_λ and Z_λ by $\sim 50\%$ or more. Therefore, the ODT-LES coupling is much less sensitive to the choice of parameters than the ODT model, indicating that LES has a significant impact on the ODT result.

As oppose to what was obtained by Schmidt et al. (2003), the L_{\max} parameter did not significantly impact the mean streamwise velocity profile (see Figure 4.7). The choice of the best L_{\max} value was performed by looking into the streamwise

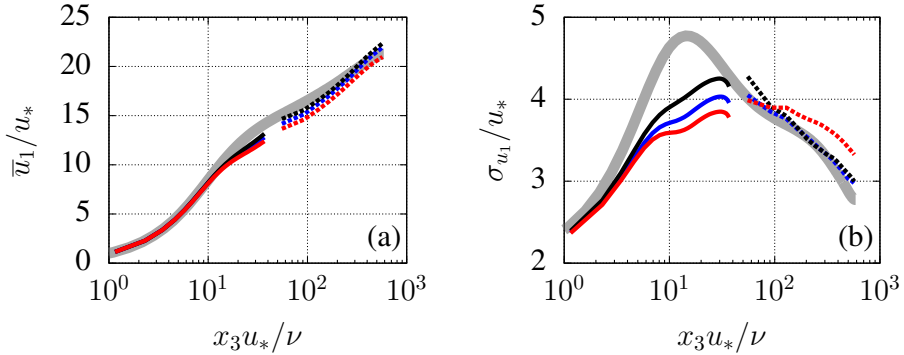


Figure 4.7. Profiles of (a) mean streamwise velocity and (b) streamwise velocity standard deviation for the smooth-channel flow simulation with $Re_* = 590$, $Z_\lambda = 20$ and $C_\lambda = 20$. ODT (solid lines) and LES (dashed lines) results are shown for $L_{\max} = 2.5$ (black), 3.5 (blue) and 4.5 (red). DNS results are shown in gray.

standard deviation profiles, which showed better results in the LES domain for $L_{\max} = 3.5$. It is not clear what is the cause for this specific discrepancy compared to the implementation by Schmidt et al. (2003), but small differences are expected since the two LES models used are not equal to each other.

Figure 4.8 shows the statistics of the ODT and LES velocity fields for the two smooth-channel flow simulations (performed with $Z_\lambda = C_\lambda = 20$ and $L_{\max} = 3.5$). In Figure 4.8a the ODT contribution to the subgrid-scale stress can be observed at the grid points closer to the wall, and the total shear has the appropriate linear profile in the entire domain. The mean streamwise velocity obtained is close to the DNS and the previous ODT-LES results, with good representation of the viscous, buffer and logarithmic regions of the flow (Figure 4.8b). Figure 4.8d shows the standard deviation of \hat{u}_3 and \tilde{v}_3 (both have mean values equal to zero), two variables that are relevant because the former contributes to the stochastic eddies and the latter goes into the LES and is responsible for ODT vertical advection. For the horizontal components the statistics of \hat{u}_i and \tilde{v}_i are the same. The results obtained here for the streamwise and vertical velocity standard deviation in the LES domain are closer to DNS than the results from Schmidt et al. (2003), probably due to the numerical improvements of the present LES code (spectral method in the horizontal discretization and Lagrangian scale-dependent subgrid-scale model). In the ODT domain, on the other hand, the standard deviations obtained here are different from the DNS, whereas results from Schmidt et al. (2003) are closer, a difference

possibly caused by the filter applied on the \tilde{v}_i calculation (needed because of the spectral calculation of horizontal derivatives) which is non-existent in the original model. The lower values of σ_{v_i} obtained here implicate that LES velocity field in the first grid has an underestimated turbulence intensity. In the ODT domain, the reduced turbulence in the streamwise direction and overestimation in the vertical direction may be reflecting an excess of transfer of energy among components through the pressure redistribution term associated with the stochastic eddies (see subsection 3.2.1 in Chapter 3). This does not necessarily translate, however, in a under/overestimation of turbulent transport of scalars in the ODT domain, as the stochastic eddies responsible for the transport depend on the total kinetic energy rather than on each component of it separately. Therefore, the performance of ODT-LES on scalar transport need to be further investigated, and in terms of the two-way coupling of the velocity field we consider these results satisfactory.

4.4.2 Rough channel flow

The behavior of the ODT-LES model in a rough-channel case is tested against the previous LES wall model based on the law-of-the-wall. The main issue with the law-of-the-wall approach is the instantaneous application of a law that is valid for mean quantities. When law-of-the-wall is applied locally, the resulting mean stress does not match the original law prediction due to the local velocity fluctuations (Bou-Zeid et al., 2005). This discrepancy creates the need to filter the velocity field used by the wall model at twice the grid scale (a spectral cutoff filter is used), improving the mean velocity statistics but limiting the model to approximately homogeneous conditions. In the cases over a rough surface, ODT also uses the law-of-the-wall as a bottom boundary condition, therefore “pushing” this approximation closer to the wall (and farther from the LES velocity field). ODT provides to LES a local momentum flux based on an instantaneous velocity field resolved in the vertical direction, removing the need to filter the LES velocity field. However, the almost independent nature of each ODT present in the LES results in fluctuations in \tilde{v}_i that need to be filtered in order to use the spectral method to perform horizontal derivatives, although in this case a filter with size equal to the grid scale was sufficient.

The final statistics of the rough-channel simulation are shown in Figure 4.9.

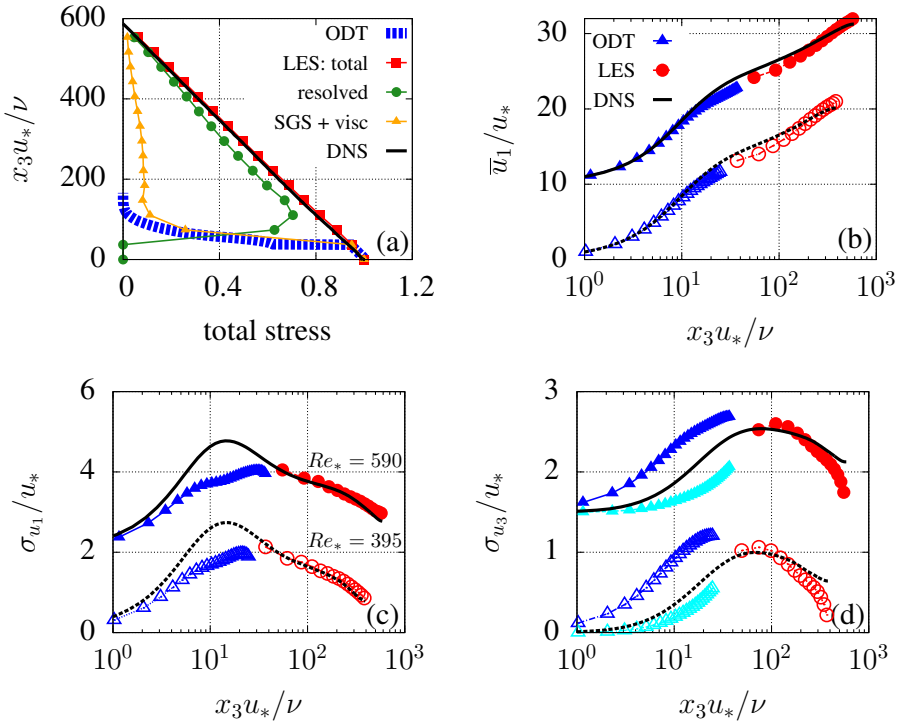


Figure 4.8. Statistics of the velocity field for smooth channel simulations for $Re_* = 395$ (open symbols, dashed lines) and $Re_* = 590$ (filled symbols, solid lines, vertically dislocated), corresponding to ODT (\hat{u}_i , blue) and LES (\tilde{U}_i , red). Results of (a) total shear, (b) normalized mean streamwise velocity, normalized standard deviation of (c) streamwise and (d) vertical velocity. Black lines correspond to DNS results from Moser et al. (1999). (a) corresponds to $Re_* = 590$ only and it also presents the LES resolved shear (green) and subgrid-scale + viscous shear (yellow). (d) also presents the standard deviation of \tilde{v}_3 (cyan).

Mean streamwise velocity and total shear are similar between the law-of-the-wall and the ODT approaches. Some improvement can be observed in the standard deviation profiles in the LES domain when using ODT, namely higher values of both streamwise and vertical components close to the surface and a change on the shape of the streamwise profile. The peak in the value of σ_{u_1}/u_* close to the wall in high Reynolds number has been observed as approximately 3 (Schultz and Flack, 2013), whereas the peak in σ_{u_3}/u_* can be estimated as 1.25 from the MOST (Kaimal and Finnigan, 1994). The shape of the σ_{u_1}/u_* profile is also closer to experimental results when using ODT (see Figure 7 at Schultz and Flack (2013)). This improvement is probably due to the fact that ODT is a numerical model that responds dynamically to the LES forcing, therefore it is a more appropriate

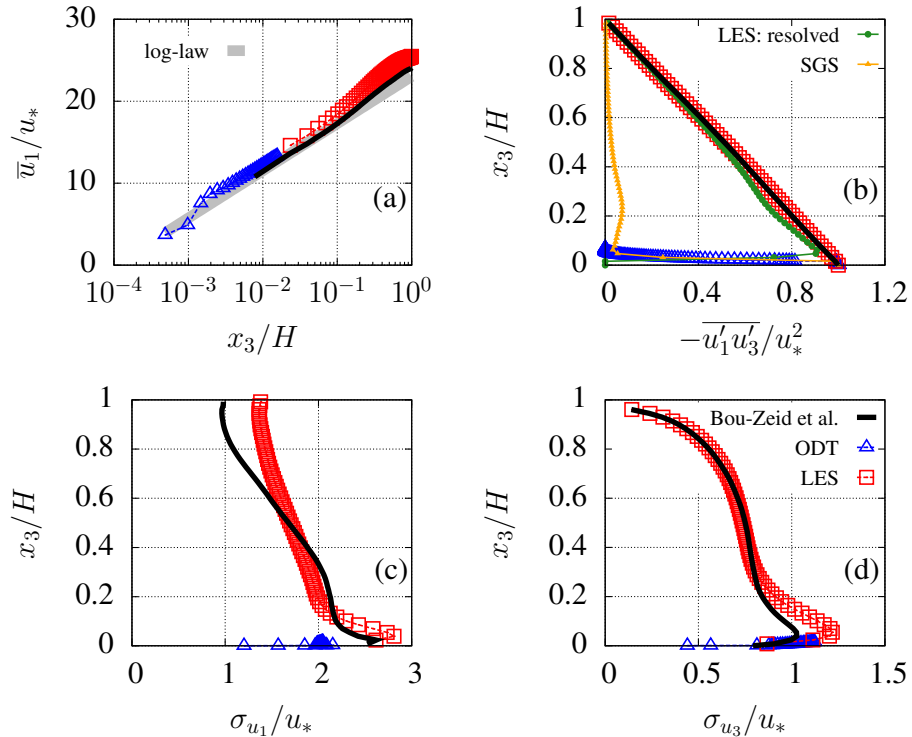


Figure 4.9. Statistics of the velocity field from rough channel simulation, corresponding to ODT (\hat{u}_i , blue) and LES (\tilde{U}_i , red). Results of (a) normalized mean streamwise velocity, (b) total shear, normalized standard deviation of (c) streamwise and (d) vertical velocity. Black lines corresponds to LES results from Bou-Zeid et al. (2005). (b) also presents the LES resolved (green) and subgrid-scale shear (yellow).

boundary condition when compared to the model that uses a theory for the mean flow to obtain a local boundary condition.

In the ODT domain (see Figure 4.10), the value of the mean streamwise velocity is close to the log-law, whereas the values of σ_{u_1} and σ_{u_3} are underestimated (as obtained in the smooth-channel simulations). Nevertheless, ODT is providing the correct mean velocity and momentum flux as boundary conditions to LES, in addition to improving the variances in the LES domain. This result motivates the use of ODT to represent plant canopies within the LES, which is presented and discussed next.

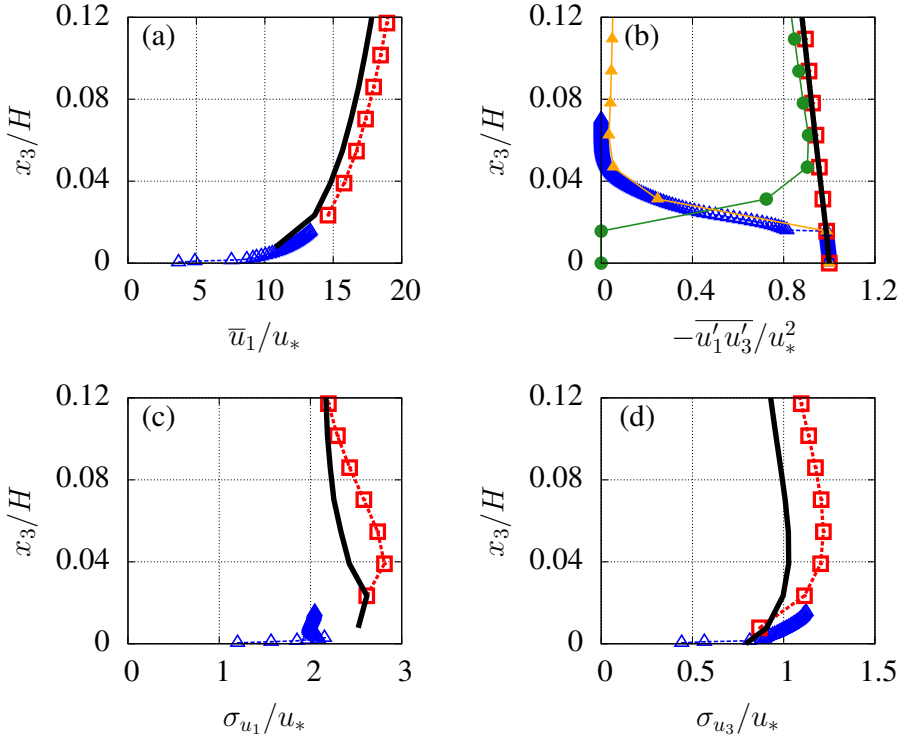


Figure 4.10. Same as Figure 4.9 but for $x_3/H \leq 0.12$.

4.4.3 Canopy flows

In Chapter 3, the stand alone version of the ODT model was used to simulate a flow through plant canopies up to the top of the ABL, and the parameter C_λ was adjusted in order to increase the match between model and data of mean streamwise velocity right above the canopy. This was achieved by reducing the value of C_λ (and consequently the mixing intensity) compared to rough-wall simulations, a choice consistent for all canopy flows tested. Conversely, in the ODT-LES model, the mean profile in the ODT domain is not as sensitive to changes in C_λ , as LES simulates the bulk of the ABL flow which drives the mean profile. In this case, the C_λ value is chosen in order to obtain the correct mean force balance (i.e., the correct value of u_* for the imposed mean pressure gradient force), and in all canopy simulations performed with ODT-LES this was achieved by keeping $C_\lambda = 20$ (the same value used for smooth- and rough-channel simulations). For the cornfield experiment, this choice resulted in a mean streamwise velocity just above the canopy smaller than the measured value (Figure 4.11a), as well as underestimation of standard

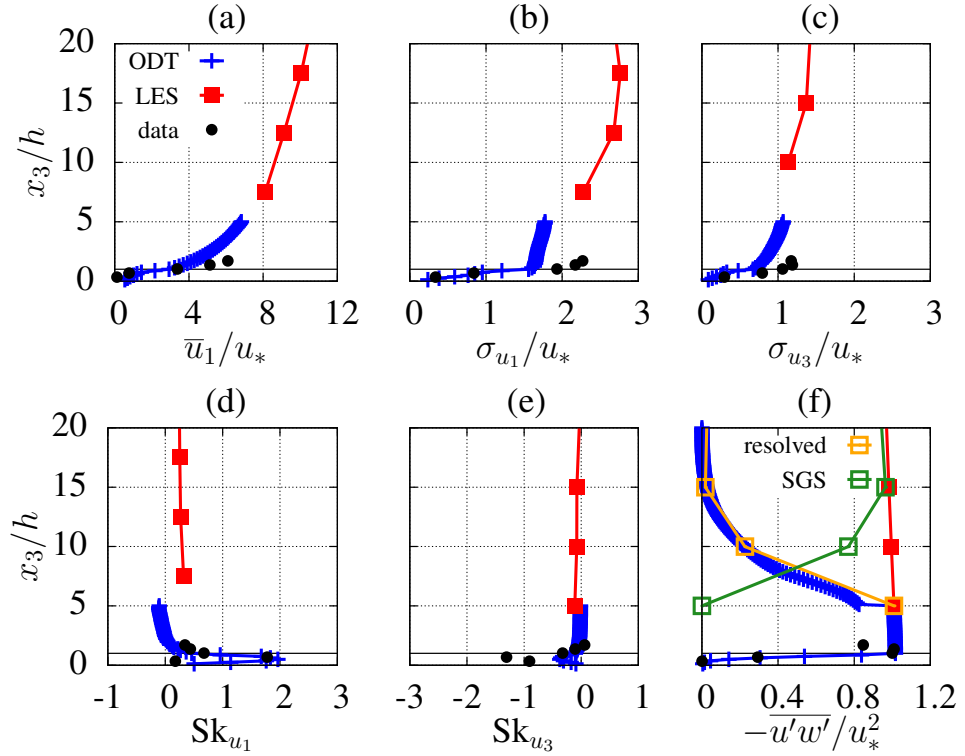


Figure 4.11. Corn simulation: ODT (blue) and LES (red) results of (a) normalized mean streamwise velocity, standard deviation of (b) streamwise and (c) vertical velocity, skewness of (d) streamwise and (e) vertical velocity and (f) vertical flux of streamwise velocity. Black dots correspond to field data presented by Pan et al. (2014). (f) also presents the LES resolved (green) and SGS (yellow) vertical flux of streamwise velocity.

deviations consistent to the smooth- and rough-channel cases (Figures 4.11b and c). Although measured data is not available in the surface layer above the canopy roughness layer (from $\sim 3h$ to $24h$), the results in the LES domain are as good as in the rough-wall case, as indicated by the values of σ_{u_1}/u_* close to 3 and σ_{u_3}/u_* close to 1.25.

Figure 4.12 shows a closer look at the ODT-LES results in the canopy roughness sublayer. Results from ODT stand alone from Chapter 3 and a canopy-resolving LES simulation from Pan et al. (2014) are also shown. Despite the problem in the mean streamwise velocity estimation, a significant improvement in the skewness of streamwise and vertical velocities is observed compared to the ODT-alone simulations, both results getting closer to the LES and experimental data values. The non-zero skewness in the canopy flow represents the development of non-Gaussian turbulence, resulting from the coherent structures present at the top

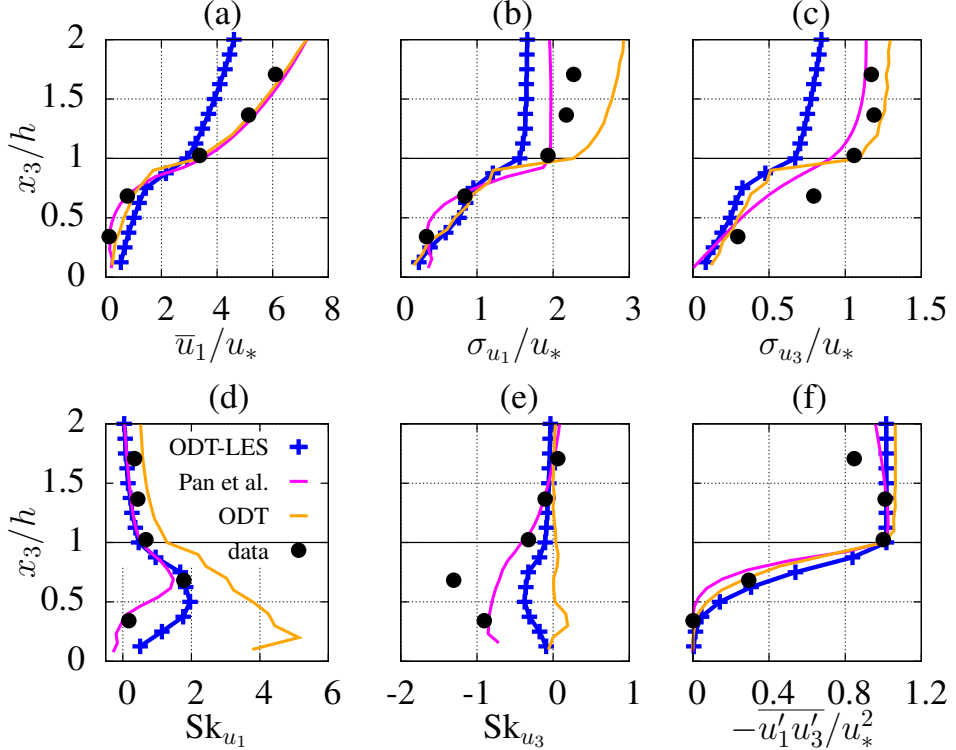


Figure 4.12. Same as Figure 4.11 for $0 < x_3/h < 2$. LES results obtained by Pan et al. (2014) (magenta) and ODT-alone results (yellow) are also shown .

of the canopy that create sweeps and ejections in the flow field within the canopy. These structures are driven by the strong shear in the streamwise velocity at the top of the canopy, which is well represented by the ODT model and is therefore captured by the streamwise skewness. But within the ODT alone, this streamwise skewness is not converted into vertical skewness, as the two velocity components are not connected (they behave as two independent scalar fields). Therefore, the negative skewness observed inside the canopy in the ODT-LES results can only be caused by the LES part of the coupling, which is itself influenced by the canopy-type turbulence represented by ODT. This is a good indicator that part of the complex canopy-type turbulence is being well represented by the two-way coupling between ODT and LES, which is encouraging despite the need to improve the first and second order statistics.

The simulation of the walnut orchard experiment resulted in similar normalized statistics compared to the cornfield simulation (see Figure 4.13). The consistent (although less pronounced) underestimation in the mean streamwise velocity above

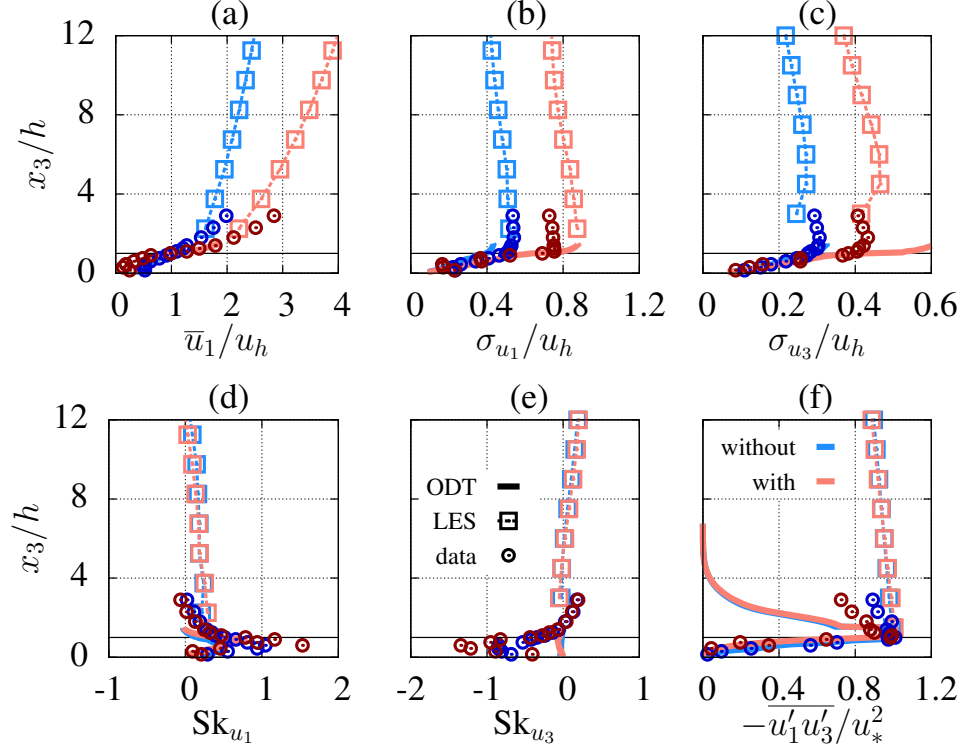


Figure 4.13. CHATS simulation: ODT (solid lines) and LES (squares) results of (a) normalized mean streamwise velocity, standard deviation of (b) streamwise and (c) vertical velocity, skewness of (d) streamwise and (e) vertical velocity and (f) vertical flux of streamwise velocity. Open dots correspond to field data presented by Dupont and Patton (2012) for neutral conditions. Results for no-leaves period (blue) and with-leaves period (red).

the canopy shows that there is room for improvement in the canopy-flow representation in the ODT-LES model (possibly by changes in the drag-force model). Compared to ODT-alone simulations, improvements can be observed in the mean streamwise profile, standard deviation profiles and in the skewness of the streamwise velocity (see Figures 4.14 and 4.15), enforcing the positive effect of the LES on the ODT results. The negative skewness of vertical velocity captured by ODT in cornfield case is not reproduced in the CHATS simulations, possibly because of the lower peak in streamwise skewness present in the walnut orchard ($\text{Sk}_{u_1} = 1$ and 1.5 compared to $\text{Sk} = 2$ in the cornfield case), which may be not enough to drive the transfer of information from ODT to LES and back to the vertical velocity in the ODT domain.

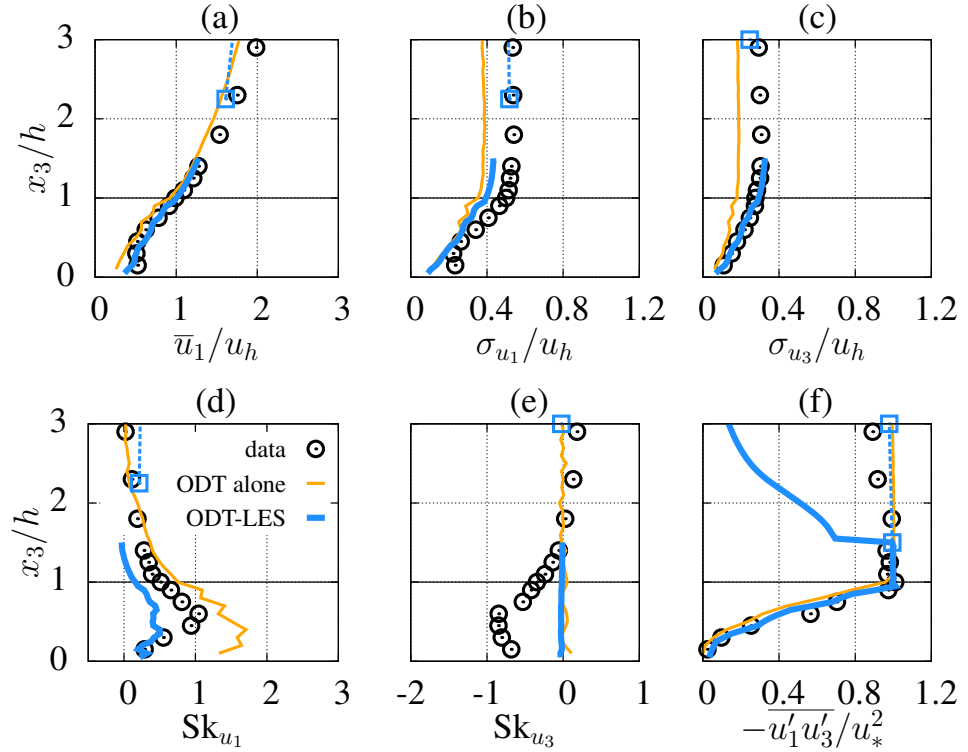


Figure 4.14. Same as Figure 4.13 but for $0 < x_3/h < 3$ and no-leaves case. ODT-alone results are shown in yellow.

4.4.4 Computational cost

As expected, the computational cost of using ODT as a wall model for LES is high compared to the wall model based on the law-of-the-wall. The two factors that contribute mostly to the cost increase are the number of ODT vertical grid points and the number of ODT timesteps within one LES timestep. The ODT computational cost is almost evenly shared between the calculation of the horizontal derivatives among ODT columns (which is done through Fast Fourier Transforms (FFTs) on each horizontal direction) and the evolution of the momentum equation, and both processes happen once every ODT timestep on each ODT grid point. The cost is also highly affected by the turbulence intensity in the ODT domain, because when probabilities of occurrence of stochastic eddies get too high, they are automatically reduced by reducing the ODT timestep. In this study, the rough-channel simulations are also used to compare the cost of ODT-LES with LES using the law-of-the-wall. Rough-channel simulations should be the most costly

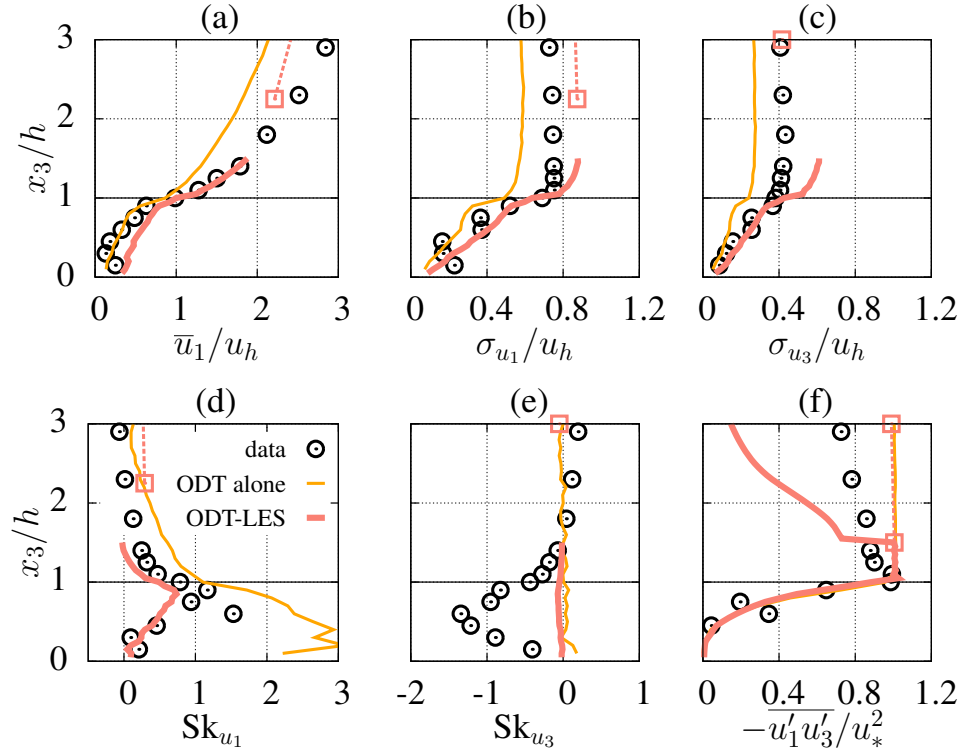


Figure 4.15. Same as Figure 4.14 but for with-leaves case.

case compared with smooth-channel and canopy-flow cases (for the same number of grids used in both ODT and LES domains), as the reduced flow in the ODT domain close to the surface in both smooth and canopy cases reduces the turbulence intensity. Figure 4.16a shows the comparison of CPU time for a LES simulations with N^3 grids ($n_x = n_y = n_z = N$), for $N = 32, 64$ and 128 . The computational cost was estimated as an average of 5 simulations, using 100 timesteps after the first 100, in a simulation ran in parallel using 8 processors. When the number of ODT grid points (n_{ODT}) is 32, ODT-LES is approximately 10 times more expensive than LES, a difference that doubles when n_{ODT} is multiplied by two. The increase in the computational cost of ODT-LES with the increase of N is very similar to the increase observed in LES alone, enforcing that most of the ODT cost is in the ODT vertical resolution and time-step.

The parallel processing in the LES code used here is done by dividing the vertical domain into layers, one for each processor used. Because ODT needs its entire vertical information to calculate the stochastic eddies, it cannot be sliced in the vertical as it is done in the LES. The alternative in this case is to divide

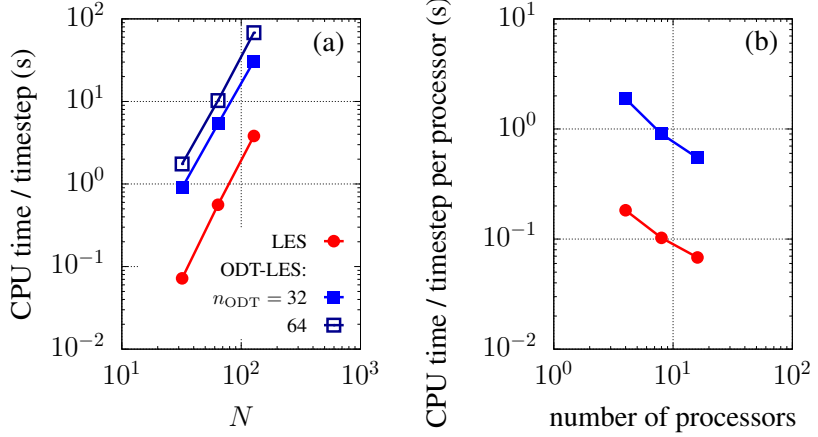


Figure 4.16. (a) CPU time per LES timestep as a function of number of LES grid points $N = n_x = n_y = n_z = 32, 64$ and 128 . (b) CPU time per LES timestep per processor as a function of number of processors used ($4, 8$ and 16), for $N = 64$. All results correspond to the rough-channel simulation using ODT-LES (blue) and LES (red).

the ODT domain horizontally, sending the calculations of a few ODT columns to each processor. Each ODT column is independent from each other except for the horizontal advection among ODTs. Therefore, all ODT processes can be done in parallel for different ODT columns, but during the FFT calculation for the horizontal advection term an exchange of information between processors is needed, which reduces the efficiency of the parallel process. Nevertheless, as shown in Figure 4.16b, the gain in CPU time observed in the ODT-LES through the increase of number of processors is similar to the gain observed in LES, giving confidence on the parallelization approach chosen to the ODT part of the model.

When using LES to represent surface processes within a large domain, the possibility of increasing the vertical resolution close to the surface is limited by the need to keep the grids' aspect ratio ($\Delta x_1/\Delta x_3$) in the order of ~ 4 to 6 , in order to be able to properly represent three dimensional turbulence. This means that any increase in vertical resolution requires a proportional increase in the resolution of the horizontal directions. As can be observed in Figure 4.16a, any increase in the LES resolution results in a very fast increase in computational cost. Therefore, for situations in which a high vertical resolution is needed close to the surface but the horizontal information does not need to be refined (as is the case of horizontally homogeneous canopies), the ODT-LES model may present the best cost-benefit relation compared to other LES wall approaches.

4.5 Conclusions

In this work, the use of the ODT as a wall model for LES was implemented to represent ABL flows in the presence of plant canopies. Two smooth-channel cases were tested and showed good agreement with DNS for mean streamwise velocity and total stress profiles, and underestimation of velocity standard deviations in the ODT domain. Compared to previous ODT-LES model, some differences in the standard deviation profiles were observed (improvement in the LES domain, deterioration in the ODT domain), likely due to different numerical approaches in the LES part of the model. Compared to previous LES wall parameterization (law-of-the-wall model), ODT-LES rough-wall results improved streamwise and vertical standard deviations close to the surface, likely due to the advantage of being a local parameterization, whereas the law-of-the-wall model is based on a theory for the mean flow. These results validated the two-way coupling and motivated the canopy-flow simulations.

In the three canopy-flow simulations tested here, the mean streamwise velocity right above the canopy was underestimated by the ODT-LES model. This indicates that current canopy representation through the drag force model needs to be improved. The profiles of standard deviation improved compared to ODT-alone simulation for the walnut orchard case, but they deteriorated in the corn case. Possibly the most interesting result was the improvement in the skewness profiles, compared to ODT-alone simulation in all cases tested. Since the ODT alone cannot correctly represent the vertical velocity skewness, and LES cannot develop canopy-type turbulence by itself without resolving the canopy, this result indicates that ODT is transferring the canopy-type streamwise flow information to LES, which is then transferring this information back to the vertical velocity component of ODT. This is a good example of the complex two-way coupling present in the ODT-LES model, which highly motivates future improvements on the canopy representation by ODT-LES.

In addition to the improvement of the LES-domain flow field, the advantage of using the ODT as a LES wall model is the instantaneous flow-field information available within the canopy region. Therefore, the next steps in the improvement of the ODT-LES model should include the incorporation of the temperature field to allow the simulation of different atmospheric stabilities, as well as other scalars,

gases with chemical reactions, particles, and any other atmospheric variables that are directly impacted by the presence of plant canopies. We believe that several atmospheric research fields could potentially benefit from this ABL-canopy simulation approach, such as dispersion and air-quality studies, cloud formation, carbon cycle, climate change, and many others.

The use of ODT as a wall superparameterization can also be extended to other near-surface complex flows, such as ocean waves, saltating sand and blowing snow. A similar approach could possibly be applied to mesoscale and global circulation models, in which ODT could be used to represent the vertical and time variation of the flow field, energy budget and scalars concentration within the ABL.

Chapter 5 |

Conclusions

Many atmospheric processes are affected by the presence of crops and forests, and they all depend to some extent on the intensity and structure of turbulent mixing within and above the canopy. Although the flow through plant canopies has been subject to intense study over the past fifty years, a number of open questions and modeling issues still remain. In this study we focused on two aspects of the problem, namely (i) the relative importance of turbulent mixing compared to other processes happening within the canopy, and (ii) a canopy-flow modeling approach that is capable of simulating non-local turbulent fluxes and transient conditions.

The characterization of turbulent mixing within the canopy was investigated for the specific case of ozone transport in the Amazon rainforest. The study used ozone concentration and high-frequency velocity data measured at several heights within the canopy and concluded that there is a direct relation between local turbulence intensity (here represented by the eddy diffusivity parameter) and the amount of ozone observed inside the canopy relative to the amount measured just above it. By classifying this relation in three regimes (poorly, partially and well-mixed conditions), the data showed that, during the day, the upper half of the canopy is well-mixed the vast majority of the time, whereas the lower half of the canopy is partially mixed half of the time. During the night, the upper half can be either poorly or partially mixed, whereas the lower half is almost always poorly mixed. This scenario describes the average conditions in which chemical reactions and deposition of ozone happen in the Amazon, which can be better quantified by comparing timescales. On average, turbulent mixing created well-mixed conditions in less than one hour during most of the daytime, but during the night its efficiency reduced significantly, reaching values between 3.5 and 6.5 hours in the lower region of the canopy. These numbers show that turbulence is mostly faster than chemistry

and deposition during the day, but during the nighttime the mixing timescale can be comparable to the chemistry timescale, meaning that turbulence can be a controlling factor of ozone concentration observed in the canopy at night. Data also showed that in the morning transition the change in turbulent mixing can be quite fast, creating a transient scenario that limits the use of equilibrium models and well-mixed assumptions when studying chemical reactions happening in the plants' environment during the first hours of the day. The mixing timescales estimated here can be used as a reference for comparison with other physical processes and chemical reactions happening within the Amazon rainforest. In addition, the new methodology applied here can be a useful tool for the estimation of mixing timescales in other types of canopy.

As exemplified by the case of the Amazon rainforest, turbulence in the canopy roughness sublayer varies significantly with height and time, a variability that needs to be taken into account when modeling atmospheric processes. Current low-cost models of canopy flows provide only equilibrium profiles of the flow statistics, and they are based on flux-gradient assumptions that neglect the dominant transport of non-local fluxes present in the canopy roughness sublayer. The ODT model is a useful tool for overcoming these issues, as it provides time-evolving instantaneous velocity and scalar fields, and it simulates turbulent fluxes through stochastic eddies driven by the kinetic and potential energy of the flow, therefore mimicking the effects of non-local transport. ODT was able to provide reasonable results for a wide range of ABL flows, including a diurnal cycle with different atmospheric stabilities. For neutral flows within the canopy, ODT reproduced the main characteristics of flow statistics up to the third order for four different types of canopy. All these results were obtained without case-specific adjustment of parameters or enforcement of boundary conditions. Some parameters present in the model (eddy probability distribution constant, Smagorinsky coefficient and drag coefficient) could be further optimized to better fit the experimental data, an option not tested here given that the goal of this study was to evaluate the general applicability of ODT. The addition of scalar fields in the model is straightforward, with almost negligible increase in computational cost and without the need of specific closures, adjustment of constants or boundary conditions. All of these characteristics make ODT a promising tool for a comprehensive modeling of ABL flows with canopy, including energy budget, chemical reactions and many other ABL processes.

Another important application of the ODT model is its use as a surface closure for large-scale models. In this study we tested this approach by applying ODT as a wall model for LES in cases where LES simulated the entire ABL and ODT represented the flow field within and above the canopy (not resolved by LES). The two-way coupling worked in a satisfactory way, which is remarkable given the stochastic versus deterministic nature of turbulence in the two models. This modeling approach opens a wide range of opportunities for the modeling of surface processes within a large-scale model. For example, in LES representing ABL flows, ODT could potentially be used to simulate the drift of particles at the surface (snow and sand, for example) and the presence of waves over lakes and ocean. Another possible application is the modeling of patches with different types of canopy. In addition, ODT can potentially be used as an ABL superparameterization for mesoscale and global circulation models, a case in which the separation of scales simplifies the two-way coupling between the models (compared to the LES case where there is a continuum of scales between the models). This vast range of applications motivates future work on testing and improving ODT for the representation of other processes, such as unstable and stable flows within the canopy, particle transport and chemical reactions.

The main contributions of this study to the current knowledge of turbulent flows in the canopy roughness sublayer can be listed as follows: (i) turbulent mixing within the canopy can vary significantly in space and time, creating conditions in which the mixing efficiency can be much faster or equally slow compared to other processes happening within the canopy, such as chemical reaction and deposition of scalars; and (ii) the ODT model is a suitable tool for single-column simulation of ABL flows with and without canopy, including the modeling of temperature and other scalar fields; it can also be used as a surface parameterization of canopy and ABL flows for large-scale models. In summary, this study calls attention to the fact that turbulence within the canopy needs to be properly evaluated and modeled, and it provides a promising tool for simulating atmospheric flows in the presence of plant canopies.

Appendix |

Flux-profile relationship for dust concentration in the stratified atmospheric surface layer

Dust ejected from soil surfaces by the wind is a major contributor to the aerosol concentration in the atmosphere, impacting climate and air quality from local to global scales. Soil dust can affect the climate directly by changing the net radiation, and indirectly by interfering with cloud formation and precipitation (Zhao et al., 2003). It can also serve as a catalytic reactor for gases in the atmosphere, modifying bio-geochemical processes in air and oceans (Ginoux et al., 2001). Dust is composed of solid inorganic particles of diameter $< 62.5 \mu\text{m}$, usually derived from sediment formed by weathering and erosion of rocks (Kok et al., 2012). Once dust particles are lifted from the surface, they are mainly transported in suspension. Consequently, the dust concentration in the atmosphere is strongly influenced by the particle gravitational settling and atmospheric turbulence (Tsoar and Pye, 1987). While gravitational settling limits the lifetime of dust in the air reducing transport distances (only particles smaller than $20 \mu\text{m}$ of diameter can remain suspended long enough to substantially affect weather and climate (Kok et al., 2012)), more vigorous turbulence produced by buoyancy can enhance this lifetime. Similarly, the deposition velocity of suspended particles can also be modulated by the effects of atmospheric stability on turbulence intensities. Therefore a theoretical framework that considers the effects of gravitational settling and atmospheric stability on dust fluxes is highly desirable.

The simplest approach for the development of such a theory is to seek steady-state relations between surface fluxes and mean vertical concentration profiles

over very large dust sources or sinks (hereafter “profile” will be used to refer to “vertical profile”). If available, this relation can be used to estimate atmospheric dust loads from surface fluxes as well as to estimate surface fluxes from observed mean concentrations. The latter is also relevant in the representation of surface fluxes of dust in numerical simulations. Turbulence resolving numerical simulations of the ABL focusing on particle dispersion usually parameterize the surface flux (both the source and the deposition) as a function of the resolved concentration at a reference height (Chamecki et al., 2009; Chamecki and Meneveau, 2011; Pan et al., 2013). In this application, a simple yet effective model that captures the effects of particle size and atmospheric stability on the flux-concentration relation is needed. During long-distance transport events relevant for regional air quality considerations and climate processes, dust particles $> 5 \mu\text{m}$ are predominantly removed from the atmosphere by dry deposition (Kok et al., 2012). Therefore, another application is the parameterization of dry deposition velocity in regional and global climate models (Zender et al., 2003; Gong et al., 2003; Ginoux et al., 2001; Nho-Kim et al., 2004).

The first theoretical equilibrium profile of mean particle concentration was proposed by Prandtl (1952), and it was derived based on the steady-state mean conservation equation for “heavy” particle concentration under the assumptions of zero surface net flux and neutral atmospheric stability. Chamberlain (1967) and Kind (1992) extended the model to non-zero surface fluxes. Chamecki et al. (2007) generalized the approach to include the effects of atmospheric stability, presenting comparisons with observed profiles of corn pollen concentration above a cornfield. The main limitation of the model presented by Chamecki et al. (2007) is that in the limit of very small particles (when the gravitational settling is negligible), the equation does not recover the classic result obtained from Monin-Obukhov similarity theory (Monin and Obukhov, 1954) for passive scalars. Thus, a unified framework that accounts for effects of atmospheric stability and is valid across the entire range of particle sizes is still lacking.

Another standing issue is the set of conditions required for the existence of equilibrium solutions. In particular, over very large sources for which mean horizontal advection is negligible, the existence of equilibrium solutions with non-zero net surface fluxes has been questioned (Hoppel et al., 2002). If a zero net flux is required, then Prandtl’s model is the only possible solution. However, an idealized

model study by Xiao and Taylor (2002) has shown that equilibrium solutions with non-zero net flux exist for small particles. Resolving this issue is extremely important, because if no equilibrium profile exists with a non-zero surface net flux, then these simple equilibrium models cannot be used to retrieve surface fluxes from mean concentration measurements nor to parameterize deposition fluxes in numerical models.

In this context, the objectives of the present study are the following: (i) to investigate the applicability of equilibrium solutions for dust concentration profiles over large sources and sinks; (ii) to develop a new analytical equilibrium model relating surface flux and profiles of mean dust concentration that accounts for effects of particle size and atmospheric stability with a non-zero net surface flux; and (iii) to assess the accuracy of different equilibrium solutions in retrieving surface fluxes from mean concentration profiles. Simulations of the dust transport in the ABL were performed using the Large-Eddy Simulation (LES) technique for neutral, unstable and stable thermal stabilities, with different particle sizes, with emission and deposition surface fluxes. Simulation results were used to evaluate the steady-state hypothesis and the performance of the various equilibrium models in reproducing mean profiles and estimating surface fluxes. Based on the results, the applicability of each equilibrium model is discussed.

The next section presents the description of existing equilibrium models for the mean concentration profile, followed by the derivation of a new model. Section A.2 describes the LES simulations performed in the present study. In Section A.3, the steady-state hypothesis is evaluated from the simulation data, and the performance of different equilibrium models is assessed. Conclusions are presented in Section A.4.

A.1 Models for the mean concentration dust profile

A.1.1 Existing models for mean concentration profile

The usual approach to relate flux and mean concentration profiles of dust introduced by Prandtl (1952) is based on the Reynolds-averaged conservation of mass of dust particles (hereafter assumed to be monodisperse). The equation for a horizontally

homogeneous flow with no mean vertical velocity is

$$\frac{\partial \bar{C}}{\partial t} = w_s \frac{\partial \bar{C}}{\partial z} - \frac{\partial}{\partial z} \bar{w'c'} + \frac{\partial}{\partial z} \left(D \frac{\partial \bar{C}}{\partial z} \right), \quad (\text{A.1})$$

where \bar{C} is the mean concentration of particles, $\bar{w'c'}$ is the vertical turbulent flux, z is height, t is time, w_s is the particle settling velocity (assumed to be constant), and D is the diffusivity due to Brownian motion. Note that the assumption of source or sink with a large extent is implicit in the fact that horizontal advection is neglected. Parameterizing the turbulent flux in terms of an eddy diffusivity K_C , neglecting Brownian diffusion, and assuming that the mean concentration is constant in time, vertical integration of Equation (A.1) yields

$$-K_C \frac{d\bar{C}}{dz} - w_s \bar{C} = \Phi. \quad (\text{A.2})$$

The first term on the left side of Equation (A.2) represents the turbulent flux of dust particles and the second term represents the flux due to gravitational settling. The constant of integration Φ represents the net vertical flux of dust (Kind, 1992; Chamecki et al., 2007). For the present problem, the source or sink is located at the ground and Φ can be interpreted as the net surface dust flux. Note that the assumptions leading to Equation (A.2) imply that the net flux must be constant in time and space.

Different models for the mean concentration profile of particles have been obtained from Equation (A.2), corresponding to different assumptions for K_C , Φ and w_s . Prandtl (1952) assumed that the transport of particles by turbulent diffusion is balanced by gravitational settling, resulting in a zero net flux (which corresponds to Equation (A.2) with $\Phi = 0$). Assuming the particle eddy diffusivity to be equal to the momentum diffusivity $K_C = \kappa z u_*$ (κ is von Karman's constant and u_* is the wind friction velocity), integration yields Prandtl's power-law model for the normalized vertical profile

$$\frac{\bar{C}}{\bar{C}_r} = \left(\frac{z}{z_r} \right)^{-w_s/\kappa u_*}, \quad (\text{A.3})$$

where \bar{C}_r is the mean concentration at a reference height z_r .

As pointed out by Kind (1992), the problem of using Equation (A.3) is that the

net flux Φ is in general not zero. Chamberlain (1967) and Kind (1992) proposed a more general model by integrating Equation (A.2) with a non-zero constant Φ :

$$\frac{\bar{C}}{C_r} = \left(\frac{\Phi}{\bar{C}_r w_s} + 1 \right) \left(\frac{z}{z_r} \right)^{-w_s/\kappa u_*} - \left(\frac{\Phi}{\bar{C}_r w_s} \right). \quad (\text{A.4})$$

In the limit of vanishing settling velocity ($w_s \rightarrow 0$), this model (hereafter referred to as Kind's models) tends to the log-law profile obtained from similarity theory for neutral stability conditions (Monin, 1970):

$$\frac{\bar{C}}{C_r} = 1 - \frac{\Phi}{\kappa u_* \bar{C}_r} \ln \left(\frac{z}{z_r} \right). \quad (\text{A.5})$$

The solution (A.4) also recovers Prandtl's model (A.3) when the net flux is zero ($\Phi = 0$). Therefore, Kind's model corresponds to a complete representation of \bar{C}/\bar{C}_r for different settling velocities and constant net fluxes.

Models (A.3)–(A.5) are valid for neutral stability, and their use is typically justified on the basis that aeolian transport only occurs at high wind speeds, and that neutral stratification is a good approximation under these conditions (Kind, 1992). However, significant transport may occur under unstable conditions (Chamecki et al., 2007; Klose and Shao, 2013). By analogy with Monin-Obukhov (MO) similarity theory, Chamecki et al. (2007) assumed that the dimensionless total vertical flux of particles, composed of turbulent and settling fluxes, is a function of the dimensionless stability parameter $\zeta = z/L$, where $L = -u_*^3 \bar{\theta}_s / (\kappa g \bar{w}' \bar{\theta}'|_s)$ is the Obukhov length ($\bar{\theta}_s$ and $\bar{w}' \bar{\theta}'|_s$ are the temperature and sensible heat flux at surface, respectively, and g is gravitational acceleration). Therefore, their assumption can be written as

$$\frac{1}{\Phi} \left(\frac{\kappa z u_*}{S c_t} \frac{d\bar{C}}{dz} + w_s \bar{C} \right) = -\phi_c(\zeta). \quad (\text{A.6})$$

For lack of a better alternative, they used the similarity function for passive scalars given by Kaimal and Finnigan (1994),

$$\phi_c(\zeta) = \begin{cases} (1 - 16\zeta)^{-1/2}, & \text{if } \zeta < 0 \text{ (unstable)}, \\ 1 + 5\zeta, & \text{if } \zeta > 0 \text{ (stable)}, \\ 1, & \text{if } \zeta = 0 \text{ (neutral)}. \end{cases} \quad (\text{A.7})$$

The solution of Equation (A.6) is

$$\frac{\bar{C}}{\bar{C}_r} = \left[\frac{\Phi}{\bar{C}_r w_s} \Omega \left(\frac{z_r}{L} \right) + 1 \right] \left(\frac{z}{z_r} \right)^{-\gamma} - \frac{\Phi}{\bar{C}_r w_s} \Omega \left(\frac{z}{L} \right), \quad (\text{A.8})$$

where $\gamma = w_s S c_t / (\kappa u_*)$ is the Rouse number and $S c_t = K_M / K_C$ is the turbulent Schmidt number, which accounts for differences between the eddy diffusivity of particles (K_C) and the eddy diffusivity of momentum (K_M). The atmospheric stability correction function is calculated via

$$\Omega(\zeta) = \begin{cases} {}_2F_1(\gamma, 1/2; 1 + \gamma; 16\zeta), & \text{if } \zeta < 0 \text{ (unstable),} \\ 1 + 5 \left(\frac{\gamma}{\gamma+1} \right) \zeta, & \text{if } \zeta > 0 \text{ (stable),} \\ 1, & \text{if } \zeta = 0 \text{ (neutral),} \end{cases} \quad (\text{A.9})$$

where ${}_2F_1(\gamma, 1/2; 1 + \gamma; 16\zeta)$ is the Gaussian hypergeometric function (Lebedev, 1972; Chamecki et al., 2007).

Equation (A.8) is a model for the concentration profile of dust as a function of the particle diameter (through the settling velocity w_s), the net flux Φ , and the atmospheric stability ζ . This model recovers Kind's model (A.4) with the inclusion of the turbulent Schmidt number $S c_t$ when the ABL is neutral (note that the limit works for both the stable and the unstable expressions, because in the latter ${}_2F_1 \rightarrow 1$ when $\zeta \rightarrow 0$). In the limit for very small particles ($w_s \rightarrow 0$), the model should recover the expression for MO similarity theory for a passive scalar. However, in this limit we have $\Omega(\zeta) \rightarrow 1$ for both the unstable and stable expressions in Equation (A.9) (note that ${}_2F_1 \rightarrow 1$ for $w_s \rightarrow 0$). Therefore the effects of atmospheric stability vanish for small particles and the model proposed by Chamecki et al. (2007) tends to Kind's model and not the expressions from MO similarity theory, suggesting that there is a problem with that solution. Note that Equation (A.6) approaches MO similarity theory for $S c_t = 1$ and $w_s \rightarrow 0$ (i.e. it recovers Equation (A.10) if one replaces $\Phi = -K_C d\bar{C}/dz$), and the problem arises during the integration leading to (A.8). Note also that Equation (A.6) is certainly not the most natural way to include effects of atmospheric stability (as discussed later) and that it cannot be recast in the general form (A.2).

A.1.2 A new general solution for mean concentration profile

A new solution to Equation (A.2) can be obtained by using a more general model for the turbulent diffusivity K_C . Following the standard approach from Monin-Obukhov similarity theory, the effect of atmospheric stability can be incorporated in the parameterization of the turbulent diffusivity (Kaimal and Finnigan, 1994; Shao, 2000)

$$K_C(\zeta) = \frac{\kappa z u_*}{\phi_c(\zeta)}. \quad (\text{A.10})$$

In addition, the trajectory-crossing effect (Csanady, 1963) on the turbulent diffusivity has to be taken into account. This is done by replacing K_C by $K_{C,p} = \alpha_{tc} K_C$, where α_{tc} represents a reduction in the turbulent diffusivity due to the trajectory-crossing effect. Following the model proposed by Csanady (1963), the correction for the vertical turbulent diffusivity is given by

$$\alpha_{tc} = \left(1 + \beta^2 \frac{w_s^2}{\sigma_w^2}\right)^{-1/2} = \left(1 + \beta^2 \frac{w_s^2}{u_*^2 \phi_w^2}\right)^{-1/2}. \quad (\text{A.11})$$

Here β is a coefficient of proportionality between Lagrangian and Eulerian integral timescales usually assumed to be between 1 and 2 (Shao, 2000), σ_w^2 is the vertical velocity variance, and $\phi_w(\zeta)$ is the M-O similarity function for σ_w/u_* . The dependence of α_{tc} on ζ is not strong (see empirical fits in Kaimal and Finnigan (1994)) and it complicates the obtention of a closed form solution to Equation (A.2). Therefore, in the present analysis, this dependence is neglected and the neutral stability value $\phi_w(\zeta)=1.25$ is used. Under these condition, integration of equation (A.2) yields

$$\frac{\bar{C}}{\bar{C}_r} = \left(\frac{\Phi}{\bar{C}_r w_s} + 1 \right) \left(\frac{z}{z_r} \right)^{-\gamma} \exp(\gamma \psi_c) - \left(\frac{\Phi}{\bar{C}_r w_s} \right), \quad (\text{A.12})$$

where $\gamma = w_s \alpha_{tc} / (\kappa u_*)$ and $\psi_c \equiv \int_{z_r/L}^{z/L} \frac{(1-\phi_c(x))}{x} dx$. The solution (A.12) is general and requires specification of $\phi_c(\zeta)$. If equations (A.7) are used, one obtains

$$\psi_c = \begin{cases} 2 \ln \left(\frac{1+(1-16z/L)^{1/2}}{1+(1-16z_r/L)^{1/2}} \right), & \text{if } \zeta < 0, \\ -5z/L + 5z_r/L, & \text{if } \zeta > 0, \\ 0, & \text{if } \zeta = 0. \end{cases} \quad (\text{A.13})$$

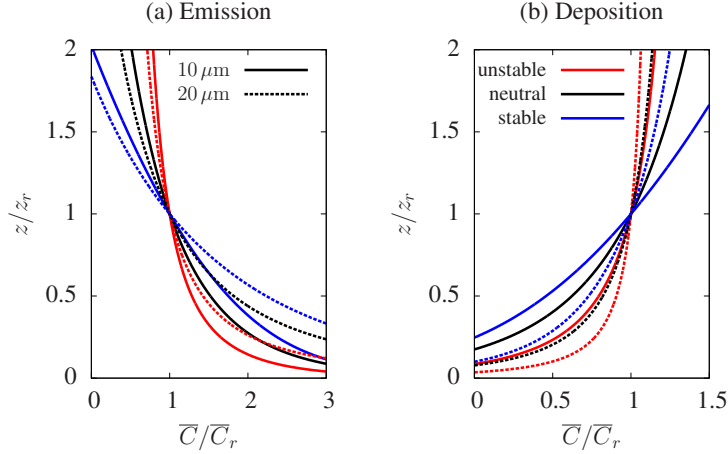


Figure A.1. Examples of profiles obtained from Equation (A.12) for particles with diameter $D_p = 10$ (solid lines) and $20 \mu\text{m}$ (dashed lines), with unstable ($L = -5 \text{ m}$, red), neutral (black) and stable ($L = 5 \text{ m}$, blue) ABLs. Arbitrary values of $u_* = 0.2 \text{ m s}^{-1}$, $\Phi/C_r = 0.05 \text{ m s}^{-1}$ (net emission) and $\Phi/C_r = -0.05 \text{ m s}^{-1}$ (net deposition) were used.

The final model for \bar{C}/\bar{C}_r (Equation (A.12)) is now complete and it has the correct limits. When the trajectory-crossing effect is neglected ($\alpha_{tc} = 1$) and $\zeta \rightarrow 0$, it recovers Kind's model (Equation (A.4)), and when $w_s \rightarrow 0$ it recovers the MO similarity theory for a passive scalar, which is given by

$$\frac{\bar{C}}{\bar{C}_r} = 1 - \frac{\Phi}{\kappa u_* \bar{C}_r} \left[\ln \left(\frac{z}{z_r} \right) - \psi_c \left(\frac{z}{L}, \frac{z_r}{L} \right) \right]. \quad (\text{A.14})$$

Figure A.1 illustrates some examples of Equation (A.12) for particles with diameter $D_p = 10$ and $20 \mu\text{m}$, for neutral, unstable ($L = -5 \text{ m}$) and stable ($L = 5 \text{ m}$) atmospheric stratifications over emitting ($\Phi > 0$) and depositing ($\Phi < 0$) surfaces. It is clear from the figure that both atmospheric stability and particle size have a strong effect on the shape of the mean concentration profiles.

The main difference between the proposed model and equation (A.8) presented by Chamecki et al. (2007) is the inclusion of the trajectory-crossing effects and the assumption that here only the turbulent flux is affected by atmospheric stability, while in equation (A.6) the settling flux is also modified by ζ . Although the changes introduced by buoyancy in the turbulence properties can potentially impact gravitational settling of inertial particles, in the present case the particle response time scale is so small that this effect is expected to be negligible.

A.2 Large-Eddy Simulation of dust concentration in the atmospheric boundary layer

The numerical simulations are designed to represent the evolution of dust profiles over an infinite and horizontally homogeneous dust source or sink. The LES code used in this study solves the three-dimensional filtered momentum equations in a rotating frame of reference, using a numerical discretization that combines a fully dealiased pseudo-spectral numerical method in the horizontal directions and a second order centered finite-differences method in the vertical direction. The fully explicit second-order Adams-Bashforth scheme is used for time integration. The scale-dependent Lagrangian averaged dynamic Smagorinsky model is used as sub-grid scale model, as described by (Bou-Zeid et al., 2005). The same numerical implementation used here has been shown to produce mean velocity and temperature gradients in the atmospheric surface layer agreement with M-O similarity theory for both unstable and stable stratifications (Kleissl et al., 2006). More details about the code can be obtained from the detailed description in Kumar et al. (2006).

The simulations are designed to represent the atmospheric boundary layer (ABL) driven by a mean constant pressure gradient in geostrophic balance above the ABL. The horizontal boundary conditions are periodic. A stressfree boundary condition is applied at the top of the domain, which is located above the temperature inversion that represents the top of the ABL. Momentum fluxes at the bottom of the domain are calculated using Monin-Obukhov similarity theory as described in Kumar et al. (2006).

Dust particles are simulated using a concentration field as described by Chamecki et al. (2009). A filtered advection-diffusion equation including an additional term to represent gravitational settling (with constant settling velocity in the vertical direction) is used. The equation is discretized using a finite-volume approach and advection is represented by the flux-limiting scheme SMART (Gaskell and Lau, 1988) (see also Chamecki et al. (2008) for more details). The constant settling velocity w_s is defined by the terminal settling velocity in a still fluid and it is calculated via Stokes' law for a spherical particle

$$w_s = \frac{D_p^2 \rho_p g}{18\mu}, \quad (\text{A.15})$$

where D_p and ρ_p are the diameter and density of the particle respectively, and μ is the dynamic viscosity of air.

A surface flux of dust Φ is imposed as a lower boundary condition over the entire horizontal domain. This flux represents the net flux at the surface, which should correspond to the imbalance between the emission and the deposition of particles. In the case of net emission of dust particles, a constant positive Φ was imposed. For the simulations representing a net deposition flux, Φ is obtained from the concentration in the first grid node, using Equation (A.4) (Kind's model), which can be justified by the assumption that the atmospheric stability effects very close to the surface are negligible. As can be observed from the results presented next, this assumption does not affect the influence of atmospheric stability on the mean concentration profile.

A.2.1 Summary of simulations

Two sets of simulations were performed. The first set, designed to study dust profiles above emitting dust sources, included neutral and unstable ABLs, for particles with $D_p = 1, 10, 20$ and $30 \mu\text{m}$ (with settling velocities $w_s = 7.98 \times 10^{-5}, 7.98 \times 10^{-3}, 3.19 \times 10^{-2}$ and $7.18 \times 10^{-2} \text{ m s}^{-1}$, respectively). The second set, designed to study dust deposition, included neutral, unstable and stable ABL for particles with $D_p = 1$ and $10 \mu\text{m}$. Table A.1 shows the physical domain and grid resolution of each stability case simulated. In all simulations, the domain was topped with a thermal inversion with a strength of 0.1 K m^{-1} (the strong inversion layer was intended to reduce the growth of the ABL in the convective simulations, allowing for appropriate statistical sampling under nearly steady-state conditions).

Table A.1. Simulations setup: domain and grid size.

	domain ($x \times y \times z$, m)	# of grid points	grid size (m)
neutral	$3000 \times 3000 \times 1000$	$160 \times 160 \times 320$	$18.75 \times 18.75 \times 3.125$
unstable	$3000 \times 3000 \times 1000$	$160 \times 160 \times 320$	$18.75 \times 18.75 \times 3.125$
stable	$480 \times 480 \times 160$	$160 \times 160 \times 320$	$1.5 \times 1.5 \times 0.5$

The main simulation parameters used for each case are presented in Table A.2. Note that there is a small difference between the initial ($z_{i,0}$) and final ($z_{i,f}$) values of the ABL height (except for the stable case). The value of $-z_i/L \approx 30$ in the

unstable simulations over a source is close to the lower limit of free convection, in order to evaluate how the models behave in this “extreme” situation. Because in this case in the surface layer $-z/L$ goes from 0 to approximately 3, the MO similarity theory is still expected to hold.

Table A.2. Simulation setup: physical parameters. $z_{i,0}$ and $z_{i,f}$ are the initial and final ABL heights respectively, (U_g, V_g) are the horizontal components of geostrophic wind, $\overline{w'\theta'}_0$ is the surface heat flux, u_* is the friction velocity and L is the Obukhov length. Emission (emi.) and deposition (dep.) cases.

	$z_{i,0}$ (m)	(U_g, V_g) (m s^{-1})	$\overline{w'\theta'}_0$ (K m s^{-1})	u_* (m s^{-1})	L (m)	$z_{i,f}$ (m)	z_i/L
neutral (emi./dep.)	570	(16, 0)	0	0.40	$-\infty$	570	0
unstable (emi.)	570	(10, 0)	0.24	0.40	-20	600	-30
unstable (dep.)	570	(10, 0)	0.05	0.35	-62	590	-9.5
stable (dep.)	120	(8, 0)	-0.01	0.15	24	90	3.75

All simulations were first run without dust particles for a period corresponding to ~ 3 h in the neutral simulations and ~ 1 h in the unstable and stable simulations, for turbulence to spin up and reach steady-state conditions. Then the dust concentration was initialized with zeroes in the emission case and with a constant value of $\overline{C}(z)/\overline{C}_r = 1$ in the entire ABL for the deposition case. The surface of the domain was flat with a roughness $z_0 = 0.001$ m, and the surface flux of dust was set equal to $0.2 \mu\text{g m}^{-2} \text{s}^{-1}$ for all emission simulations. As an example, Fig. A.2 shows snapshots of the particle concentration field in the emission case for neutral and unstable ABL, for particles $10 \mu\text{m}$ of diameter. The figure illustrates the differences in instantaneous concentration fields between the two cases (note the convective plumes generated in the unstable case, with large concentration in the updrafts and nearly clean downdrafts).

A.3 Results

A.3.1 The applicability of the steady-state assumption

An important assumption of the equilibrium models discussed here is that the mean concentration field is in steady state within the atmospheric surface layer (i.e., $\partial\overline{C}/\partial t$ can be neglected). If the unsteady term is not neglected, Equation (A.1)

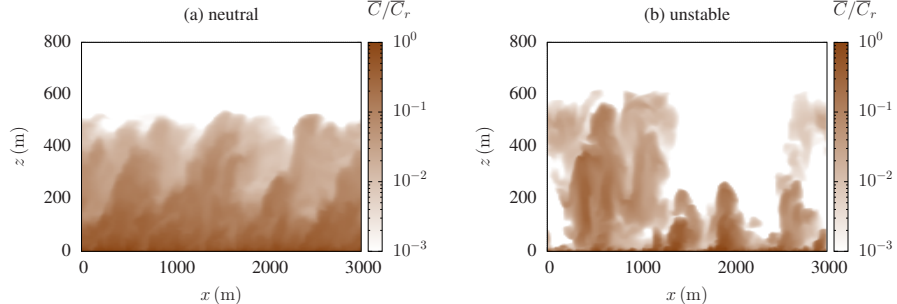


Figure A.2. Snapshots of normalized particle concentration field (\bar{C}/\bar{C}_r), for $D_p = 10 \mu\text{m}$, for emission simulations in (a) neutral and (b) unstable ABL.

can be integrated in the vertical direction to yield (once again neglecting Brownian diffusion)

$$\overline{w'c'} - w_s \bar{C} = \Phi - \int_{z_0}^z \frac{\partial \bar{C}}{\partial t} dz. \quad (\text{A.16})$$

In this equation, the left hand side corresponds to the total vertical dust flux. On the right hand side, Φ is the net surface flux and the second term must carry all the vertical and time dependence of the total flux. Over a source $\Phi > 0$ and we expect $\partial \bar{C} / \partial t > 0$, so that the unsteady term will be increasingly more negative as z increases. Thus, Equation (A.16) predicts that the total flux ($\overline{w'c'} - w_s \bar{C}$) should decrease with height (the opposite should happen in the case over a sink). All the solutions presented in Section A.1 rely on the assumption that the unsteady term is negligible in comparison with the dominant terms in equation (A.16), and that the total flux is approximately constant within the surface layer (as is assumed to be the case for scalar fluxes in the Monin-Obukhov similarity framework).

Because the steady-state assumption is not invoked in the LES runs, simulation results can be used to assess its applicability. Figure A.3 shows the time evolution of the ratio between the unsteady term of Equation (A.16) and the turbulent flux $\overline{w'c'}$ approximately in the middle of the surface layer (i.e., at $z = 0.05z_i$ – hereafter it is assumed that the surface layer extends up to $z = 0.1z_i$) for all simulations. In the figure, time is measured from the start of the dust initialization, and it is normalized by the eddy turnover time scale T_{eddy} for each simulation, which is given by $T_{\text{eddy}} = z_i/u_* \sim 1400 \text{ s}$ for neutral simulations, $T_{\text{eddy}} = z_i/w_* \sim 300 \text{ s}$ for unstable simulations (w_* is the convective velocity scale) and $T_{\text{eddy}} = z_i/u_* \sim 550 \text{ s}$ for stable simulations. In the beginning of the dust particle simulation, the unsteady term is

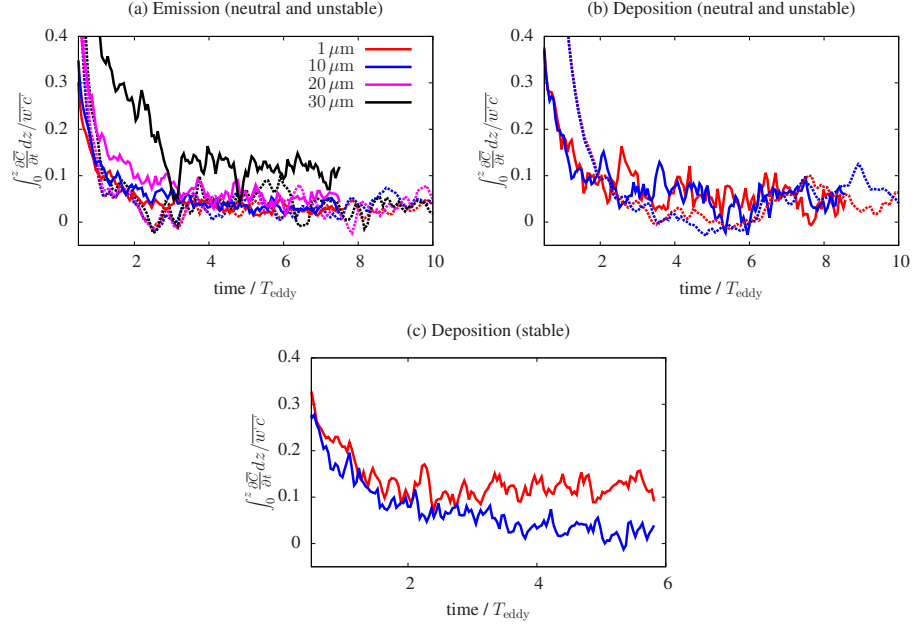


Figure A.3. Time evolution of the ratio between the unsteady term of Equation (A.16) and the turbulent flux, at $z/z_i \sim 0.05$, for all particle sizes. (a) Emission simulations, neutral ABL (solid lines) and unstable ABL (dashed lines). (b) Deposition simulations for neutral ABL (solid lines) and unstable ABL (dashed lines). (c) Deposition simulations for stable ABL. All times are normalized by the eddy turnover time scale for the ABL T_{eddy} .

dominant and the ratio is large due the spin-up time of the particle concentration field. After about one eddy turnover time, the ratio becomes approximately constant, at reasonably low values (typically smaller than 0.2 for neutral and stable simulations and much smaller than 0.1 for the unstable ones).

To provide further insight into the flux balance within the surface layer, Fig. A.4 shows time-averaged vertical profiles of each term of Equation (A.16), for particles with $D_p = 1$ and $30 \mu\text{m}$ for the emission case, and for particles with $D_p = 10 \mu\text{m}$ for the deposition case. For emission of small particles ($D_p = 1 \mu\text{m}$ in Fig. A.4a), the settling flux $w_s \bar{C}$ (blue) is negligible, and the turbulent flux $\bar{w}'c'$ (red) is approximately equal to the surface net flux Φ (magenta). The small difference is balanced by the unsteady term (black), which becomes larger with increasing height. This is true for neutral (solid lines) and unstable (dashed lines) temperature stratifications. For emission of large particles ($D_p = 30 \mu\text{m}$) in the neutral case (Fig. A.4b, solid lines) the turbulent flux (red) is mainly balanced by the settling

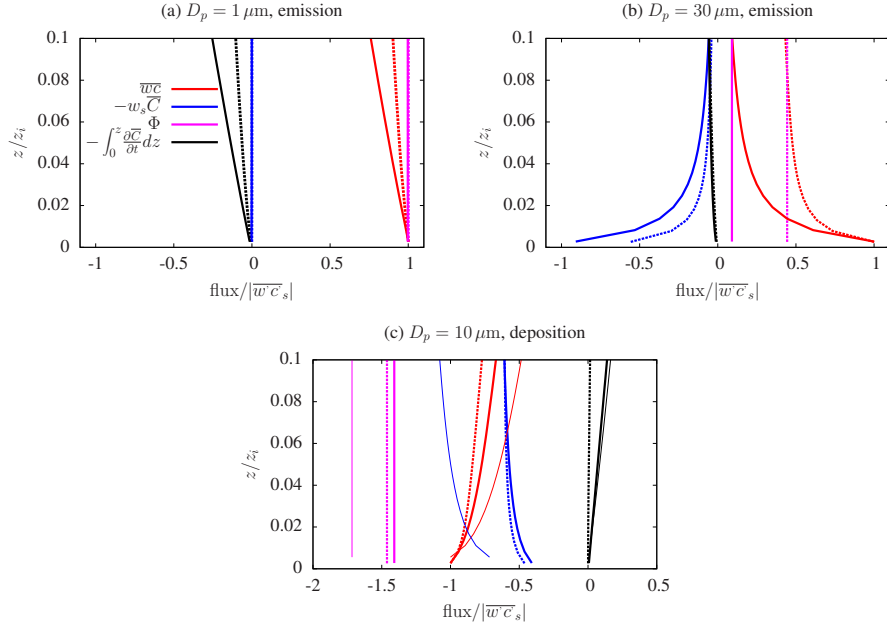


Figure A.4. Vertical profiles of each term of the unsteady flux equation (A.16) normalized by the absolute value of the turbulent flux at the surface ($|\bar{w}'\bar{C}'_s|$), for particles with (a) $D_p = 1 \mu\text{m}$ and (b) $D_p = 30 \mu\text{m}$ for emission simulations under neutral (solid lines) and unstable (dashed lines) ABL, (c) $D_p = 10 \mu\text{m}$ for deposition simulations under neutral (solid lines), unstable (dashed lines) and stable (thin lines) ABL.

flux (blue), and the surface net flux Φ (magenta) is small compared to those fluxes (suggesting that Prandtl's solution is a good approximation for these larger particles). In the unstable case (Fig. A.4b, dashed lines) turbulent flux (red) and gravitational settling (blue) are important, but so is their difference (i.e., the net flux is not negligible). In the deposition case (Fig. A.4c) the turbulent flux (red) and gravitational settling (blue) are important and balanced by the surface net deposition flux (magenta) for all atmospheric stabilities, with minor contribution from the unsteady term.

In general, Fig. A.4 suggests that in the surface layer ($z \lesssim 0.1z_i$), the unsteady term (black) is smaller than the other terms in Equation (A.16) for a range of particle sizes and atmospheric stabilities. Therefore, according to the present simulation results, the error incurred by neglecting the unsteady term (i.e. the equilibrium assumption) is acceptable. The worst case scenario is for a passive scalar ($w_s \rightarrow 0$) in neutral temperature stratification near the top of the surface layer, where the unsteady term reaches about 25% of the surface flux. The relative

importance of the unsteady term always increases with height, becoming significant above the surface layer. Therefore, even though the total loading of particles is evolving in time, the surface layer profile evolves in an approximate self-similar form that may be represented by equilibrium models.

It is often assumed that, over a source, the equilibrium state is only reached when the net surface flux is equal to zero ($\Phi = 0$), a condition that may require very long time periods to be reached (e.g., (Hoppel et al., 2002)). As can be observed from the results presented here, this hypothesis is not needed for the establishment of an approximate steady-state condition. Furthermore, for very small particles the surface emission flux is in equilibrium with the turbulent flux, which corresponds to the MO similarity theory for scalars. Therefore, the only necessary conditions for the approximate validity of the steady-state assumption in the mean concentration (besides the constant surface flux) are the (1) statistical steady-state turbulence and (2) horizontally homogeneity of surface forcings. These are the same conditions required by MO similarity theory.

A.3.2 The estimation of mean vertical concentration profiles of dust

When comparing the theoretical equilibrium models (Equations (A.3), (A.4), (A.5), (A.8), (A.12) and (A.14)) with simulation results, the parameters needed in the models, such as u_* , L and Φ , were obtained from the corresponding simulation. In all the analysis, the trajectory-crossing effect has been neglected by setting $\alpha_{tc} = 1$. The lowest value of α_{tc} estimated from Equation (A.11) for the simulations presented here is $\alpha_{tc} \approx 0.99$, corresponding to the largest particle $D_p = 30 \mu\text{m}$ in the convective simulation with $u_* = 0.35 \text{ m s}^{-1}$ (using the typical value $\beta = 1$). This is in agreement with Shao (2000), who concluded that for small dust particles the trajectory-crossing effect is only important in conditions with very weak turbulence. In addition, due to the different numerical approaches used for representing vertical advection in the momentum and particle concentration equations, a turbulent Schmidt number $Sc_t = 1.25$ is introduced in the theoretical profiles for comparisons with all simulations (this is equivalent to dividing $\phi_c(\zeta)$ by 1.25). This value corresponds to the ratio between eddy viscosity and particle eddy diffusivity for the simulations in the lower half of the surface layer ($z \lesssim 0.05 z_i$), where Sc_t

is approximately constant (this value is the appropriate Schmidt number for our simulations and it is not related to the trajectory-crossing effect, as it is independent of settling velocity). \bar{C}_r is taken at the first vertical grid point ($z_r = 1.56 \text{ m}$), and the results presented next are obtained by averaging the resolved concentration field in time and space (spatial averages are carried over the entire horizontal domain and time averages are carried over the last eddy turnover time of each simulation).

Figure A.5 shows the normalized mean concentration profiles of dust in the neutral surface layer for the emission cases. It is clearly seen in the figure that, for the neutral surface layer, Kind's model (Equation (A.4)) is a good approximation for the entire range of particle sizes investigated (from 1 to $30 \mu\text{m}$). The log-law model (Equation (A.5)) is indistinguishable from Kind's model for very small particles, here represented by $D_p = 1 \mu\text{m}$. Prandtl's power-law (Equation (A.3)) is a good approximation only for the largest particle size $D_p = 30 \mu\text{m}$. This suggests that for very large particles (which is the application intended by Prandtl, who was interested in profiles of blown snow and sand and sediment transport in rivers), the net flux is negligible when compared with settling and turbulent fluxes, as noted by Xiao and Taylor (2002) and clearly illustrated in Fig. A.4b. For intermediate particle sizes particles ($D_p = 10 \mu\text{m}$ and $20 \mu\text{m}$), for which both w_s and Φ are important, only Kind's equation provides a good model to the mean concentration profiles. Note that the difference between the other models (log-law and power-law) and the simulation results for intermediate particle sizes increases with height.

Figure A.6 is the unstable surface layer counterpart of Fig. A.5. It is clearly seen in the figure that Kind's model (Equation (A.4)) is always far from the simulation results, showing the importance of atmospheric stability in determining the mean particle concentration profile for the conditions in the simulation ($u_* = 0.40 \text{ m s}^{-1}$ and $L = -20 \text{ m}$). Therefore, the most meaningful comparison is between the three models that include stability corrections: MO similarity for a passive scalar (A.14), the model proposed by Chamecki et al. (2007) (A.8), and the new model proposed here (A.12). The agreement between the model proposed here and the LES results is very good. The other models display poor performance for large particles ($D_p = 20$ and $30 \mu\text{m}$). As expected, the differences between the new model and the passive scalar behavior decrease as the particle size decrease, and the two are again indistinguishable for the smallest particle size ($D_p = 1 \mu\text{m}$). Note how the model proposed by Chamecki et al. (2007) moves towards the new model and

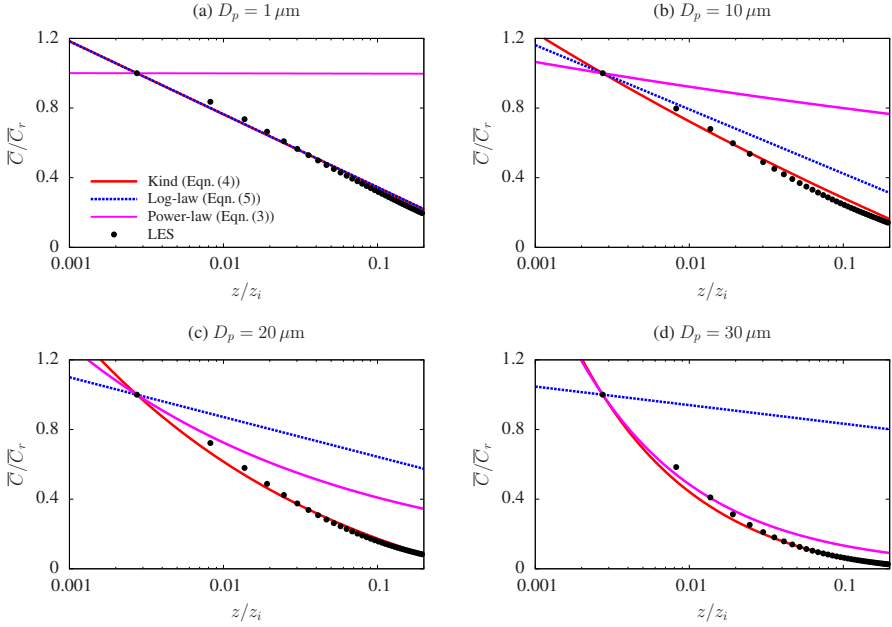


Figure A.5. Normalized mean vertical concentration profiles of dust in the neutral surface layer for different particle diameters ($1, 10, 20$ and $30 \mu\text{m}$, as indicated in the figure).

the passive scalar as particle size decrease from $D_p = 30$ to 20 and to $10 \mu\text{m}$, but it diverges from them for $D_p = 1 \mu\text{m}$ (moving toward Kind's profile as discussed in Section A.1).

Results obtained for the deposition simulations are presented in Fig. A.7, for all atmospheric stabilities and for particles with $D_p = 1$ and $10 \mu\text{m}$. As observed before, for $D_p = 1 \mu\text{m}$ the proposed model (or Kind's model in the neutral case) is equivalent to MO similarity model, but the later is very far from the simulation for larger particles (especially in the stable case). Although the use of Kind's model in unstable and stable conditions is not ideal, the error is not as large as in the emission case.

Comparisons similar to the one presented in Fig. A.6 were performed for other combinations of u_* and L ($u_* = 0.23$ and 0.34 m s^{-1} , $L = -28$ and -54 m), yielding the same conclusion. These results show that the model proposed in Section A.1.2 is capable of predicting the mean particle concentration profile for a wide range of stability and particle sizes, for emission and deposition cases.

As mentioned in previous subsection, after the first eddy turnover time the steady-state approximation is reasonable within the atmospheric surface layer.

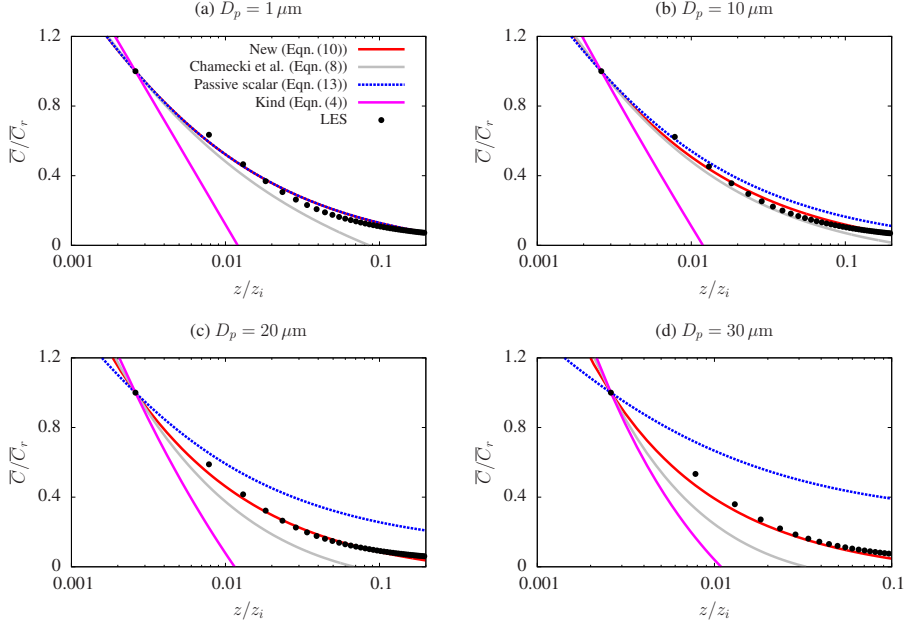


Figure A.6. Normalized mean vertical concentration profiles of dust in the unstable surface layer for different particle diameters ($1, 10, 20$ and $30 \mu\text{m}$, as indicated in the figure).

Because \bar{C}_r evolves during the simulation, one approach to verify the validity of the equilibrium solution in time is to look at the simulation trajectory on the parameters space spanned by \bar{C}/\bar{C}_r and $\Phi/\bar{C}_r w_s$. Trajectories from three heights within the surface layer are compared to those given by the equilibrium solution (A.12) in Fig. A.8. For all simulations performed (only those for $D_p = 10 \mu\text{m}$ are shown), the trajectories approach the model during the initial stages (about one eddy turnover time) and then remain close to the predicted trajectory for the duration of the simulations, confirming the picture of a time evolving self-similar profile.

A.3.3 Surface flux estimations from concentration data

In this section we study the inverse problem: the estimation of the surface flux from mean concentration profiles. The goal is to assess the capabilities of the different equilibrium models in recovering the flux used to force the LES (i.e., the true surface flux in the simulation). In this analysis, mean concentration values at the first seven vertical grid points of the simulation are employed (this corresponds approximately

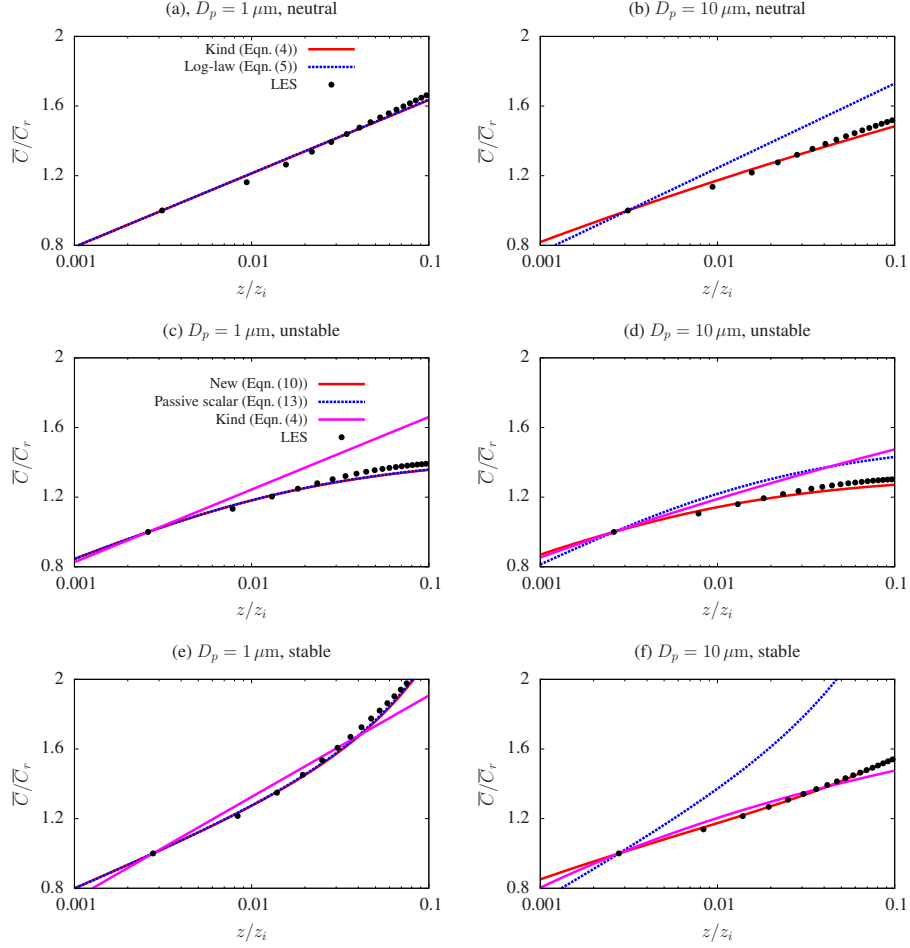


Figure A.7. Normalized mean vertical concentration profiles of dust in the deposition case for different particle diameters (1 and $10\ \mu\text{m}$) and atmospheric stability, as indicated in the figure.

to the lowest half of the surface layer; if additional points are used no significant differences are observed). Each model is fitted to the profile obtained from the simulations by estimating one single parameter: the value of the surface flux Φ . Figures A.9a and c present the results for neutral simulations in the emission and deposition cases, respectively, where surface fluxes are normalized by $\bar{C}_r u_*$ (this makes all fluxes of the same order of magnitude). It is evident that Kind's model (Equation (A.4)) yields a very good estimate of the flux for all particle sizes. As expected from the results in the previous discussions, the log-law model produces accurate estimates for very small particles ($D_p = 1\ \mu\text{m}$), but it diverges quickly overestimating the magnitude of true flux when particles increase in size. It is

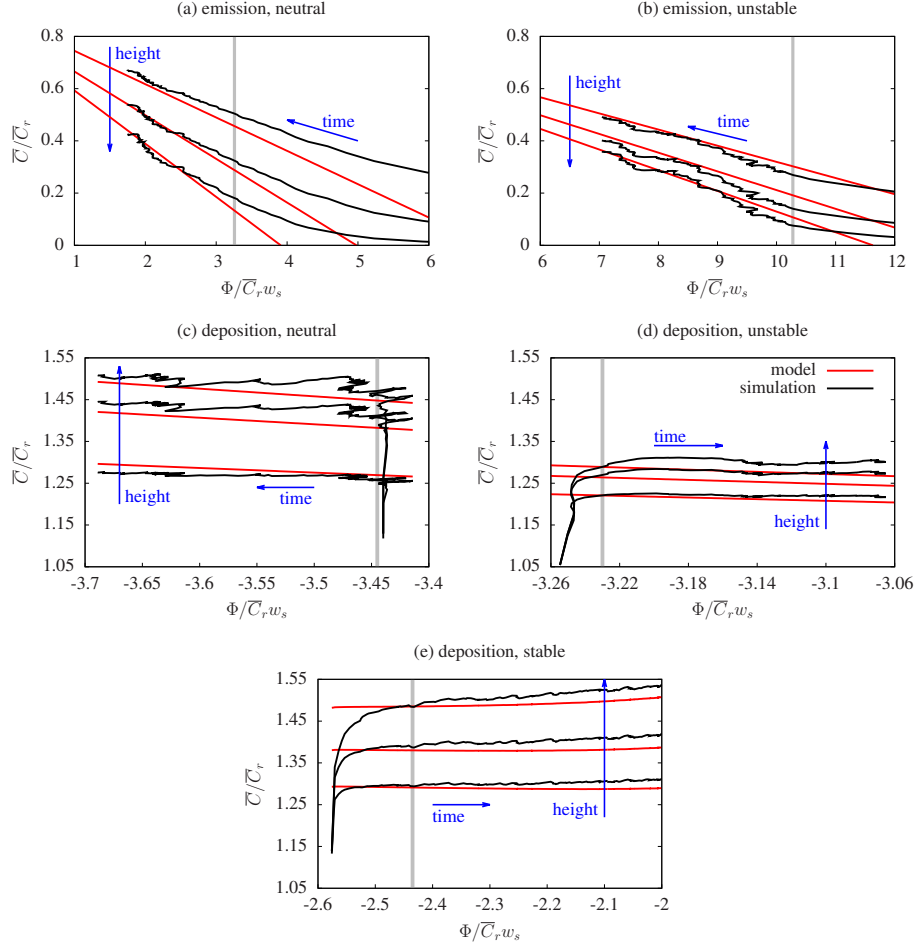


Figure A.8. Simulation trajectories on the parameters space spanned by \bar{C}/\bar{C}_r and $\Phi/\bar{C}_r w_s$ (simulation time evolution, black line) for $D_p = 10, \mu\text{m}$ at three different heights ($z = 0.02, 0.05$ and $0.09 z_i$). The red line corresponds to the trajectory of the proposed equilibrium model (Equation A.12). The vertical gray line identifies the time equal to one eddy turnover time ($t/T_{\text{eddy}} = 1$).

worthwhile mentioning that both equations fit equally well to the simulated profile, but as illustrated in Fig. A.9 yield very different estimates of the the surface flux.

The same analysis is performed for the unstable and stable atmospheric stratification cases, and the results are presented in Fig.s A.9b, d and e. As expected from the previous section results, neglecting atmospheric stability and using Kind's model provides very poor estimates of the surface fluxes (underestimation for unstable with emission and stable with deposition, and overestimation for unstable with deposition). All the models that include stability corrections perform equally

well for the smallest particle size, but only the newly proposed model yields good predictions of the surface flux across the range of particle sizes. Using MO similarity theory for passive scalars causes large over predictions of the fluxes, while the model proposed by Chamecki et al. (2007) produces under-prediction of the surface fluxes.

A.4 Conclusions

In this work a new equilibrium model relating surface flux and mean vertical profiles of dust concentration is proposed. The new model accounts for the effects of atmospheric stability (as characterized by $\zeta = z/L$) and particle settling velocity (w_s/u_*), and it recovers more specific models existent in the literature if the appropriate limits are used. It reduces to: (i) Kind's model (Chamberlain, 1967; Kind, 1992) for neutral stability, (ii) Prandtl's model (Prandtl, 1952) for neutral stability in the absence of a net flux of particles, (iii) the log-law (Monin, 1970) for neutral stability and no settling velocity, and (iv) MO similarity (Monin and Obukhov, 1954) for non-neutral stability and no settling velocity. In that sense, the resulting equation can be considered as an extension of Monin-Obukhov Similarity to concentration of settling particles.

Due to the difficulty in measuring surface fluxes of loose particles and the large variation in particle sizes during dust events, experimental validation of these models is difficult. The approach of fitting the value of the surface flux and comparing models by the mean squared errors of the adjusted equations (Gillies and Berkofsky, 2004; Chamecki et al., 2007) does not yield conclusive results. In this study we used numerical experiments based on LES of dust particles with four different sizes ($D_p = 1, 10, 20$ and $30 \mu\text{m}$) in neutral and unstable atmospheric stabilities with emission and deposition situations to verify the applicability of the various models.

For the neutral atmospheric stability case, results presented here are the most convincing evidence to date that Kind's model is indeed the best approach to represent equilibrium profiles of suspended particles above extensive sources. The simulations also show that, in addition to the obvious limit towards the log-law as w_s/u_* becomes very small, the assumption of $\Phi = 0$ is indeed good when w_s/u_* is large (as already suggested by the one-dimensional simulations of Xiao and Taylor (2002)).

For unstable and stable atmospheric conditions the new model proposed here

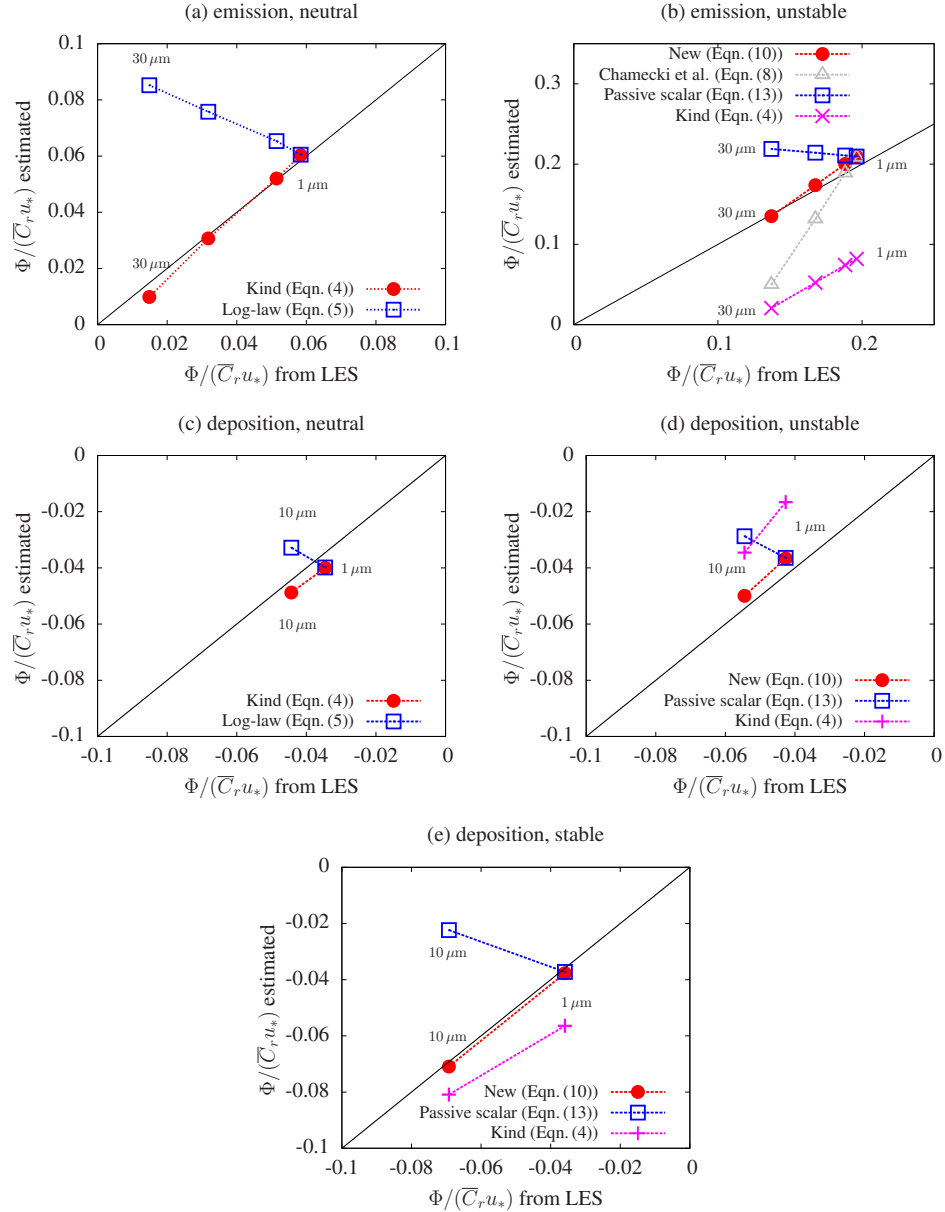


Figure A.9. Comparison between surface flux used to drive LES and the surface flux estimated by fitting theoretical profiles to mean concentration profile of the atmospheric surface layer. (a) Emission in neutral ABL, (b) emission in unstable ABL, (c) deposition in neutral ABL, (d) deposition in unstable ABL, and (d) deposition in stable ABL.

is in very good agreement with numerical simulations, performing much better than the model proposed by Chamecki et al. (2007). For the conditions used in the numerical simulations, effects of atmospheric stability on dust concentration profiles seem more important than gravitational settling. However, the picture would be different for lower values of the friction velocity. Therefore, we conclude that both effects are important and should be included in models that aspire to be applicable to realistic conditions.

Results also show that the steady-state assumption needed in the derivation of all the equilibrium models discussed here is reasonable for the atmospheric surface layer after the first eddy turnover time. Therefore, equilibrium models can be useful in the formulation of parameterizations for deposition fluxes typically needed in regional and global models.

Typically when the application requires estimating the surface flux from adjusting the concentration profiles to observations (Gillies and Berkofsky, 2004; Chamecki et al., 2007), different models present a similar performance measured by mean squared errors. However, the fitted values of the surface flux can be significantly different. This result is supported by the present study. In particular, the use of LES results where the surface flux is known clearly illustrates the poor predictions yielded by models that do not account for gravitational settling or atmospheric stability.

Bibliography

- Albertson, J. D., Katul, G. G., and Wiberg, P. (2001). Relative importance of local and regional controls on coupled water, carbon, and energy fluxes. *Advances in Water Resources*, 24:1103 – 1118.
- Alves, E. G., Jardine, K., Tota, J., Jardine, A., Yáñez Serrano, A. M., Karl, T., Tavares, J., Nelson, B., Gu, D., Stavrakou, T., Martin, S., Artaxo, P., Manzi, A., and Guenther, A. (2016). Seasonality of isoprenoid emissions from a primary rainforest in central amazonia. *Atmospheric Chemistry and Physics*, 16(6):3903–3925.
- Andren, A., Brown, A. R., Mason, P. J., Graf, J., Schumann, U., Moeng, C.-H., and Nieuwstadt, F. T. M. (1994). Large-eddy simulation of a neutrally stratified boundary layer: A comparison of four computer codes. *Quarterly Journal of the Royal Meteorological Society*, 120(520):1457–1484.
- Anfossi, D., Rizza, U., Mangia, C., Degrazia, G., and Filho, E. P. M. (2006). Estimation of the ratio between the lagrangian and eulerian time scales in an atmospheric boundary layer generated by large eddy simulation. *Atmospheric Environment*, 40(2):326 – 337.
- Angell, J. K., Pack, D. H., Hoegker, W. H., and Delver, N. (1971). Lagrangian-eulerian time-scale ratios estimated from constant volume balloon flights past a tall tower. *Quarterly Journal of the Royal Meteorological Society*, 97(411):87–92.
- Aschmann, S. M., Arey, J., and Atkinson, R. (2002). OH radical formation from the gas-phase reactions of O₃ with a series of terpenes. *Atmospheric Environment*, 36(27):4347 – 4355.
- Atkinson, R. (1997). Gas-phase tropospheric chemistry of volatile organic compounds: 1. alkanes and alkenes. *Journal of Physical and Chemical Reference Data*, 26(2):215–290.
- Atkinson, R., Baulch, D. L., Cox, R. A., Hampson, R. F., Kerr, J. A., Rossi, M. J., and Troe, J. (1999). Evaluated kinetic and photochemical data for atmospheric chemistry, organic species: Supplement vii. *Journal of Physical and Chemical Reference Data*, 28(2):191–393.

- Aylor, D. E. and Flesch, T. K. (2001). Estimating spore release rates using a lagrangian stochastic simulation model. *Journal of Applied Meteorology*, 40(7):1196–1208.
- Baldocchi, D. (1992). A lagrangian random-walk model for simulating water vapor, CO₂ and sensible heat flux densities and scalar profiles over and within a soybean canopy. *Boundary-Layer Meteorology*, 61(1):113–144.
- Batchelor, G. K. (2000). *An Introduction to Fluid Dynamics*. Cambridge University Press, Cambridge.
- Bou-Zeid, E., Meneveau, C., and Parlange, M. (2005). A scale-dependent lagrangian dynamic model for large eddy simulation of complex turbulent flows. *Physics of Fluids*, 17(2):025105.
- Brasseur, J. G. and Wei, T. (2010). Designing large-eddy simulation of the turbulent boundary layer to capture law-of-the-wall scaling. *Physics of Fluids*, 22(2):021303.
- Brunet, Y., Finnigan, J., and Raupach, M. (1994). A wind tunnel study of air flow in waving wheat: Single-point velocity statistics. *Boundary-Layer Meteorology*, 70(1-2):95–132.
- Bryan, A. M., Bertman, S. B., Carroll, M. A., Dusander, S., Edwards, G. D., Forkel, R., Griffith, S., Guenther, A. B., Hansen, R. F., Helmig, D., Jobson, B. T., Keutsch, F. N., Lefer, B. L., Pressley, S. N., Shepson, P. B., Stevens, P. S., and Steiner, A. L. (2012). In-canopy gas-phase chemistry during cabinex 2009: sensitivity of a 1-d canopy model to vertical mixing and isoprene chemistry. *Atmospheric Chemistry and Physics*, 12(18):8829–8849.
- Campos, J. G., Acevedo, O. C., Tota, J., and Manzi, A. O. (2009). On the temporal scale of the turbulent exchange of carbon dioxide and energy above a tropical rain forest in amazonia. *Journal of Geophysical Research: Atmospheres*, 114(D8):n/a–n/a. D08124.
- Cancelli, D. M., Chamecki, M., and Dias, N. L. (2014). A large-eddy simulation study of scalar dissimilarity in the convective atmospheric boundary layer. *Journal of the Atmospheric Sciences*, 71(1):3–15.
- Cassiani, M., Radicchi, A., and Albertson, J. (2007). Modelling of concentration fluctuations in canopy turbulence. *Boundary-Layer Meteorology*, 122(3):655–681.
- Chamberlain, A. C. (1967). Transport of lycopodium spores and other small particles to rough surfaces. *Proceedings of the Royal Society of London. Series A. Mathematical and Physical Sciences*, 296(1444):45–70.

- Chamecki, M. (2013). Persistence of velocity fluctuations in non-gaussian turbulence within and above plant canopies. *Physics of Fluids*, 25(11):1–14.
- Chamecki, M., Hout, R., Meneveau, C., and Parlange, M. (2007). Concentration profiles of particles settling in the neutral and stratified atmospheric boundary layer. *Boundary-Layer Meteorology*, 125(1):25–38.
- Chamecki, M. and Meneveau, C. (2011). Particle boundary layer above and downstream of an area source: scaling, simulations, and pollen transport. *Journal of Fluid Mechanics*, 683:1–26.
- Chamecki, M., Meneveau, C., and Parlange, M. (2008). A hybrid spectral/finite-volume algorithm for large-eddy simulation of scalars in the atmospheric boundary layer. *Boundary-Layer Meteorology*, 128(3):473–484.
- Chamecki, M., Meneveau, C., and Parlange, M. B. (2009). Large eddy simulation of pollen transport in the atmospheric boundary layer. *Journal of Aerosol Science*, 40(3):241–255.
- Cionco, R. M. (1978). Analysis of canopy index values for various canopy densities. *Boundary-Layer Meteorology*, 15(1):81–93.
- Coppin, P., Raupach, M., and Legg, B. (1986). Experiments on scalar dispersion within a model plant canopy part ii: An elevated plane source. *Boundary-Layer Meteorology*, 35(1-2):167–191.
- Corrsin, S. (1963). Estimates of the relations between eulerian and lagrangian scales in large reynolds number turbulence. *Journal of the Atmospheric Sciences*, 20(2):115–119.
- Corrsin, S. (1975). Limitations of gradient transport models in random walks and in turbulence. *Advances in Geophysics*, 18:25–60.
- Csanady, G. T. (1963). Turbulent diffusion of heavy particles in the atmosphere. *Journal of the Atmospheric Sciences*, 20(3):201–208.
- Cuxart, J., Holtslag, A., Beare, R., Bazile, E., Beljaars, A., Cheng, A., Conangla, L., Ek, M., Freedman, F., Hamdi, R., Kerstein, A., Kitagawa, H., Lenderink, G., Lewellen, D., Mailhot, J., Mauritzen, T., Perov, V., Schayes, G., Steeneveld, G.-J., Svensson, G., Taylor, P., Weng, W., Wunsch, S., and Xu, K.-M. (2006). Single-column model intercomparison for a stably stratified atmospheric boundary layer. *Boundary-Layer Meteorology*, 118(2):273–303.
- Damköhler, G. (1940). Der einfluss der turbulenz auf die flammengeschwindigkeit in gasgemischen. *Zeitschrift für Elektrochemie und angewandte physikalische Chemie*, 46(11):601–626.

- de Arellano, J. V.-G., Duynkerke, P. G., Jonker, P. J., and Builtjes, P. J. (1993). An observational study on the effects of time and space averaging in photochemical models. *Atmospheric Environment. Part A. General Topics*, 27(3):353–362.
- De Ridder, K. (2010). Bulk transfer relations for the roughness sublayer. *Boundary-Layer Meteorology*, 134(2):257–267.
- Deardorff, J. W. (1966). The counter-gradient heat flux in the lower atmosphere and in the laboratory. *Journal of the Atmospheric Sciences*, 23(5):503–506.
- Deardorff, J. W. (1970). A numerical study of three-dimensional turbulent channel flow at large reynolds numbers. *Journal of Fluid Mechanics*, 41:453–480.
- Deardorff, J. W. (1978). Closure of second- and third- moment rate equations for diffusion in homogeneous turbulence. *Physics of Fluids*, 21(4):525–530.
- Dupont, S. and Patton, E. G. (2012). Influence of stability and seasonal canopy changes on micrometeorology within and above an orchard canopy: The CHATS experiment. *Agricultural and Forest Meteorology*, 157(0):11–29.
- Dwyer, M. J., Patton, E. G., and Shaw, R. H. (1997). Turbulent kinetic energy budgets from a large-eddy simulation of airflow above and within a forest canopy. *Boundary-Layer Meteorology*, 84(1):23–43.
- Echekki, T., Kerstein, A. R., Dreeben, T. D., and Chen, J.-Y. (2001). One-dimensional turbulence simulation of turbulent jet diffusion flames: model formulation and illustrative applications. *Combustion and Flame*, 125(3):1083–1105.
- Fan, S.-M., Wofsy, S. C., Bakwin, P. S., Jacob, D. J., and Fitzjarrald, D. R. (1990). Atmosphere-biosphere exchange of CO₂ and O₃ in the central amazon forest. *Journal of Geophysical Research: Atmospheres*, 95(D10):16851–16864.
- Ferziger, J. H. and Perić, M. (2002). *Computational Methods for Fluid Dynamics*. Springer Berlin Heidelberg.
- Finnigan, J. (2000). Turbulence in plant canopies. *Annual Review of Fluid Mechanics*, 32(1):519–571.
- Finnigan, J., Harman, I., Ross, A., and Belcher, S. (2015). First-order turbulence closure for modelling complex canopy flows. *Quarterly Journal of the Royal Meteorological Society*, 141(692):2907–2916.
- Fitzjarrald, D. R., Moore, K. E., Cabral, O. M. R., Scolar, J., Manzi, A. O., and de Abreu Sá, L. D. (1990). Daytime turbulent exchange between the amazon forest and the atmosphere. *Journal of Geophysical Research: Atmospheres*, 95(D10):16825–16838.

- Flack, K. A., Schultz, M. P., and Connelly, J. S. (2007). Examination of a critical roughness height for outer layer similarity. *Physics of Fluids*, 19(9):n/a–n/a.
- Flesch, T. K. and Wilson, J. D. (1992). A two-dimensional trajectory-simulation model for non-gaussian, inhomogeneous turbulence within plant canopies. *Boundary-Layer Meteorology*, 61(4):349–374.
- Florens, E., Eiff, O., and Moulin, F. (2013). Defining the roughness sublayer and its turbulence statistics. *Experiments in Fluids*, 54(4):1500.
- Freire, L. S., Chamecki, M., and Gillies, J. A. (2016). Flux-profile relationship for dust concentration in the stratified atmospheric surface layer. *Boundary-Layer Meteorology*, 160(2):249–267.
- Fuentes, J. D., Chamecki, M., dos Santos, R. M. N., Randow, C. V., Stoy, P. C., Katul, G., Fitzjarrald, D., Manzi, A., Gerken, T., Trowbridge, A., Freire, L. S., Ruiz-Plancarte, J., Maia, J. M. F., Tóta, J., Dias, N., Fisch, G., Schumacher, C., Acevedo, O., and Mercer, J. R. (2016). Linking meteorology, turbulence, and air chemistry in the amazon rainforest. *Bulletin of the American Meteorological Society*, 97(12):2329–2342.
- Gaskell, P. H. and Lau, A. K. C. (1988). Curvature-compensated convective transport: Smart, a new boundedness- preserving transport algorithm. *International Journal for Numerical Methods in Fluids*, 8(6):617–641.
- Gerken, T., Wei, D., Chase, R. J., Fuentes, J. D., Schumacher, C., Machado, L. A., Andreoli, R. V., Chamecki, M., de Souza, R. A. F., Freire, L. S., Jardine, A. B., Manzi, A. O., dos Santos, R. M. N., von Randow, C., dos Santos Costa, P., Stoy, P. C., Tóta, J., and Trowbridge, A. M. (2016). Downward transport of ozone rich air and implications for atmospheric chemistry in the amazon rainforest. *Atmospheric Environment*, 124, Part A:64 – 76.
- Germano, M., Piomelli, U., Moin, P., and Cabot, W. H. (1991). A dynamic subgrid-scale eddy viscosity model. *Physics of Fluids A*, 3(7):1760–1765.
- Gillies, J. and Berkofsky, L. (2004). Eolian suspension above the saltation layer, the concentration profile. *Journal of Sedimentary Research*, 74(2):176–183.
- Ginoux, P., Chin, M., Tegen, I., Prospero, J. M., Holben, B., Dubovik, O., and Lin, S.-J. (2001). Sources and distributions of dust aerosols simulated with the GOCART model. *Journal of Geophysical Research: Atmospheres*, 106(D17):20255–20273.
- Gleicher, S. C., Chamecki, M., Isard, S. A., Pan, Y., and Katul, G. G. (2014). Interpreting three-dimensional spore concentration measurements and escape

- fraction in a crop canopy using a coupled eulerian-lagrangian stochastic model. *Agricultural and Forest Meteorology*, 194:118–131.
- Gong, S. L., Barrie, L. A., Blanchet, J.-P., von Salzen, K., Lohmann, U., Lesins, G., Spacek, L., Zhang, L. M., Girard, E., Lin, H., Leaitch, R., Leighton, H., Chylek, P., and Huang, P. (2003). Canadian aerosol module: A size-segregated simulation of atmospheric aerosol processes for climate and air quality models 1. module development. *Journal of Geophysical Research: Atmospheres*, 108(D1):AAC3–1–AAC3–16.
- Gregory, G. L., Browell, E. V., and Warren, L. S. (1988). Boundary layer ozone: An airborne survey above the amazon basin. *Journal of Geophysical Research: Atmospheres*, 93(D2):1452–1468.
- Grooms, I. and Majda, A. J. (2013). Efficient stochastic superparameterization for geophysical turbulence. *Proceedings of the National Academy of Sciences*, 110(12):4464–4469.
- Gu, L., Shugart, H. H., Fuentes, J. D., Black, T., and Shewchuk, S. R. (1999). Micrometeorology, biophysical exchanges and NEE decomposition in a two-story boreal forest – development and test of an integrated model. *Agricultural and Forest Meteorology*, 94(2):123 – 148.
- Hamba, F. (1993). A modified k model for chemically reactive species in the planetary boundary layer. *Journal of Geophysical Research: Atmospheres*, 98(D3):5173–5182.
- Hanna, S. R. (1981). Lagrangian and eulerian time-scale relations in the daytime boundary layer. *Journal of Applied Meteorology*, 20(3):242–249.
- Harman, I. N. and Finnigan, J. J. (2007). A simple unified theory for flow in the canopy and roughness sublayer. *Boundary-Layer Meteorology*, 123(2):339–363.
- Hill, J. C. (1976). Homogeneous turbulent mixing with chemical reaction. *Annual Review of Fluid Mechanics*, 8(1):135–161.
- Holtslag, A. A. M. and Moeng, C.-H. (1991). Eddy diffusivity and countergradient transport in the convective atmospheric boundary layer. *Journal of the Atmospheric Sciences*, 48(14):1690–1698.
- Hoppel, W. A., Frick, G. M., and Fitzgerald, J. W. (2002). Surface source function for sea-salt aerosol and aerosol dry deposition to the ocean surface. *Journal of Geophysical Research: Atmospheres*, 107(D19):AAC7–1–AAC7–17. 4382.

- Horst, T. W., Kleissl, J., Lenschow, D. H., Meneveau, C., Moeng, C.-H., Parlange, M. B., Sullivan, P. P., and Weil, J. C. (2004). Hats: Field observations to obtain spatially filtered turbulence fields from crosswind arrays of sonic anemometers in the atmospheric surface layer. *Journal of the Atmospheric Sciences*, 61(13):1566–1581.
- Huang, J., Katul, G., and Albertson, J. (2013). The role of coherent turbulent structures in explaining scalar dissimilarity within the canopy sublayer. *Environmental Fluid Mechanics*, 13(6):571–599.
- Jackson, P. S. (1981). On the displacement height in the logarithmic velocity profile. *Journal of Fluid Mechanics*, 111:15–25.
- Jacob, D. J. and Wofsy, S. C. (1990). Budgets of reactive nitrogen, hydrocarbons, and ozone over the amazon forest during the wet season. *Journal of Geophysical Research: Atmospheres*, 95(D10):16737–16754.
- Jardine, A. B., Jardine, K. J., Fuentes, J. D., Martin, S. T., Martins, G., Durgante, F., Carneiro, V., Higuchi, N., Manzi, A. O., and Chambers, J. Q. (2015). Highly reactive light-dependent monoterpenes in the amazon. *Geophysical Research Letters*, 42(5):1576–1583. 2014GL062573.
- Jardine, K., Yañez Serrano, A., Arneth, A., Abrell, L., Jardine, A., van Haren, J., Artaxo, P., Rizzo, L. V., Ishida, F. Y., Karl, T., Kesselmeier, J., Saleska, S., and Huxman, T. (2011). Within-canopy sesquiterpene ozonolysis in amazonia. *Journal of Geophysical Research: Atmospheres*, 116(D19):n/a–n/a. D19301.
- Jiménez, P. A., Dudhia, J., González-Rouco, J. F., Navarro, J., Montávez, J. P., and García-Bustamante, E. (2012). A revised scheme for the wrf surface layer formulation. *Monthly Weather Review*, 140(3):898–918.
- Jones, H. G. (1998). Stomatal control of photosynthesis and transpiration. *Journal of Experimental Botany*, 49(Special Issue):387–398.
- Juang, J.-Y., Katul, G. G., Siqueira, M. B., Stoy, P. C., and McCarthy, H. R. (2008). Investigating a hierarchy of eulerian closure models for scalar transfer inside forested canopies. *Boundary-Layer Meteorology*, 128(1):1–32.
- Kaimal, J. C. and Finnigan, J. J. (1994). *Atmospheric boundary layer flows: their structure and measurement*. Oxford University Press.
- Kanda, M., Inagaki, A., Letzel, M. O., Raasch, S., and Watanabe, T. (2004). LES study of the energy imbalance problem with eddy covariance fluxes. *Boundary-Layer Meteorology*, 110(3):381–404.

- Kaser, L., Karl, T., Yuan, B., Mauldin, R., Cantrell, C., Guenther, A., Patton, E., Weinheimer, A., Knote, C., Orlando, J., et al. (2015). Chemistry-turbulence interactions and mesoscale variability influence the cleansing efficiency of the atmosphere. *Geophysical Research Letters*, 42(24).
- Katul, G. and Albertson, J. (1998). An investigation of higher-order closure models for a forested canopy. *Boundary-Layer Meteorology*, 89(1):47–74.
- Katul, G., Grönholm, T., Launiainen, S., and Vesala, T. (2011). The effects of the canopy medium on dry deposition velocities of aerosol particles in the canopy sub-layer above forested ecosystems. *Atmospheric Environment*, 45(5):1203–1212.
- Kerstein, A., Ashurst, W. T., Wunsch, S., and Nilsen, V. (2001). One-dimensional turbulence: vector formulation and application to free shear flows. *Journal of Fluid Mechanics*, 447:85–109.
- Kerstein, A. R. (1999). One-dimensional turbulence: model formulation and application to homogeneous turbulence, shear flows, and buoyant stratified flows. *Journal of Fluid Mechanics*, 392:277–334.
- Kerstein, A. R. and Wunsch, S. (2006). Simulation of a stably stratified atmospheric boundary layer using one-dimensional turbulence. *Boundary-Layer Meteorology*, 118(2):325–356.
- Kesselmeier, J., Kuhn, U., Wolf, A., Andreae, M., Ciccioli, P., Brancaleoni, E., Frattoni, M., Guenther, A., Greenberg, J., Vasconcellos, P. D. C., de Oliva, T., Tavares, T., and Artaxo, P. (2000). Atmospheric volatile organic compounds (voc) at a remote tropical forest site in central amazonia. *Atmospheric Environment*, 34(24):4063 – 4072.
- Khairoutdinov, M., Randall, D., and DeMott, C. (2005). Simulations of the atmospheric general circulation using a cloud-resolving model as a superparameterization of physical processes. *Journal of the Atmospheric Sciences*, 62(7):2136–2154.
- Kind, R. (1992). One-dimensional aeolian suspension above beds of loose particles: A new concentration-profile equation. *Atmospheric Environment. Part A. General Topics*, 26(5):927–931.
- Kirchhoff, V. W. J. H. (1988). Surface ozone measurements in amazonia. *Journal of Geophysical Research: Atmospheres*, 93(D2):1469–1476.
- Kleissl, J., Kumar, V., Meneveau, C., and Parlange, M. B. (2006). Numerical study of dynamic smagorinsky models in large-eddy simulation of the atmospheric boundary layer: Validation in stable and unstable conditions. *Water Resources Research*, 42(6):W06D09.

- Klose, M. and Shao, Y. (2013). Large-eddy simulation of turbulent dust emission. *Aeolian Research*, 8(0):49–58.
- Koeltzsch, K. (1998). On the relationship between the lagrangian and eulerian time scale. *Atmospheric Environment*, 33(1):117 – 128.
- Kok, J. F., Parteli, E. J. R., Michaels, T. I., and Karam, D. B. (2012). The physics of wind-blown sand and dust. *Reports on Progress in Physics*, 75(10):106901.
- Kruijt, B., Malhi, Y., Lloyd, J. D., Nobre, A., Miranda, A., Pereira, M., Culf, A., and Grace, J. (2000). Turbulence statistics above and within two amazon rain forest canopies. *Boundary-Layer Meteorology*, 94(2):297–331.
- Kumar, V., Kleissl, J., Meneveau, C., and Parlange, M. B. (2006). Large-eddy simulation of a diurnal cycle of the atmospheric boundary layer: Atmospheric stability and scaling issues. *Water Resources Research*, 42(6):n/a–n/a.
- Kundu, P. K., Cohen, I. M., and Dowling, D. R. (2012). *Fluid mechanics*. Academic Press.
- Lamb, R. G. (1973). Note on the application of k-theory to diffusion problems involving nonlinear chemical reactions. *Atmospheric Environment (1967)*, 7(3):257–263.
- Launiainen, S., Katul, G., Gronholm, T., and Vesala, T. (2013). Partitioning ozone fluxes between canopy and forest floor by measurements and a multi-layer model. *Agricultural and Forest Meteorology*, 173:85–99.
- Lebedev, N. N. (1972). *Special functions & their applications*. Dover Publications, New York. 336 pp.
- Lelieveld, J., Butler, T. M., Crowley, J. N., Dillon, T. J., Fischer, H., Ganzeveld, L., Harder, H., Lawrence, M. G., Martinez, M., Taraborrelli, D., and Williams, J. (2008). Atmospheric oxidation capacity sustained by a tropical forest. *Nature*, 452(7188):737–740.
- Lelieveld, J., Gromov, S., Pozzer, A., and Taraborrelli, D. (2016). Global tropospheric hydroxyl distribution, budget and reactivity. *Atmospheric Chemistry and Physics Discussions*, 2016:1–25.
- Lenschow, D. H. and Stankov, B. B. (1986). Length scales in the convective boundary layer. *Journal of the Atmospheric Sciences*, 43(12):1198–1209.
- Lien, R.-C. and D'Asaro, E. A. (2002). The kolmogorov constant for the lagrangian velocity spectrum and structure function. *Physics of Fluids*, 14(12):4456–4459.

- Lilly, D. K. (1967). The representation of small-scale turbulence in numerical simulation experiments. In *Proc. IBM Scientific Computing Symposium on Environmental Sciences*, page 195.
- Lindvall, J., Svensson, G., and Hannay, C. (2013). Evaluation of near-surface parameters in the two versions of the atmospheric model in cesm1 using flux station observations. *Journal of Climate*, 26(1):26–44.
- Liu, C.-M. (2008). Complete solutions to extended stokes' problems. *Mathematical Problems in Engineering*, 2008:18.
- Liu, Y., Brito, J., Dorris, M. R., Rivera-Rios, J. C., Seco, R., Bates, K. H., Artaxo, P., Duvoisin, S., Keutsch, F. a. N., Kim, S., et al. (2016). Isoprene photochemistry over the amazon rainforest. *Proceedings of the National Academy of Sciences*, 113(22):6125–6130.
- Majda, A. J. (2007). Multiscale models with moisture and systematic strategies for superparameterization. *Journal of the Atmospheric Sciences*, 64(7):2726–2734.
- Majda, A. J. and Grote, M. J. (2009). Mathematical test models for superparametrization in anisotropic turbulence. *Proceedings of the National Academy of Sciences*, 106(14):5470–5474.
- Marques Filho, A. d. O., Dallarosa, R. G., and Pachêco, V. B. (2005). Solar radiation and vertical leaf area distribution in forest-reserva biológica do cueiras ZF02, manaus. *Acta Amazonica*, 35:427 – 436.
- Martens, C. S., Shay, T. J., Mendlovitz, H. P., Matross, D. M., Saleska, S. R., Wofsy, S. C., Stephen Woodward, W., Menton, M. C., De Moura, J. M. S., Crill, P. M., De Moraes, O. L. L., and Lima, R. L. (2004). Radon fluxes in tropical forest ecosystems of brazilian amazonia: night-time co₂ net ecosystem exchange derived from radon and eddy covariance methods. *Global Change Biology*, 10(5):618–629.
- Martin, S. T., Artaxo, P., Machado, L. A. T., Manzi, A. O., Souza, R. A. F., Schumacher, C., Wang, J., Andreae, M. O., Barbosa, H. M. J., Fan, J., Fisch, G., Goldstein, A. H., Guenther, A., Jimenez, J. L., Pöschl, U., Silva Dias, M. A., Smith, J. N., and Wendisch, M. (2016). Introduction: Observations and modeling of the green ocean amazon (goamazon2014/5). *Atmospheric Chemistry and Physics*, 16(8):4785–4797.
- Mason, P. J. and Thomson, D. J. (1992). Stochastic backscatter in large-eddy simulations of boundary layers. *Journal of Fluid Mechanics*, 242:51–78.
- Massman, W. and Weil, J. (1999). An analytical one-dimensional second-order closure model of turbulence statistics and the lagrangian time scale within

- and above plant canopies of arbitrary structure. *Boundary-Layer Meteorology*, 91(1):81–107.
- Maurer, K. D., Bohrer, G., Kenny, W. T., and Ivanov, V. Y. (2015). Large-eddy simulations of surface roughness parameter sensitivity to canopy-structure characteristics. *Biogeosciences*, 12(8):2533–2548.
- McRae, G. J., Goodin, W. R., and Seinfeld, J. H. (1982). Mathematical modeling of photochemical air pollution. environmental quality laboratory report. Technical report, California Institute of Technology.
- McWilliam, A.-L. C., Roberts, J. M., Cabral, O. M. R., Leitao, M. V. B. R., de Costa, A. C. L., Maitelli, G. T., and Zamparoni, C. A. G. P. (1993). Leaf area index and above-ground biomass of terra firme rain forest and adjacent clearings in amazonia. *Functional Ecology*, 7(3):310–317.
- Moeng, C.-H. (1984). A large-eddy-simulation model for the study of planetary boundary-layer turbulence. *Journal of the Atmospheric Sciences*, 41(13):2052–2062.
- Moeng, C.-H. and Wyngaard, J. C. (1989). Evaluation of turbulent transport and dissipation closures in second-order modeling. *Journal of the Atmospheric Sciences*, 46(14):2311–2330.
- Molod, A., Takacs, L., Suarez, M., and Bacmeister, J. (2015). Development of the GEOS-5 atmospheric general circulation model: evolution from MERRA to MERRA2. *Geoscientific Model Development*, 8(5):1339–1356.
- Monin, A. and Obukhov, A. (1954). Basic laws of turbulent mixing in the surface layer of the atmosphere. *Trudy Geofizicheskogo Instituta, Akademiya Nauk SSSR*, 151:163–187.
- Monin, A. and Yaglom, A. (2013). *Statistical Fluid Mechanics, Volume II: Mechanics of Turbulence*. Dover Books on Physics. Dover Publications.
- Monin, A. S. (1970). The atmospheric boundary layer. *Annual Review of Fluid Mechanics*, 2(1):225–250.
- Moser, R. D., Kim, J., and Mansour, N. N. (1999). Direct numerical simulation of turbulent channel flow up to $\text{Re}_\tau = 590$. *Physics of Fluids*, 11(4):943–945.
- Nho-Kim, E.-Y., Michou, M., and Peuch, V.-H. (2004). Parameterization of size-dependent particle dry deposition velocities for global modeling. *Atmospheric Environment*, 38(13):1933–1942.

- O'Connell, L. M., Mosseler, A., and Rajora, O. P. (2007). Extensive long-distance pollen dispersal in a fragmented landscape maintains genetic diversity in white spruce. *Journal of Heredity*, 98(7):640–645.
- Ouellette, N. T., Xu, H., Bourgoin, M., and Bodenschatz, E. (2006). Small-scale anisotropy in lagrangian turbulence. *New Journal of Physics*, 8(6):102.
- Ouwersloot, H., Vilà-Guerau de Arellano, J., van Heerwaarden, C., Ganzeveld, L., Krol, M., and Lelieveld, J. (2010). The significance of species segregation for amazionic chemistry. In *19th Symposium on Boundary Layers and Turbulence/29th Conference on Agricultural and Forest Meteorology, AMS, extended abstract*.
- Pan, Y., Chamecki, M., and Isard, S. A. (2013). Dispersion of heavy particles emitted from area sources in the unstable atmospheric boundary layer. *Boundary-Layer Meteorology*, 146(2):235–256.
- Pan, Y., Chamecki, M., and Isard, S. A. (2014). Large-eddy simulation of turbulence and particle dispersion inside the canopy roughness sublayer. *Journal of Fluid Mechanics*, 753:499–534.
- Patton, E., Davis, K., Barth, M., and Sullivan, P. (2001). Decaying scalars emitted by a forest canopy: A numerical study. *Boundary-Layer Meteorology*, 100(1):91–129.
- Patton, E. G., Horst, T. W., Sullivan, P. P., Lenschow, D. H., Oncley, S. P., Brown, W. O. J., Burns, S. P., Guenther, A. B., Held, A., Karl, T., Mayor, S. D., Rizzo, L. V., Spuler, S. M., Sun, J., Turnipseed, A. A., Allwine, E. J., Edburg, S. L., Lamb, B. K., Avissar, R., Calhoun, R. J., Kleissl, J., Massman, W. J., Paw U, K. T., and Weil, J. C. (2010). The canopy horizontal array turbulence study. *Bulletin of the American Meteorological Society*, 92(5):593–611.
- Patton, E. G., Sullivan, P. P., Shaw, R. H., Finnigan, J. J., and Weil, J. C. (2016). Atmospheric stability influences on coupled boundary layer and canopy turbulence. *Journal of the Atmospheric Sciences*, 73(4):1621–1647.
- Paulson, S. E. and Orlando, J. J. (1996). The reactions of ozone with alkenes: An important source of hox in the boundary layer. *Geophysical Research Letters*, 23(25):3727–3730.
- Piomelli, U. and Balaras, E. (2002). Wall-layer models for large-eddy simulations. *Annual Review of Fluid Mechanics*, 34(1):349–374.
- Piomelli, U., Ferziger, J., Moin, P., and Kim, J. (1989). New approximate boundary conditions for large eddy simulations of wall-bounded flows. *Physics of Fluids A*, 1(6):1061–1068.

- Pleijel, H. (2008). Concentration gradients of ozone and other trace gases in and above cereal canopies. *Meteorologische Zeitschrift*, 17(2):187–192.
- Poggi, D., Katul, G., and Albertson, J. (2006). Scalar dispersion within a model canopy: Measurements and three-dimensional lagrangian models. *Advances in Water Resources*, 29(2):326–335. Experimental Hydrology: A Bright Future.
- Poggi, D. and Katul, G. G. (2006). Two-dimensional scalar spectra in the deeper layers of a dense and uniform model canopy. *Boundary-Layer Meteorology*, 121(2):267–281.
- Poggi, D., Katul, G. G., and Cassiani, M. (2008). On the anomalous behavior of the lagrangian structure function similarity constant inside dense canopies. *Atmospheric Environment*, 42(18):4212 – 4231.
- Pope, S. B. (2000). *Turbulent Flows*. Cambridge University Press.
- Pope, S. B. and Chen, Y. L. (1990). The velocity-dissipation probability density function model for turbulent flows. *Physics of Fluids A*, 2(8):1437–1449.
- Porté-Agel, F., Meneveau, C., and Parlange, M. B. (2000). A scale-dependent dynamic model for large-eddy simulation: application to a neutral atmospheric boundary layer. *Journal of Fluid Mechanics*, 415:261–284.
- Prandtl, L. (1952). *Essentials of fluid dynamics*. Blackie and Son, London.
- Rannik, Ü., Zhou, L., Zhou, P., Gierens, R., Mammarella, I., Sogachev, A., and Boy, M. (2016). Aerosol dynamics within and above forest in relation to turbulent transport and dry deposition. *Atmospheric Chemistry & Physics*, 16:3145–3160.
- Raupach, M. (1989a). Applying lagrangian fluid mechanics to infer scalar source distributions from concentration profiles in plant canopies. *Agricultural and Forest Meteorology*, 47(2):85 – 108.
- Raupach, M. (1989b). A practical lagrangian method for relating scalar concentrations to source distributions in vegetation canopies. *Quarterly Journal of the Royal Meteorological Society*, 115(487):609–632.
- Raupach, M., Coppin, P., and Legg, B. (1986). Experiments on scalar dispersion within a model plant canopy part i: The turbulence structure. *Boundary-Layer Meteorology*, 35(1-2):21–52.
- Raupach, M. R. (1994). Simplified expressions for vegetation roughness length and zero-plane displacement as functions of canopy height and area index. *Boundary-Layer Meteorology*, 71(1):211–216.

- Reynolds, A. M. (1998). On the formulation of lagrangian stochastic models of scalar dispersion within plant canopies. *Boundary-Layer Meteorology*, 86(2):333–344.
- Reynolds, A. M. (2012). Incorporating sweeps and ejections into lagrangian stochastic models of spore trajectories within plant canopy turbulence: Modeled contact distributions are heavy-tailed. *Phytopathology*, 102(11):1026–1033.
- Rodean, H. C. (1995). Turbulent diffusion as a stochastic lagrangian process. *Environmetrics*, 6(6):659–663.
- Rummel, U., Ammann, C., Kirkman, G. A., Moura, M. A. L., Foken, T., Andreae, M. O., and Meixner, F. X. (2007). Seasonal variation of ozone deposition to a tropical rain forest in southwest amazonia. *Atmospheric Chemistry and Physics*, 7(20):5415–5435.
- Santos, D. M., Acevedo, O. C., Chamecki, M., Fuentes, J. D., Gerken, T., and Stoy, P. C. (2016). Temporal scales of the nocturnal flow within and above a forest canopy in amazonia. *Boundary-Layer Meteorology*, 161(1):73–98.
- Schmidt, J. R., Wendt, J. O., and Kerstein, A. R. (2009). Non-equilibrium wall deposition of inertial particles in turbulent flow. *Journal of Statistical Physics*, 137(2):233–257.
- Schmidt, R. C., Kerstein, A. R., Wunsch, S., and Nilsen, V. (2003). Near-wall LES closure based on one-dimensional turbulence modeling. *Journal of Computational Physics*, 186(1):317–355.
- Schultz, M. P. and Flack, K. A. (2013). Reynolds-number scaling of turbulent channel flow. *Physics of Fluids*, 25(2):n/a–n/a.
- Schumann, U. (1975). Subgrid scale model for finite difference simulations of turbulent flows in plane channels and annuli. *Journal of Computational Physics*, 18(4):376 – 404.
- Schumann, U. (1989). Large-eddy simulation of turbulent diffusion with chemical reactions in the convective boundary layer. *Atmospheric Environment (1967)*, 23(8):1713–1727.
- Shao, Y. (2000). *Physics and Modelling of Wind Erosion*. Kluwer Academic Publishers.
- Shaw, R. H. and Schumann, U. (1992). Large-eddy simulation of turbulent flow above and within a forest. *Boundary-Layer Meteorology*, 61(1):47–64.

- Shu, Y. and Atkinson, R. (1994). Rate constants for the gas-phase reactions of O₃ with a series of terpenes and OH radical formation from the O₃ reactions with sesquiterpenes at 296 ± 2 K. *International Journal of Chemical Kinetics*, 26(12):1193–1205.
- Sigler, J. M., Fuentes, J. D., Heitz, R. C., Garstang, M., and Fisch, G. (2002). Ozone dynamics and deposition processes at a deforested site in the amazon basin. *AMBIO: A Journal of the Human Environment*, 31(1):21–27.
- Simon, E., Lehmann, B., Ammann, C., Ganzeveld, L., Rummel, U., Meixner, F., Nobre, A., Araújo, A., and Kesselmeier, J. (2005). Lagrangian dispersion of 222rn, H₂O and CO₂ within amazonian rain forest. *Agricultural and Forest Meteorology*, 132(3):286–304.
- Siqueira, M., Lai, C.-T., and Katul, G. (2000). Estimating scalar sources, sinks, and fluxes in a forest canopy using lagrangian, eulerian, and hybrid inverse models. *Journal of Geophysical Research: Atmospheres*, 105(D24):29475–29488.
- Smagorinsky, J. (1963). General circulation experiments with the primitive equations i. the basic experiment. *Monthly Weather Review*, 91(3):99–164.
- Sorbjan, Z. (1991). Evaluation of local similarity functions in the convective boundary layer. *Journal of Applied Meteorology*, 30(12):1565–1583.
- Sreenivasan, K. R. (1995). On the universality of the kolmogorov constant. *Physics of Fluids*, 7(11):2778–2784.
- Sreenivasan, K. R., Chambers, A. J., and Antonia, R. A. (1978). Accuracy of moments of velocity and scalar fluctuations in the atmospheric surface layer. *Boundary-Layer Meteorology*, 14(3):341–359.
- Stockwell, W. R. (1995). Effects of turbulence on gas-phase atmospheric chemistry: Calculation of the relationship between time scales for diffusion and chemical reaction. *Meteorology and Atmospheric Physics*, 57(1):159–171.
- Stroud, C., Makar, P., Karl, T., Guenther, A., Geron, C., Turnipseed, A., Nemitz, E., Baker, B., Potosnak, M., and Fuentes, J. D. (2005). Role of canopy-scale photochemistry in modifying biogenic-atmosphere exchange of reactive terpene species: Results from the celtic field study. *Journal of Geophysical Research: Atmospheres*, 110(D17):n/a–n/a.
- Su, H.-B., Shaw, R., Paw, K., Moeng, C.-H., and Sullivan, P. (1998). Turbulent statistics of neutrally stratified flow within and above a sparse forest from large-eddy simulation and field observations. *Boundary-Layer Meteorology*, 88(3):363–397.

- Sun, G., Lignell, D. O., Hewson, J. C., and Gin, C. R. (2014). Particle dispersion in homogeneous turbulence using the one-dimensional turbulence model. *Physics of Fluids*, 26(10):n/a–n/a.
- Swap, R., Garstang, M., Greco, S., Talbot, R., and Kallberg, P. (1992). Saharan dust in the amazon basin. *Tellus B*, 44(2):133–149.
- Taylor, G. I. (1922). Diffusion by continuous movements. *Proceedings of the London Mathematical Society*, s2-20(1):196–212.
- Thomas, C. K., Martin, J. G., Law, B. E., and Davis, K. (2013). Toward biologically meaningful net carbon exchange estimates for tall, dense canopies: Multi-level eddy covariance observations and canopy coupling regimes in a mature Douglas-fir forest in Oregon. *Agricultural and Forest Meteorology*, 173:14–27.
- Thomson, D. J. (1987). Criteria for the selection of stochastic models of particle trajectories in turbulent flows. *Journal of Fluid Mechanics*, 180:529–556.
- Tóta, J., Roy Fitzjarrald, D., and da Silva Dias, M. A. (2012). Amazon rainforest exchange of carbon and subcanopy air flow: Manaus LBA site – a complex terrain condition. *The Scientific World Journal*, 2012:1–19.
- Trumbore, S. E., Keller, M., Wofsy, S. C., and da Costa, J. M. (1990). Measurements of soil and canopy exchange rates in the amazon rain forest using ^{222}Rn . *Journal of Geophysical Research: Atmospheres*, 95(D10):16865–16873.
- Tsoar, H. and Pye, K. (1987). Dust transport and the question of desert loess formation. *Sedimentology*, 34(1):139–153.
- Verseghy, D. L. (1991). Class - a canadian land surface scheme for gcms. i. soil model. *International Journal of Climatology*, 11(2):111–133.
- Wilson, J. D. (1988). A second-order closure model for flow through vegetation. *Boundary-Layer Meteorology*, 42(4):371–392.
- Wilson, J. D. and Sawford, B. L. (1996). Review of lagrangian stochastic models for trajectories in the turbulent atmosphere. *Boundary-Layer Meteorology*, 78(1):191–210.
- Wilson, J. D., Ward, D. P., Thurtell, G. W., and Kidd, G. E. (1982). Statistics of atmospheric turbulence within and above a corn canopy. *Boundary-Layer Meteorology*, 24(4):495–519.
- Wilson, N. R. and Shaw, R. H. (1977). A higher order closure model for canopy flow. *Journal of Applied Meteorology*, 16(11):1197–1205.

- Wouters, H., De Ridder, K., and van Lipzig, N. P. M. (2012). Comprehensive parametrization of surface-layer transfer coefficients for use in atmospheric numerical models. *Boundary-Layer Meteorology*, 145(3):539–550.
- Xiao, J. and Taylor, P. A. (2002). On equilibrium profiles of suspended particles. *Boundary-Layer Meteorology*, 105(3):471–482.
- Xing, Y., Majda, A. J., and Grabowski, W. W. (2009). New efficient sparse space-time algorithms for superparameterization on mesoscales. *Monthly Weather Review*, 137(12):4307–4324.
- Xu, L., Pyles, R. D., U, K. T. P., Snyder, R., Monier, E., Falk, M., and Chen, S.-H. (2015). Impact of canopy representations on regional modeling of evapotranspiration using the WRF–ACASA coupled model. Technical report, MIT Joint Program on the Science and Policy of Global Change.
- Xue, M., Droege, K. K., Wong, V., Shapiro, A., Brewster, K., Carr, F., Weber, D., Liu, Y., and Wang, D. (2001). The advanced regional prediction system (ARPS) – a multi-scale nonhydrostatic atmospheric simulation and prediction tool. part ii: Model physics and applications. *Meteorology and Atmospheric Physics*, 76(3):143–165.
- Yamazaki, T., Kondo, J., Watanabe, T., and Sato, T. (1992). A heat-balance model with a canopy of one or two layers and its application to field experiments. *Journal of Applied Meteorology*, 31(1):86–103.
- Zender, C. S., Bian, H., and Newman, D. (2003). Mineral dust entrainment and deposition (DEAD) model: Description and 1990s dust climatology. *Journal of Geophysical Research: Atmospheres*, 108(D14):4416.
- Zhao, T. L., Gong, S. L., Zhang, X. Y., and McKendry, I. G. (2003). Modeled size-segregated wet and dry deposition budgets of soil dust aerosol during ACE-Asia 2001: Implications for trans-pacific transport. *Journal of Geophysical Research: Atmospheres*, 108(D23):8665.

Vita

Livia Souza Freire Grion

Livia Souza Freire Grion was born on December 8, 1987 in Vitória da Conquista, Bahia, Brazil, the daughter of Maria Dolores Souza Freire and Edson Freire de Oliveira. After finishing high-school in 2005, she entered the Federal University of Paraná in Curitiba, Paraná, Brazil, where she received a Bachelor of Science degree in Environmental Engineering in 2009 and a Master of Science degree in Numerical Methods in Engineering in 2012. She moved to USA in 2012 to join the graduate program in Meteorology and Atmospheric Science of Pennsylvania State University, where she has been working on atmospheric boundary-layer turbulence in the research group of Professor Marcelo Chamecki. During this time, she participated in two field experiment projects (“Bridging Land-surface Fluxes and Aerosol Concentrations to Triggering Convective Rainfall”, DOE, 2014/2016, and “From Turbulence to Weather and Climate: Unraveling the Multiscale Nature of Dust and Sand Transport in the Atmospheric Boundary Layer”, NSF, 2014/2017). In the Spring of 2014, she worked as Teaching Assistant of the course *Introduction to Programming Techniques for Meteorology*, and in the Spring of 2016 she worked as the instructor of the course *Atmospheric Dispersion*, both courses from the undergraduate program on Meteorology of Pennsylvania State University. She has produced and contributed to the following journal publications:

- 2016 **L. S. Freire**, M. Chamecki, and J. A. Gillies. Flux-profile relationship for dust concentration in the stratified atmospheric surface layer. *Boundary-Layer Meteorology*, 160(2):249–267
- J. D. Fuentes and 18 more authors including **L. S. Freire**. Linking meteorology, turbulence, and air chemistry in the amazon rainforest. *Bulletin of the American Meteorological Society*
- T. Gerken and 17 other authors including **L. S. Freire**. Downward transport of ozone rich air and implications for atmospheric chemistry in the Amazon rainforest. *Atmospheric Environment*, 124(A):64–76
- 2013 **L. S. Freire** and N. L. Dias. Residual layer effects on the modeling of convective boundary layer growth rates with a slab model using FIFE data. *Journal of Geophysical Research: Atmospheres*, 118:1–10
- 2012 N. L. Dias, J. E. Gonçalves, **L. S. Freire**, T. Hasegawa, and A. L. Malheiros. Obtaining potential virtual temperature profiles, entrainment fluxes, and spectra from mini unmanned aerial vehicle data. *Boundary-Layer Meteorology*, 145:93–111